

AD-A088 764

RAYTHEON CO WALTHAM MA RESEARCH DIV

F/G 17/9

PRODUCTION OF LITHIUM FERRITE ASSEMBLIES FOR PHASED ARRAY RADAR--ETC(U)

JUN 79 J J GREEN, H J VAN HOOK

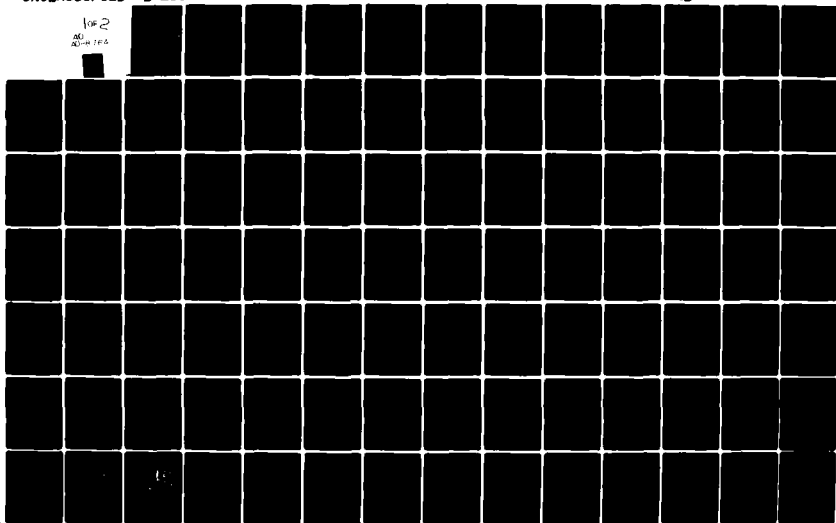
DAAK40-78-C-0082

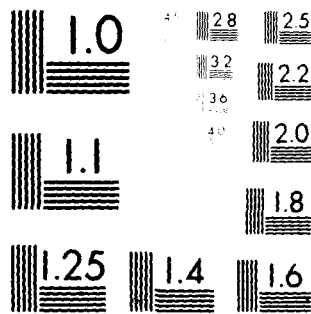
UNCLASSIFIED

S-2554

NL

1 of 2
AD
AD-88 764





MICROCOPY RESOLUTION TEST CHART
NATIONAL BUREAU OF STANDARDS-1963-A

LEVEL

2
P.S.

AD A088764

**PRODUCTION OF LITHIUM FERRITE ASSEMBLIES
FOR PHASED ARRAY RADARS**

*Raytheon Company
Research Division
Waltham, Massachusetts 02154*

DTIC
ELECTE
AUG 27 1980
D
C

June 1979

Final Report for DAAK40-78-C-0082

Prepared for

*Advanced Systems Development and Manufacturing Technology Directorate
Engineering Laboratory
U. S. Army Missile Research and Development Command
Redstone Arsenal, Alabama 35809*

Approved for public release; distribution unlimited.

DDC FILE COPY

~~80 80 8 25 018~~

Unclassified

SECURITY CLASSIFICATION OF THIS PAGE (When Data Entered)

REPORT DOCUMENTATION PAGE		READ INSTRUCTIONS BEFORE COMPLETING FORM
1. REPORT NUMBER	2. GOVT ACCESSION NO.	3. RECIPIENT'S CATALOG NUMBER
	AD-A088	764
4. TITLE (and Subtitle)		5. TYPE OF REPORT & PERIOD COVERED
PRODUCTION OF LITHIUM FERRITE ASSEMBLIES FOR PHASED ARRAY RADARS.		Final Technical Report 3/13/78 - 6/13/79
6. AUTHOR(s)		6. PERFORMING ORG. REPORT NUMBER
J. J. Green H. J. Van Hook		15 S-2554 ✓
7. PERFORMING ORGANIZATION NAME AND ADDRESS		8. CONTRACT OR GRANT NUMBER(s)
Raytheon Research Division 28 Seyon Street Waltham, Massachusetts 02154		15 DAAK 40-78-C-0082
9. CONTROLLING OFFICE NAME AND ADDRESS		10. PROGRAM ELEMENT, PROJECT, TASK AREA & WORK UNIT NUMBERS
U.S. Army Missile Research & Dev. Command Redstone Arsenal, Alabama 35809		11 Jun 77
11. MONITORING AGENCY NAME & ADDRESS (if different from Controlling Office)		12. REPORT DATE
9 Final R. Y. 13 Mar 78-13 Jun 79		June 1979
		13. NUMBER OF PAGES
		118
		15. SECURITY CLASS. (of this report)
		Unclassified
		15a. DECLASSIFICATION/DOWNGRADING SCHEDULE
16. DISTRIBUTION STATEMENT (of this Report)		
Approved for public release; distribution unlimited.		
17. DISTRIBUTION STATEMENT (of the abstract entered in Block 20, if different from Report)		
18. SUPPLEMENTARY NOTES		
19. KEY WORDS (Continue on reverse side if necessary and identify by block number)		
lithium titanium ferrite waveguide toroid insertion phase dielectric materials saturation magnetization anisotropy field remanent magnetization phase shifter magnetic moment		
20. ABSTRACT (Continue on reverse side if necessary and identify by block number)		
An investigation was made of substitutions of Al, Cr, Ga, In, Ni, and Zn in the lithium titanium ferrite ($4\pi M_s = 1200$ gauss). A final composition, $\text{Li}_{0.7275}\text{Ti}_{0.61}\text{Zn}_{0.10}\text{Mn}_{0.10}\text{Ni}_{0.05}\text{Co}_{0.005}\text{Fe}_{1.4075}\text{O}_4$ was selected, and gave an acceptable temperature dependence of insertion phase. Using this composition, eight 2 Kg powder batches and two 40 Kg powder batches were made. Toroid forming, firing, and evaluation techniques were developed to produce a high remanent reproducible waveguide toroid. Over two hundred		

DD FORM 1473 1 JAN 73 EDITION OF 1 NOV 65 IS OBSOLETE

Unclassified

SECURITY CLASSIFICATION OF THIS PAGE (When Data Entered)

1130 106

Unclassified

SECURITY CLASSIFICATION OF THIS PAGE(When Data Entered)

Waveguide toroids were formed from these 10 powder batches in a series of firings. Particular attention was paid to the type of firing cycle and kiln location required to produce a straight toroid.

Two techniques, pin drop and ultrasonic measurement, were evolved to determine toroid straightness. The ultrasonic technique shows more promise and was used to monitor the phase shifting wall thickness in a large portion of the waveguide toroids which had been through final machining. Insertion phase temperature measurements on two toroids made from the large powder batches gave results that are competitive with garnet materials.

Unclassified

SECURITY CLASSIFICATION OF THIS PAGE(When Data Entered)

PREFACE

This report covers work performed under MIRADCOM-supported Contract No. DAAK40-78-C-0082 for the Advanced Systems Development and Manufacturing Technology Directorate during the period April 1978 through May 1979. The project engineer for this contract is Mr. Philip Ormsby. The program's principal investigator was Dr. J. J. Green. Dr. H. J. Van Hook was responsible for the ferrite materials development. Mr. R. J. Maher carried out the processing and firing, with the assistance of Mr. M. L. Stallings. Ferrite property measurements were performed by Messrs. J. H. Saunders and G. E. Flynn. X-ray diffraction and fluorescence work was under the direction of Dr. O. J. Guentert, with Messrs. D. W. Howe and W. Y. Tye assisting. This report has been assigned the Raytheon internal number S-2554.

Accession For	
NTIS GRA&I	<input checked="checked" type="checkbox"/>
DDC TAB	<input type="checkbox"/>
Unannounced	<input type="checkbox"/>
Justification	
By _____	
Distribution/	
Availability Codes	
Dist	Avail and/or special
A	

TABLE OF CONTENTS

	<u>Page</u>
PREFACE	iii
TABLE OF CONTENTS	iv
LIST OF ILLUSTRATIONS	vi
LIST OF TABLES	ix
1.0 INTRODUCTION	1
2.0 RESULTS	10
2.1 Lithium Ferrite Formulation	10
2.1.1 General considerations on cation substitutions	10
2.1.2 Magnetization	11
2.1.3 Anisotropy evaluation	12
2.2 Toroid Processing and Raw Materials Quality Control	46
2.2.1 Raw materials	46
2.2.2 Powder processing	62
2.2.3 Toroid forming	64
2.3 Toroid Property Verification	68
2.3.1 Methods of record keeping for toroids	68
2.3.2 Toroid straightness evaluation	69
2.3.3 Bulk property measurements	70
2.3.3.1 Experimental procedures	70
2.3.3.2 Experimental results	71
2.4 Development of Dielectric Material	88
2.5 Verification of the Dielectric	92
2.6 Co-Manufacturing	94
2.7 Evaluation of Li-Ti-Zn-Ferrite Toroids	94
2.7.1 Introduction	94
2.7.2 Discussion of tabulated results	96
2.7.2.1 Furnace conditions	96
2.7.2.2 Pin clearance and ultrasonic data	96

TABLE OF CONTENTS (Continued)

	<u>Page</u>
2.7.2.3 Summary of toroid firings	97
2.7.3 Future work	98
2.8 Phase Shifter Evaluation	99
2.9 Economic Forecast: Relative Cost of Toroids Made From Lithium Ferrite and Garnet	99
3.0 SUMMARY AND CONCLUSIONS	107

LIST OF ILLUSTRATIONS

<u>Fig. No.</u>		<u>Page No.</u>
1	Early Non-Reciprocal Phase Shifters (External H)	2
2	First Type of Non-Reciprocal Latching Phase Shifter	3
3	Non-Reciprocal Latching Phase Shifter with Dielectric Loading	4
4	Non-Reciprocal Latching Phase Shifter - Side Loaded Geometry	5
5	Saturated Insertion Phase as a Function of Temperature	7
6	Saturated Insertion Phase as a Function of Temperature	8
7	n_B vs. T for $z = 0$, from Dionne (1974)	13
8	n_B vs. T for $z = 0.05$, from Dionne (1974)	14
9	n_B vs. T for $z = 0.10$, from Dionne (1974)	15
10	Magnetization vs. Ti(x) Content in $\text{Li}_{\frac{1+x-v-z}{2}} \text{Mn}_y \text{Co}_v \text{Ti}_x \text{Zn}_z \text{Fe}_{\frac{5-3x-v-z}{2}} \text{O}_4$	16
11	Anisotropy Field Determination from Magnetization Plot	18
12	Anisotropy Field Determination from Magnetization Plot	19
13	Anisotropy Field Determination from Magnetization Plot	20
14	Anisotropy Field Determination from Magnetization Plot	21
15	Anisotropy Field Determination from Magnetization Plot	22
16	Anisotropy Field Determination from Magnetization Plot	23
17	Saturation Magnetization as a Function of Temperature	28
18	Saturation Magnetization as a Function of Temperature	29
19	Saturation Magnetization as a Function of Temperature	30
20	Saturation Magnetization as a Function of Temperature	31
21	Saturation Magnetization as a Function of Temperature	32
22	Saturation Magnetization as a Function of Temperature	33

LIST OF ILLUSTRATIONS (Continued)

<u>Fig. No.</u>		<u>Page No.</u>
23	Saturation Magnetization as a Function of Temperature	34
24	Anisotropy Field as a Function of Temperature	35
25	Anisotropy Field as a Function of Temperature	36
26	Anisotropy Field as a Function of Temperature	37
27	Anisotropy Field as a Function of Temperature	38
28	Anisotropy Field as a Function of Temperature	39
29	Anisotropy Field as a Function of Temperature	40
30	Anisotropy Field as a Function of Temperature	41
31	Anisotropy Field as a Function of Temperature	42
32	Anisotropy Field as a Function of Temperature	43
33	Anisotropy Field as a Function of Temperature	44
34	Anisotropy Field as a Function of Temperature	45
35	Saturated Insertion Phase as a Function of Temperature	47
36	Saturated Differential Phase as a Function of Temperature	48
37	Saturated Insertion Phase as a Function of Temperature	49
38	Saturated Differential Phase as a Function of Temperature	50
39	Saturated Insertion Phase as a Function of Temperature	51
40	Saturated Differential Phase as a Function of Temperature	52
41	Saturated Insertion Phase as a Function of Temperature	53
42	Saturated Differential Phase as a Function of Temperature	54
43	Saturated Insertion Phase as a Function of Temperature	55
44	Saturated Differential Phase as a Function of Temperature	56
45	Saturated Insertion Phase as a Function of Temperature	57

LIST OF ILLUSTRATIONS (Continued)

<u>Fig. No.</u>		<u>Page No.</u>
46	Saturated Differential Phase as a Function of Temperature	58
47	Saturated Insertion Phase as a Function of Temperature	59
48	Saturated Differential Phase as a Function of Temperature	60
49	Flow Chart for Production of Microwave Ferrite Material	63
50a	Photographs at 275X of 1200 Gauss Ferrite Material	72
50b	Photographs at 275X of 1200 Gauss Ferrite Material	73
50c	Photographs at 275X of 1200 Gauss Ferrite Material	74
50d	Photographs at 275X of 1200 Gauss Ferrite Material	75
51	$4\pi M_r$ vs. Density in 1200 g Li-Ti-Ferrite	87
52	Thermal Expansion Coefficient vs. Temperature for 1200 Gauss Ferrites and a Matched Dielectric	90
53	Bar of Li-Ti-Ferrite Dielectric Before Machining	91
54	Thermal Expansion Coefficient vs. Temperature for Three Expansion Matched Dielectrics	93
55	Saturated Insertion Phase as a Function of Temperature	100
56	Saturated Differential Phase as a Function of Temperature	101
57	Saturated Insertion Phase as a Function of Temperature	102
58	Saturated Differential Phase as a Function of Temperature	103

LIST OF TABLES

<u>Table No.</u>		<u>Page No.</u>
1	Composition, $4\pi M_s$ and H_a on Ferrite Materials	25
2	Temperature Dependence of Insertion Phase (Short State)	61
3	Departure from Straightness in Mils for the Steel Pins Used in Forming of Li-Ti-Ferrite Toroids	67
4	Composition and Physical Properties of Ferrite Toroids	76
5	Toroid Straightness and Physical Properties	85
6	Properties of Expansion Matching Dielectrics	92
7	Insertion Phase Temperature Coefficient	104

1.0 INTRODUCTION

Over the last quarter century, there has been a steady evolution of the nonreciprocal phase shifter used in multielement phased array radars. The original concept of using a transversely magnetized ferrite (transverse to the direction of propagation) (Fig. 1) to change the electrical length of a section of waveguide dates back to the theoretical and experimental work of the early 1950s. Differential phase shift circulators using these concepts have been employed for over 20 years and are still being designed and built for new systems.

In the 1960s, the need for multiple target tracking and missile guidance was met by using radar beams that could be electronically steered with a phased-array lens. To minimize the power needed to control each phase element, the latching phase shifter (Fig. 2) was developed. The transversely magnetized ferrite of the 1950s became a closed magnetic circuit, entirely contained within the propagating waveguide.

In the late '60s and early '70s, dielectric loading (Fig. 3) was introduced; by incorporating a high-dielectric material (e.g., K-38, $\epsilon = 38$) inside the waveguide toroid, the volume of ferrite material was significantly reduced. This produced a major cost savings by considerably decreasing the volume of the most frequently used expensive garnet materials (e.g., rare-earth elements such as yttrium and gadolinium). The reduced magnetic volume also requires less control power and represents an additional cost savings.

The most recent step in phase shifter evolution is shown in Fig. 4. The high ϵ material is no longer in the center of the toroid; it extends completely across the waveguide, while the magnetic toroid is adjacent on one side or the other. This side-loaded geometry permits the switching wires to be in a region where the microwave field is small, thereby considerably reducing the tendency to couple to higher-order modes and set up resonances within the toroid-dielectric section. It also permits additional switching wires, which gives the driver designer more options in his search for the lowest-cost configuration. In

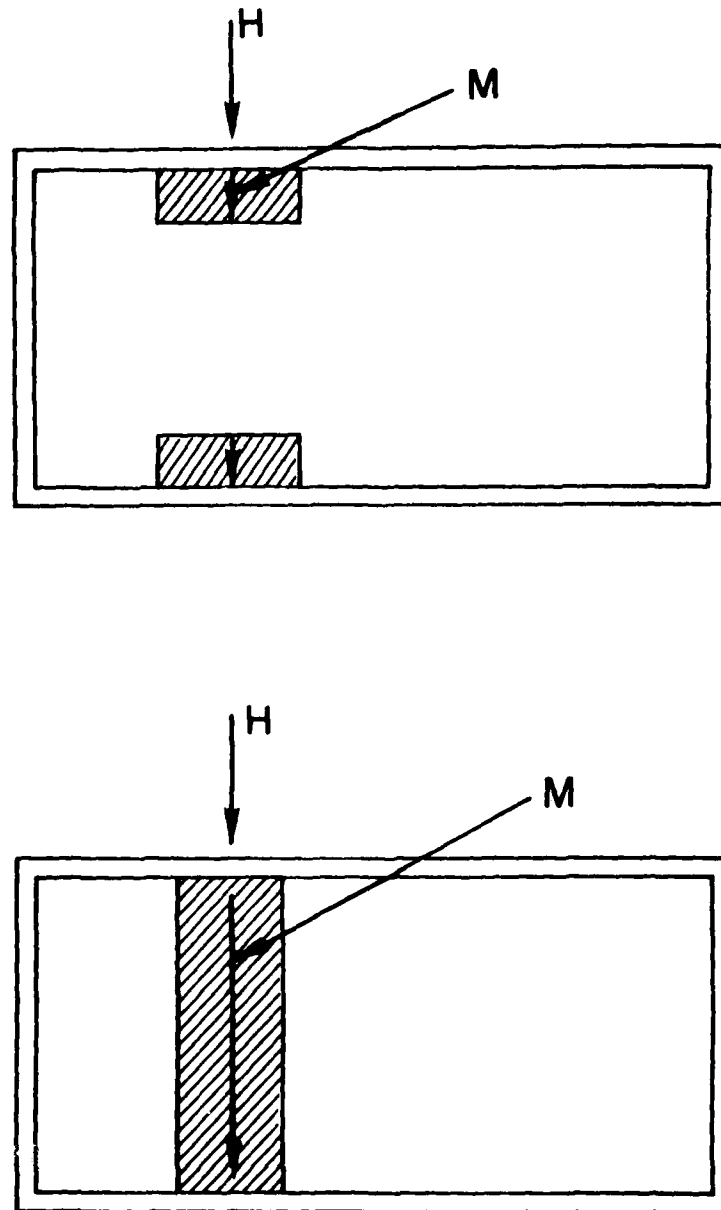


Figure 1. Early Non-Reciprocal Phase Shifters (External H).

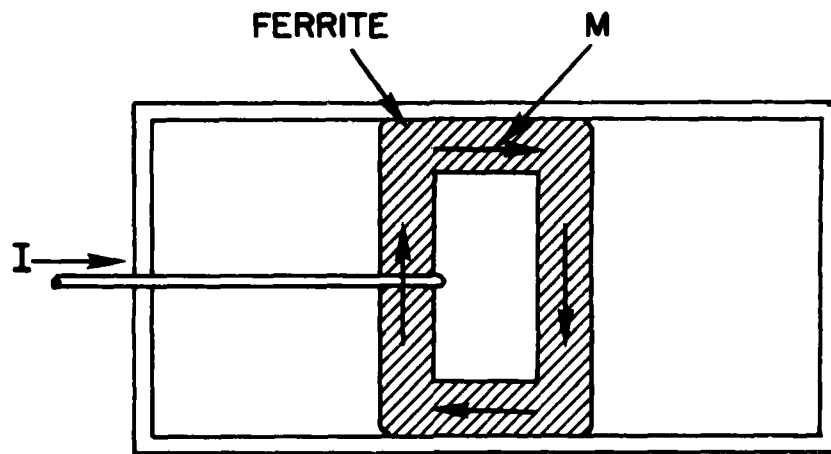


Figure 2. First Type of Non-Reciprocal Latching Phase Shifter.

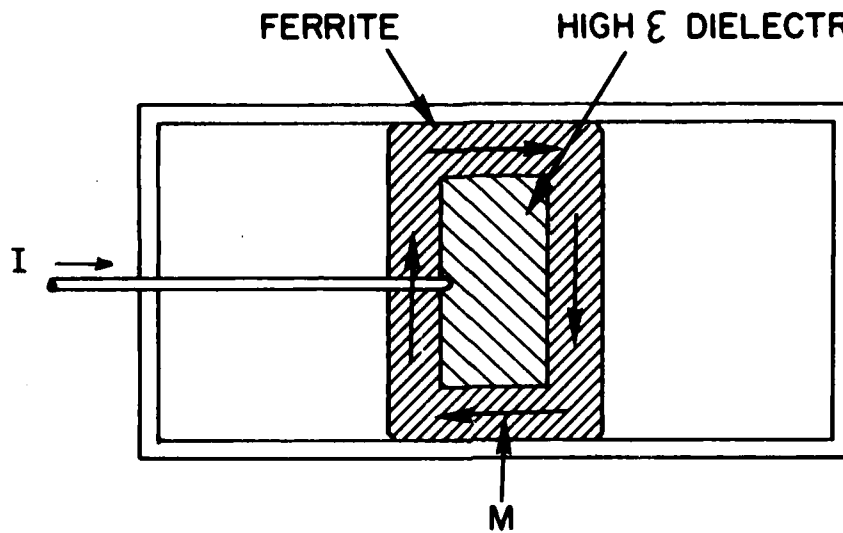


Figure 3. Non-Reciprocal Latching Phase Shifter with Dielectric Loading.

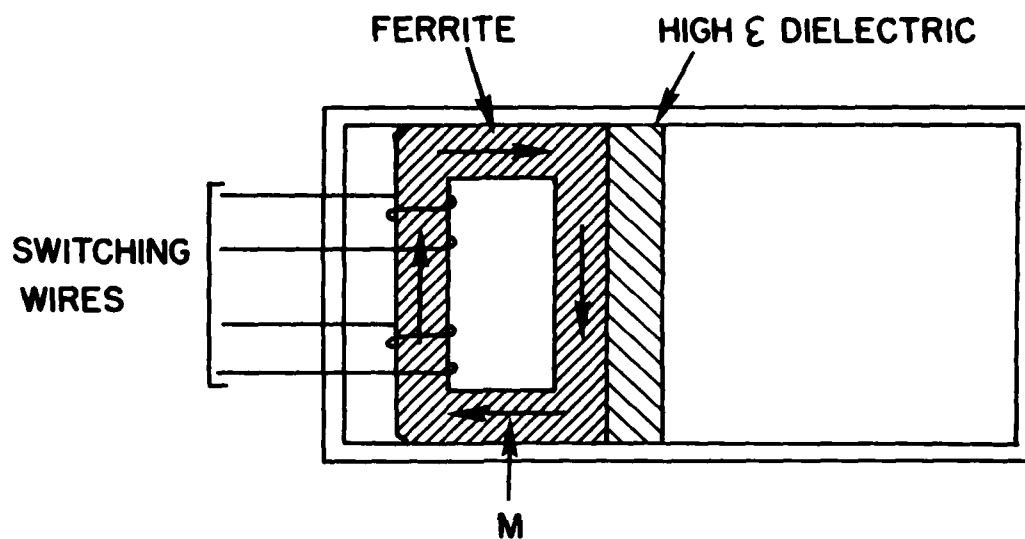


Figure 4. Non-Reciprocal Latching Phase Shifter - Side Loaded Geometry.

addition, it eliminates the painstaking fabrication steps needed to prevent air voids in coating and loading the center dielectric. Finally, the geometry is readily adaptable to phase trimming.

This most recent improvement took place between the time of our proposal submission and the start of the contract effort. Our original intention was to demonstrate the producibility of the center-loaded geometry (Fig. 3) by the fire-in-place technique (FIP) using lithium ferrite. However, when the system designers switched to the improved side-loaded geometry, Raytheon and the Army decided that the contract should focus on the producibility problems of that geometry. While some work was performed on the FIP approach, as is described in this report, most of the effort was directed at the side-loaded geometry.

In developing this side-loaded geometry, the phase-shifter designers investigated both garnet and lithium ferrite. This work showed that the garnet performance was superior because of lithium ferrite's large temperature dependence of insertion phase (Fig. 5 and Fig. 6). The LiFe composition of Fig. 6 is the one which we intended to use in this program; as the program began, however, we knew that this material was too temperature-sensitive for use in the new geometry. Furthermore, LiFe's high temperature sensitivity was unexplainable at that time. The theoretical computer model fit the garnet results very well, but did not fit the lithium ferrite results. Fortunately, we were in close contact with the phase shifter designers and immediately heard of lithium ferrite's poor performance. This gave us some time before the contract to study LiFe's temperature performance.

The clue came from χ' measurements on demagnetized samples of LiFe and garnet materials. For the same saturation magnetization, (χ'_{demag}) was larger for the LiFe, indicating that the LiFe was a more active material. This was verified by the variable-phase-shift measurement. For identical $4\pi M_s$ and sample dimensions, the LiFe gave more phase shift than did garnet. At this point, one of the authors realized that the anisotropy field, H_a , could be the source of LiFe's higher activity. If H_a is included in the dependence of the

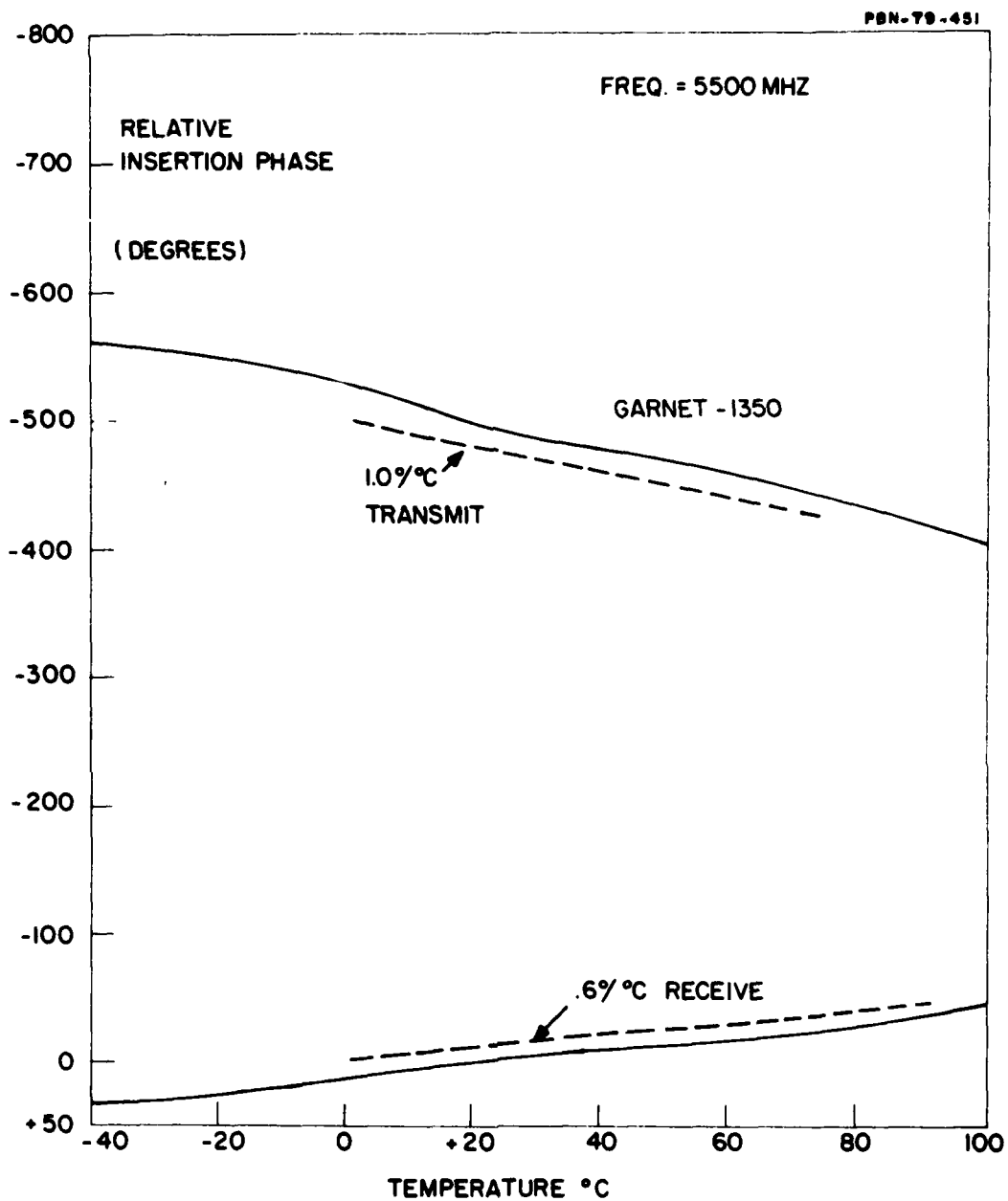


Figure 5. Saturated Insertion Phase as a Function of Temperature.

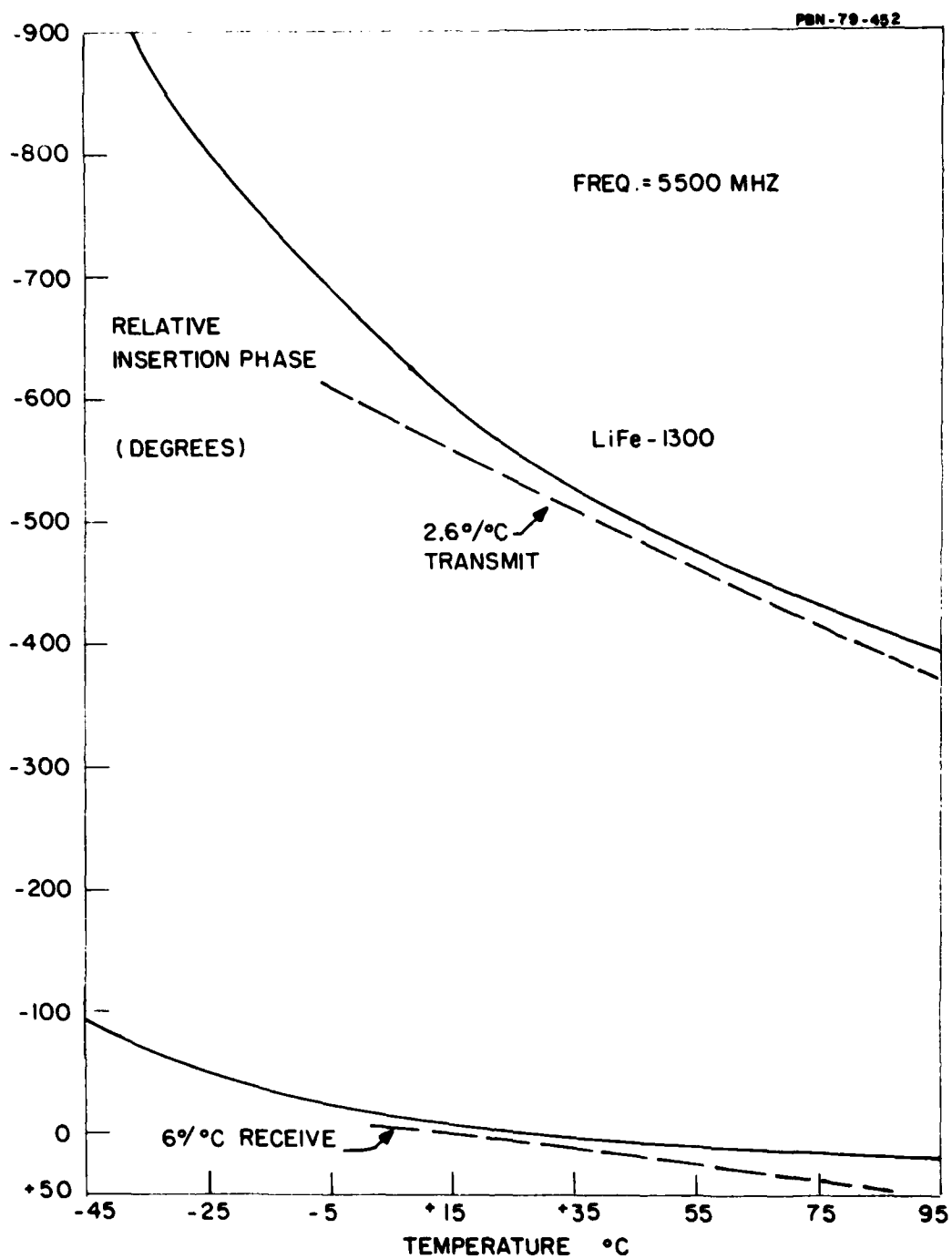


Figure 6. Saturated Insertion Phase as a Function of Temperature.

permeability components, then the computer calculations correctly give the phase shift and the temperature dependence of the insertion phase even at low temperature.

The early part of the program therefore focussed on reducing the temperature dependence by reducing the anisotropy field. Many new compositions were formulated and evaluated. Because of the difficulties in determining H_a by using either approach-to-saturation (ATS) or demagnetized $\chi'(\chi'_{\text{demag}})$, ATS and χ'_{demag} were used primarily to screen compositions. Eventually those candidates which showed the most promise were fabricated into waveguide toroids and measured in the phase-shifter configuration. A lithium-titanium-nickel-zinc composition gave the best temperature dependence and was chosen as the material to be used in the subsequent manufacture of 200 waveguide toroids. We produced 8 small (2 Kg) and 2 large (30 Kg) powder batches, from which the 200+ toroids were made.

During the early firings many variables had to be sorted out. We developed powder preparation techniques, pressing conditions, and firing schedules that gave us the necessary control over material properties such as remanent magnetization and coercive force. It was more difficult to control the dimensional properties — particularly hole straightness, which has special impact on the phase-shifting wall. Evaluation of this parameter presented a particular challenge, and required that we develop a new "pin drop test," using a series of ceramic pins. In addition, a new technique to measure wall thickness ultrasonically has shown exciting promise.

The report begins with a description of the search for a material composition having acceptable temperature dependence. It is followed by sections which describe the toroid processing and toroid verification. Then we summarize the progress that had been made on the early development of a dielectric insert composition for the fire-in-place toroid before that work was abandoned in favor of the side-loaded geometry. The evaluation of the 200+ toroids is presented next. Finally, we project the economic impact of LiFe over garnet.

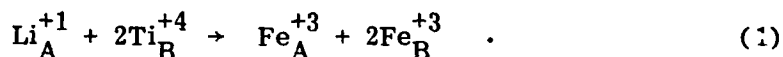
2.0 RESULTS

2.1 Lithium Ferrite Formulation

2.1.1 General considerations on cation substitutions

It is well known that the saturation magnetization ($4\pi M_s$) of lithium ferrite is reduced by Li + Ti and Al substitutions, replacing Fe^{+3} ions on the octahedral (B) cation sites. Replacement of Fe^{+3} on the tetrahedral (A) sites by Zn ions has the opposite effect of increasing $4\pi M_s$. When the substituting ion itself has a magnetic moment, as is the case with M_a , Ni, or Co, the effect on $4\pi M_s$ is less dramatic than the nonmagnetic substituents mentioned earlier.

The cation substitution process must satisfy the condition of charge balance as well as maintain the number and relative size of the ions involved. The paired substitution of Li + Ti is an example of one approach to satisfying these restrictions:

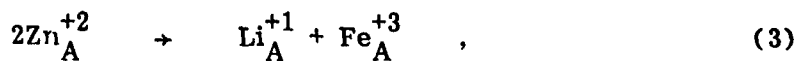


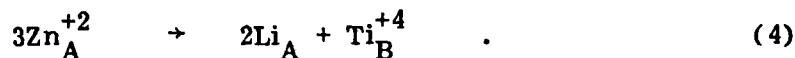
the subscripts A and B in the preceding and subsequent equations indicated the probable site locations for the cations involved. Note that the number of ions and their ionic charge on the left in (1) are balanced by the three Fe^{+3} ions being removed.

Another type of substitution in Li-ferrite that was investigated is the direct replacement of Fe^{+3} by a trivalent element such as Al, Cr, or In:



With the addition of divalent cations, we again have a charge imbalance which must be satisfied by a paired replacement of cations. Taking Zn^{+2} as an example of a divalent additive which occupies tetrahedral (A) sites in the spinel lattice, one is faced with two possible replacement schemes:





In Eq. (3) a direct replacement of A-site ions occur, but in (4) the situation is more complicated because Ti^{+4} ions normally occupy B sites (reducing $4\pi M_s$). The Zn substitution which increases $4\pi M_s$ by displacing magnetic ions on A sites may be less effective in this respect if the replacement also affects the B site occupancy.

In the case of the magnetic transition metal ions Mn, Co, and Ni, the fact that changes in $4\pi M_s$ are small means that this property is not a reliable indicator of probable site occupancy. In addition, the oxidation state of these elements is variable, lending further uncertainty in establishing substitution equations. Since Mn_2O_3 in oxygen is the stable form of the pure oxide below 1030° , we have assumed a valence of Mn^{+3} and a direct replacement of Mn^{+3} for Fe^{+3} in Li-Ti-ferrites. For Co and Ni, we have assumed a divalent oxidation state.

These relationships between number and valance of the substituting ions lead to a general spinel formula:

$$\frac{\text{Li}_{1+x-u-v-z} \text{Ti}_x \text{Mn}_y \text{Al}_w \text{Ni}_u \text{Co}_v \text{Zn}_z \text{Fe}_{5-3x-u-v-z}}{2} -w-y \quad (5)$$

where $\text{Mn}^{+3}(y)$ and $\text{Al}^{+3}(w)$ replace Fe^{+3} directly, where $\text{Li}^+ + 2\text{Ti}$ replaces $3\text{Fe}^{+3} \left(\frac{3x}{2}\right)$, and where the divalent Ni, Co, and Zn substitute half for Li^{+1} and half for Fe^{+3} .

2.1.2 Magnetization

An understanding of how the various elemental substitutions affect the magnetic moment has been of critical importance to the development of a suitable phase shifter material. The reason for this is that many cation substitutions were made primarily to influence a specific property such as dielectric loss tangent, magnetic loss, or magnetocrystalline anisotropy, but these same

substitutions also modify $4\pi M_s$. Dionne¹ has made, for a series of LiZnTi ferrite compositions, molecular field calculations of magnetization versus temperature, which have been very useful as guides of $4\pi M_s$ versus composition studies. From Dionne's calculated curves for $z = 0, 0.05, \text{ and } 0.10$ (reproduced in Fig. 7, 8, and 9), one can determine magnetic moment versus Li + Ti replacement (t) and versus Zn (z) substitution level.

The magnetic moment (n_B) in Dionne's curves is in moment per gram atom, whereas $4\pi M_s$ is in moment per unit volume, so that density corrections should be made to compare n_B directly with $4\pi M_s$. However, the compositions of interest cover such a small range in density that this correction was quite unnecessary. The value of $4\pi M_s = 1300$ gauss at Ti = 0.50 and Zn = 0, a well established experimental value, was taken as a fixed point for comparing with Dionne's calculated values. At room temperature (300°K), $4\pi M_s = 1300$ corresponds to $n_B = 0.866$. Figure 10 shows experimental data on $4\pi M_s$ at 20°C versus Ti(x) and Zn(z) content on compositions also doped with Co(v = 0.005) and Mn(y = 0.10) normalized at the 1300 gauss composition mentioned previously. The experimental data show a somewhat smaller dependence of $4\pi M_s$ on (x) than theory predicts, as shown by the difference in slope between experimental (solid) and calculated (dashed line) curves. They also show a small dependence on $4\pi M_s$ with zinc (z) level as indicated by the progressive displacement of the experimental (solid line) curves from Dionne's calculated values.

2.1.3 Anisotropy evaluation

We have made use of two techniques to estimate the anisotropy field. One is the approach to saturation (ATS), while the other uses the demagnetized susceptibility (χ'_{demag}). The law for ATS allows the magnetization M to be written in terms of the internal field H_i .

1. G. F. Dionne, "Magnetic Moment versus Temperature Curves of LiZnTi Ferrites," Lincoln Lab T Report #502, May 1974.

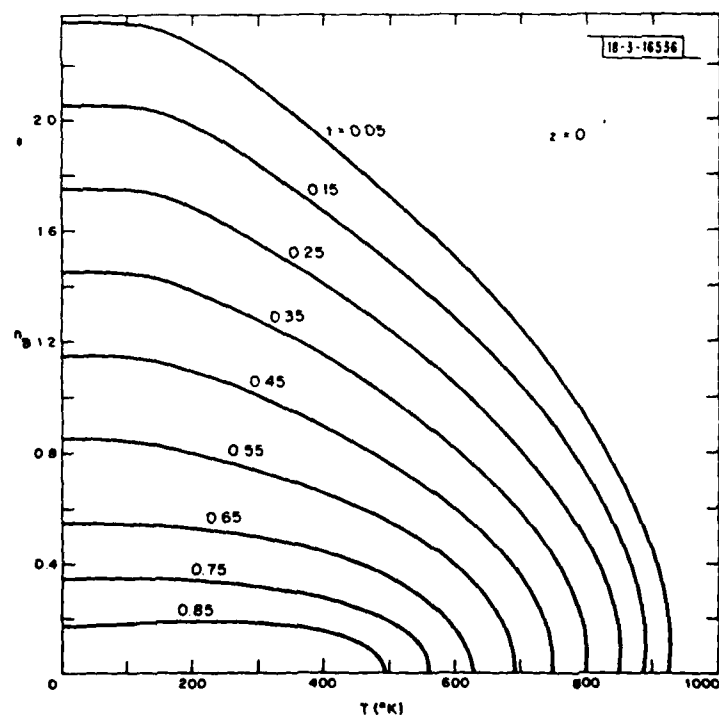
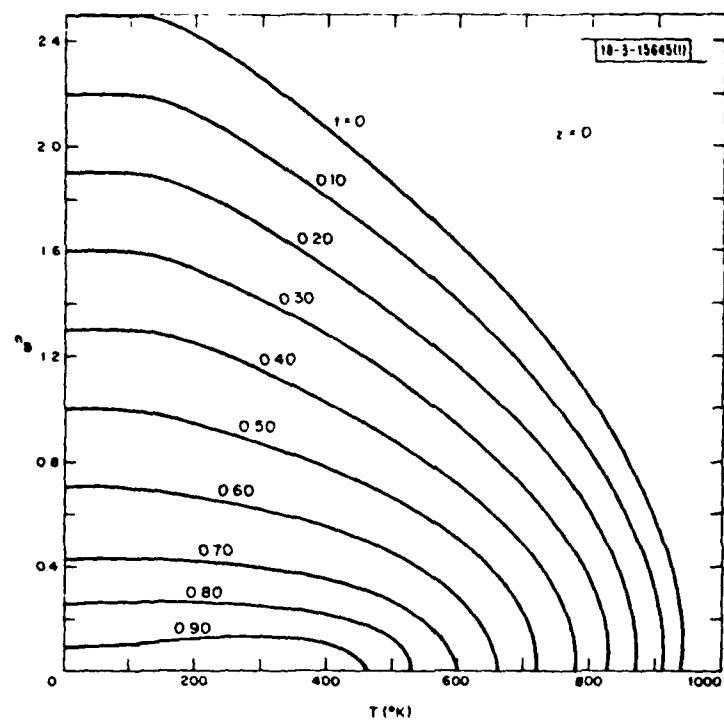


Figure 7. n_B vs. T for $z = 0$, from Dionne (1974).

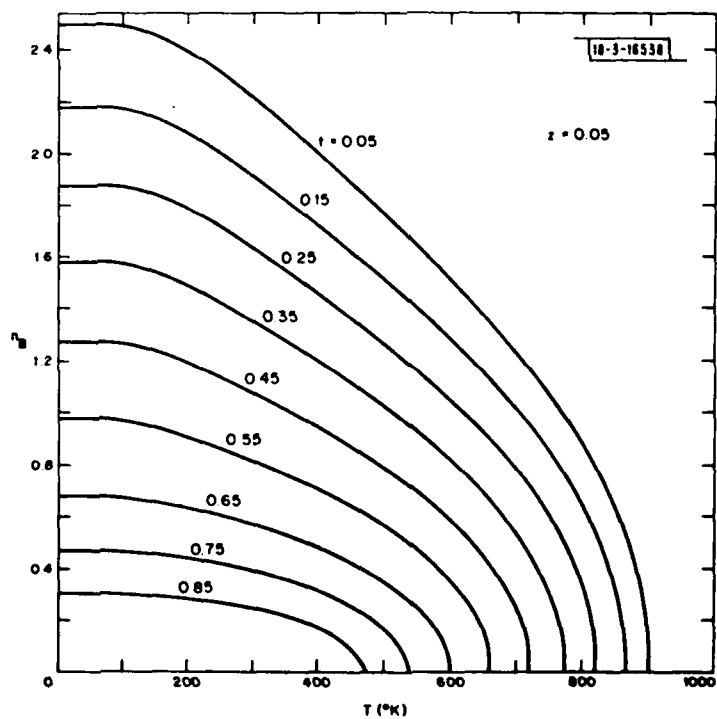
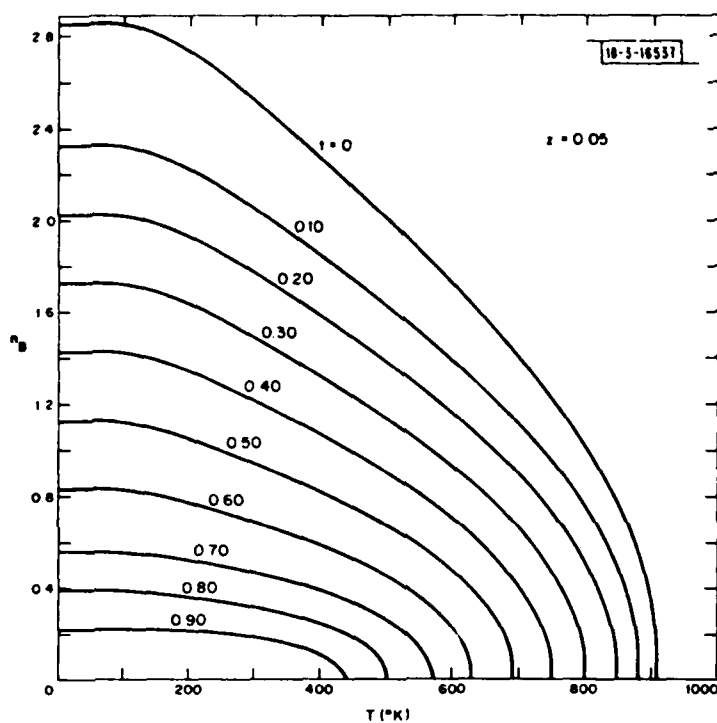


Figure 8. n_B vs. T for $z = 0.05$, from Dionne (1974).

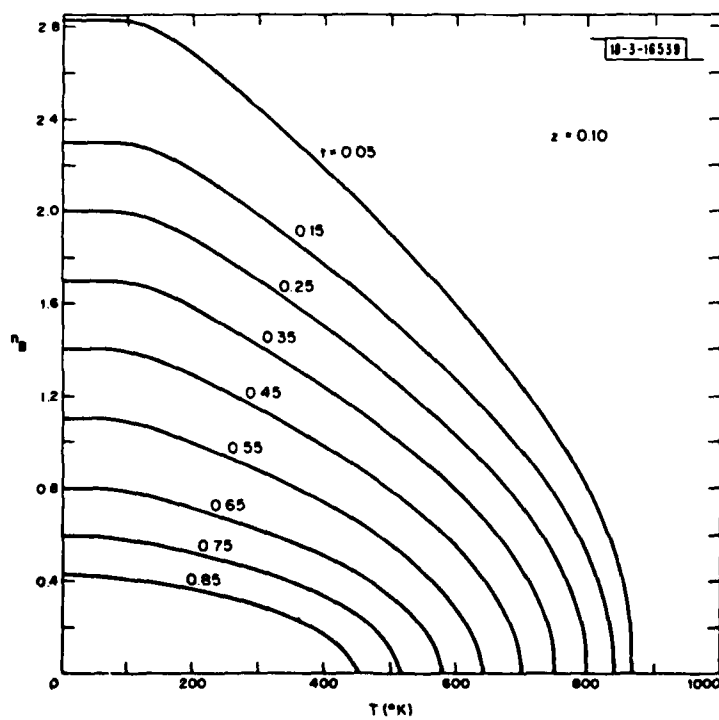
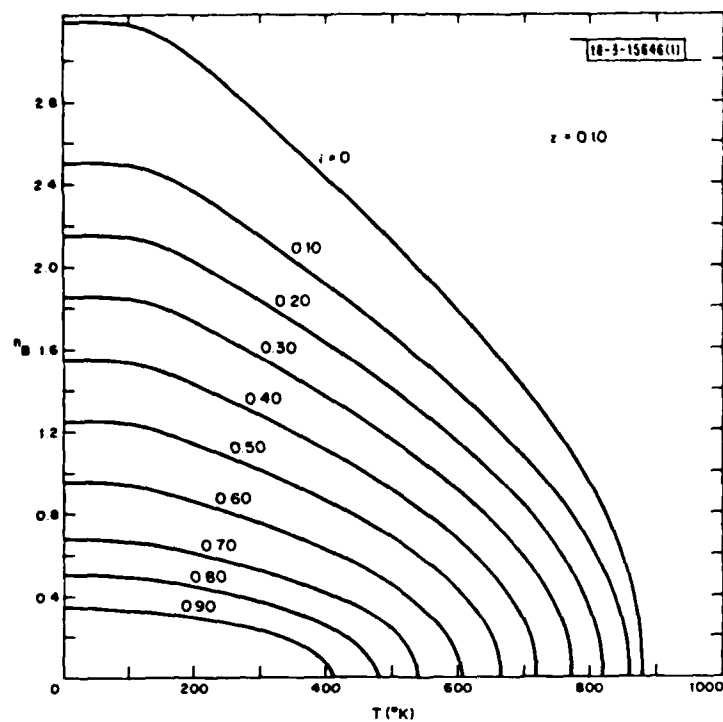


Figure 9. n_B vs. T for $z = 0.10$, from Dionne (1974).

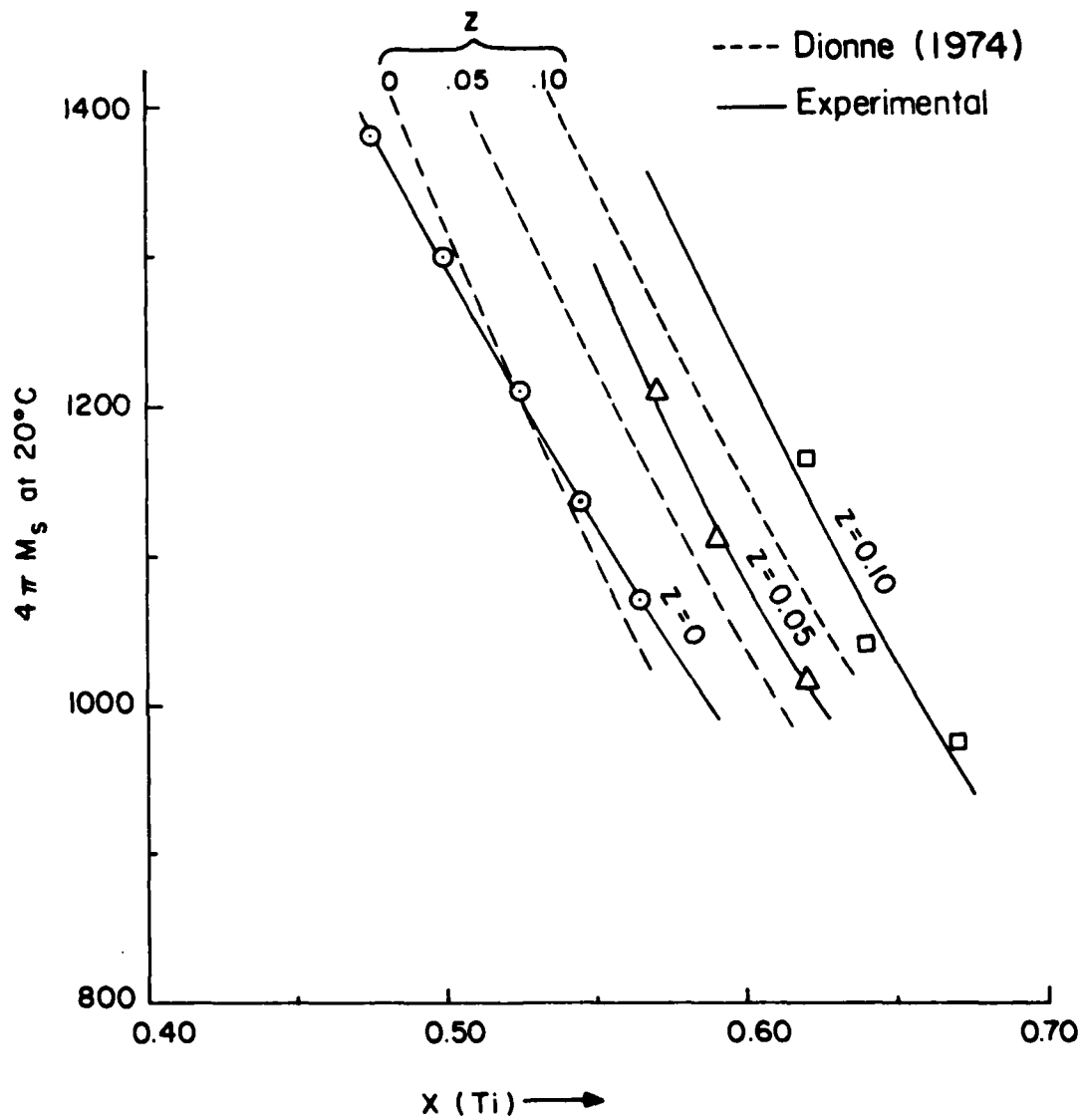
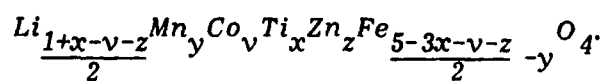


Figure 10. Magnetization vs. $\text{Ti}(x)$ Content in



$$\frac{M}{M_m} = 1 - \frac{a}{H} - \frac{b}{H^2} \dots\dots + \chi_0 H_i \quad (6)$$

χ_0 is generally very small and can be neglected.

M_m is the saturation magnetization M_s reduced by porosity. If p_{eff} is the effective porosity, then in the range $0.1 < \frac{H}{4\pi M_s} < 2$

$$a + 0.035 (4\pi M_m) \frac{p_{eff}}{1-p_{eff}} \quad (7)$$

for $H < 4\pi M_s$

$$b = \frac{1}{105} H_a^2 \quad \text{where } H_a = \frac{2K_1}{M_s} \quad (8)$$

K_1 is the first order anisotropy constant and H_a is the effective anisotropy field. For low porosity ($p_{eff} \leq (0.02)$) and values of $H_a \geq 200$ Oe, the b term dominates.

For the demagnetized case the microwave permeability μ'_{demag} ($\mu'_{demag} = 1 + \chi'_{demag}$) according to Schloemann² is given by

$$\mu'_{demag} = \frac{(\omega/\delta)^2 - H_a(H_a + 4\pi M_s)}{\left(\frac{\omega}{\delta}\right)^2 - H_a^2} \quad (9)$$

where $\omega = 2\pi$ frequency and δ = gyromagnetic ratio.

The ATS method on small spheres (2 to 3 mm diameter) uses the vibrating sample magnetometer. The magnetization is measured for small increments (~ 25 Oe) of applied field (H) up to the saturation magnetization. M is plotted against $1/H_i^2$ where H_i is the internal field ($H_i = H - \frac{4\pi M}{3}$). With the assumptions of b being dominant over a and χ_0 such plots should yield a linear region as $1/H_i^2$ approaches 0. The slope of the plot in this region is $-\frac{M_m H_a^2}{105}$ where M_m is obtained from the zero intercept. Figs. 11-16 show examples of such

2. E. Schloemann, private communication.

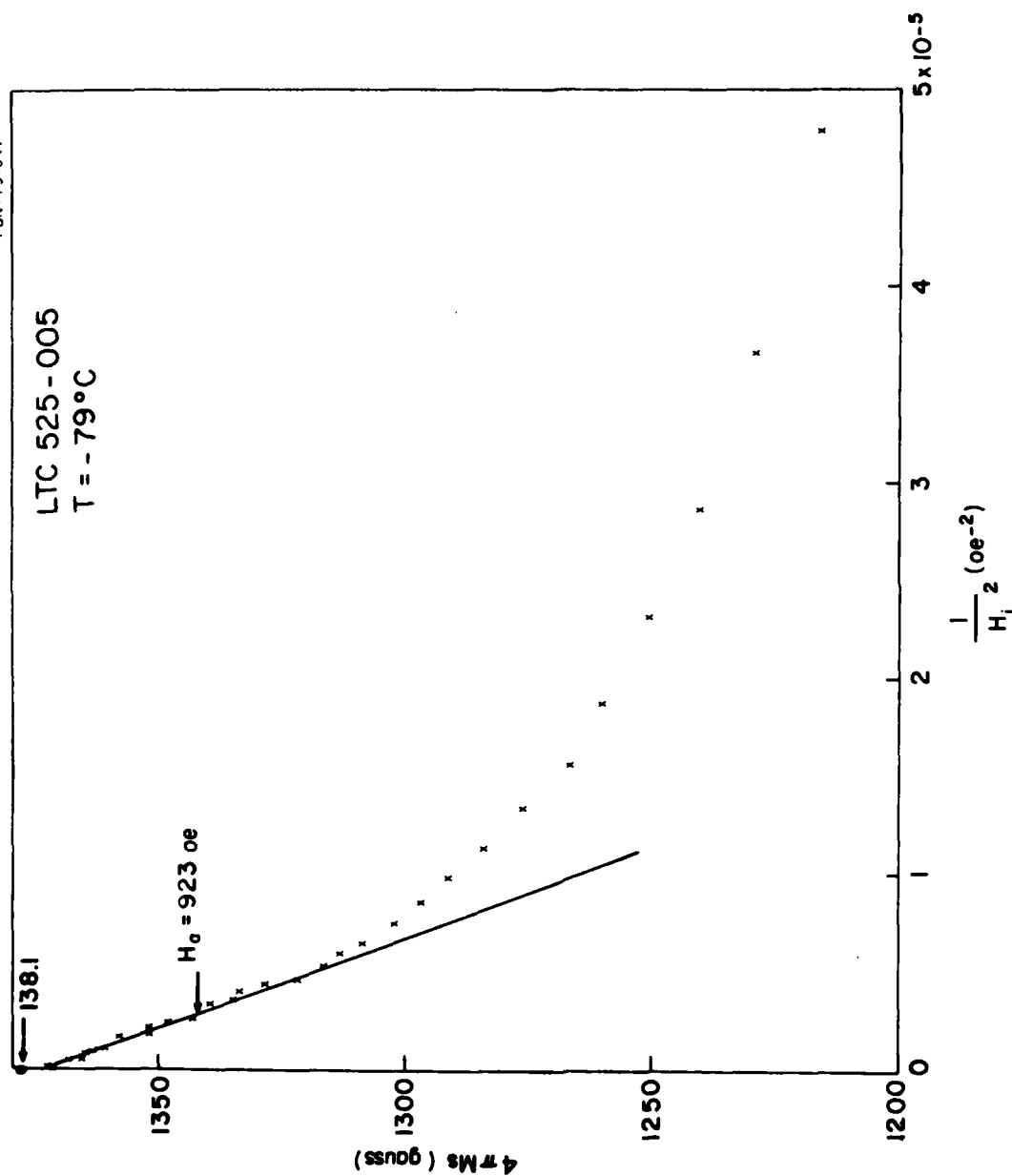


Figure 11. Anisotropy Field Determination from Magnetization Plot.

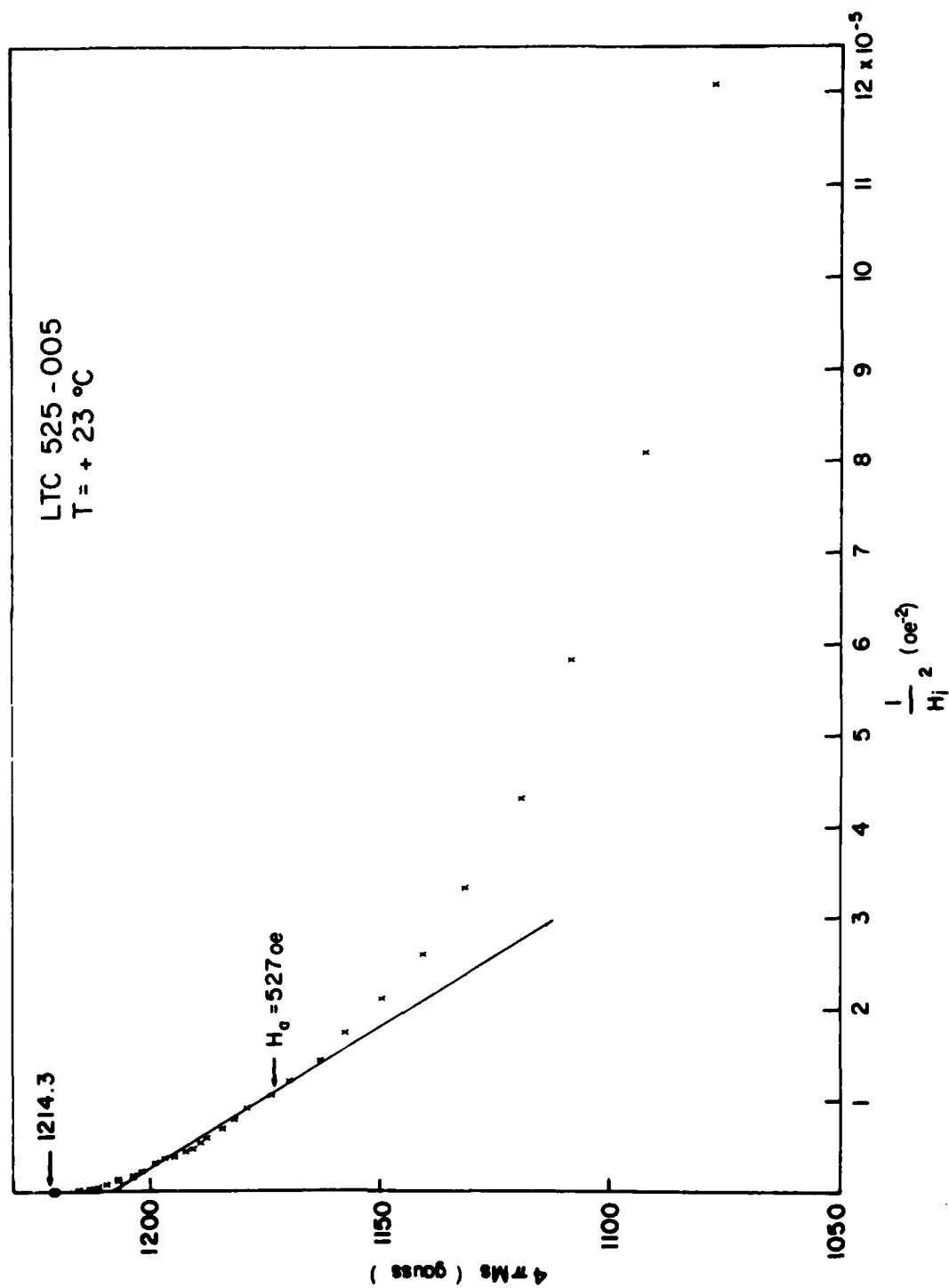


Figure 12. Anisotropy Field Determination from Magnetization Plot.

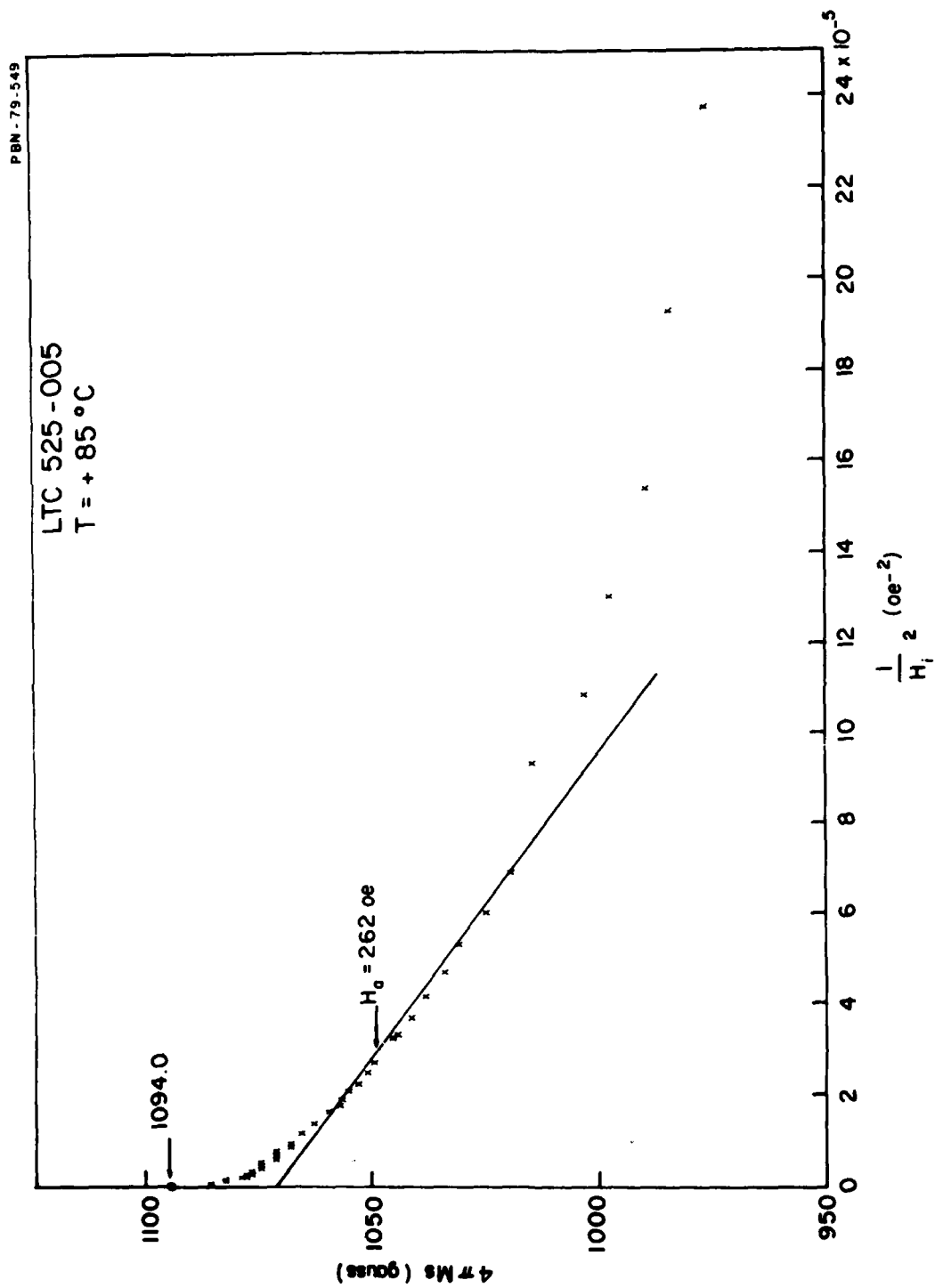


Figure 13. Anisotropy Field Determination from Magnetization Plot.

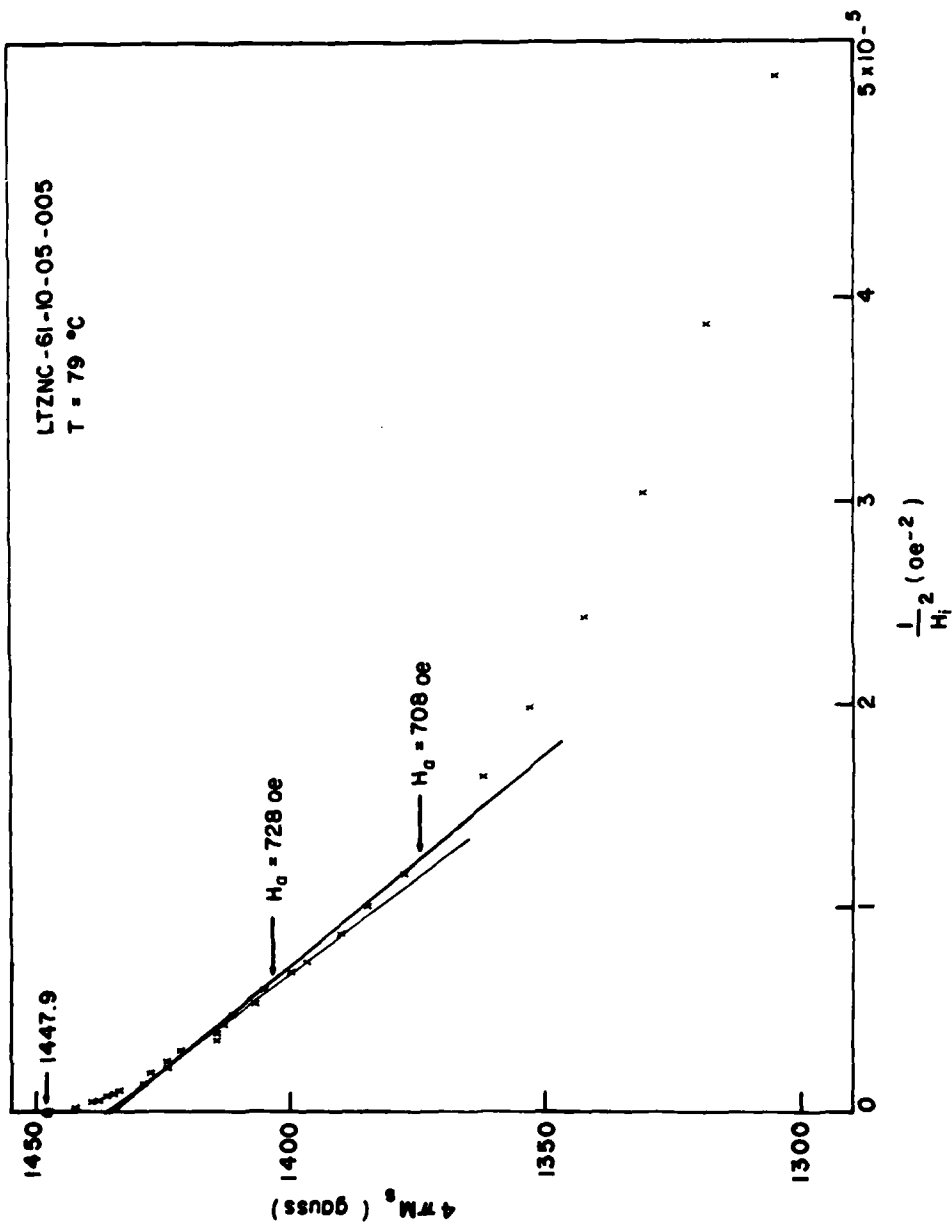


Figure 14. Anisotropy Field Determination from Magnetization Plot.

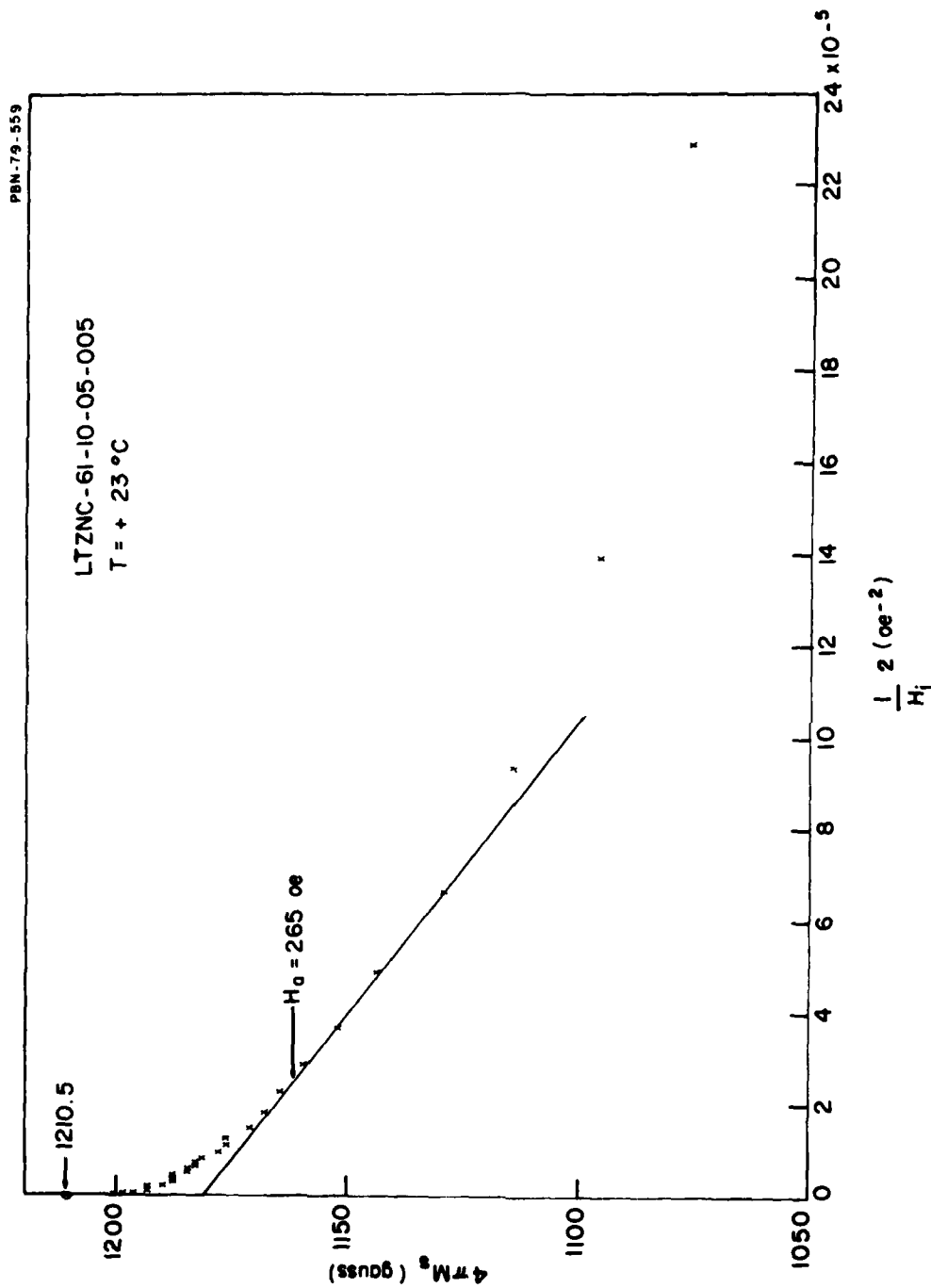


Figure 15. Anisotropy Field Determination from Magnetization Plot.

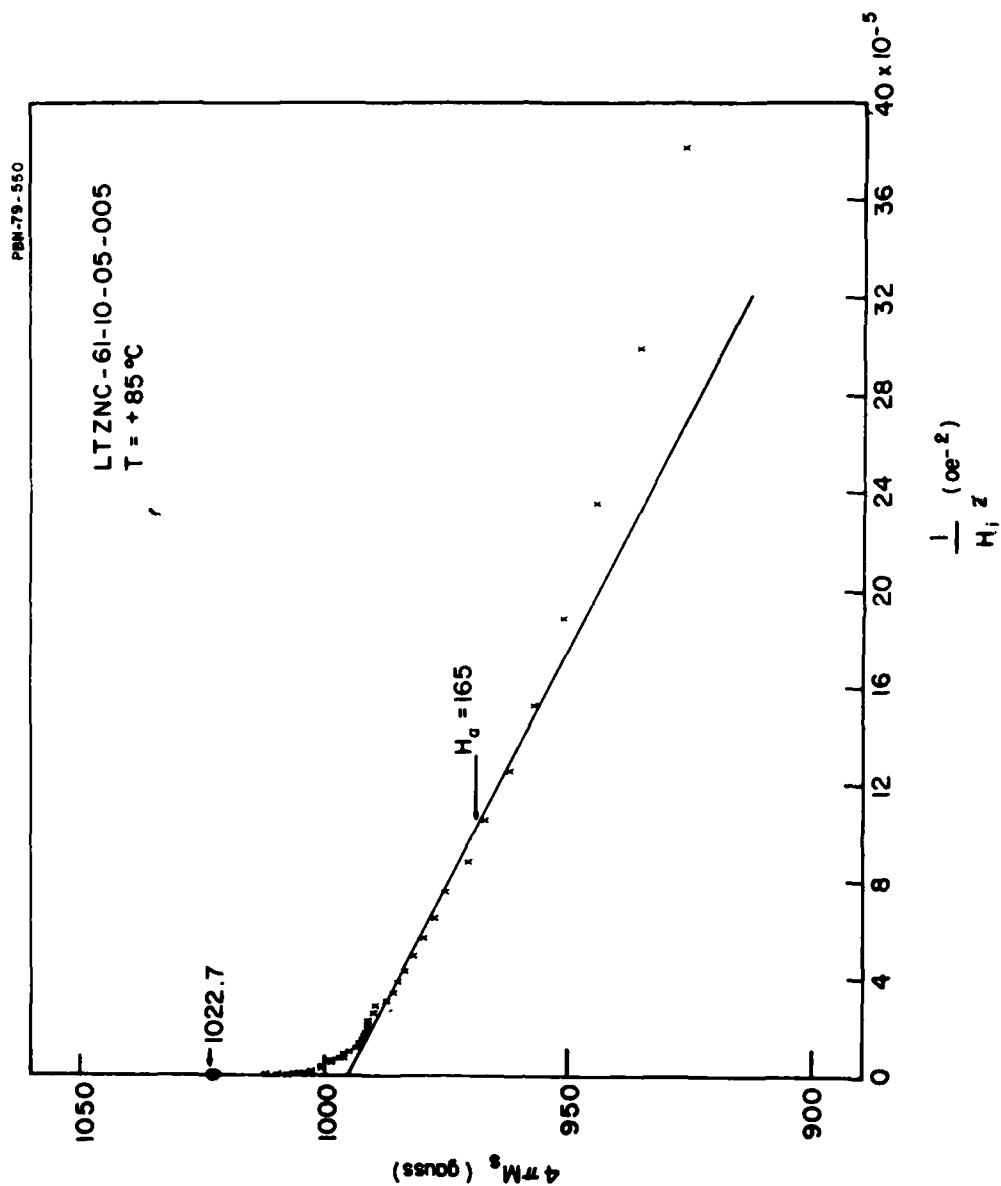


Figure 16. Anisotropy Field Determination from Magnetization Plot.

plots. Where H_a is large, ($H_a > 500$ Oe) there is a good linear slope as $\frac{1}{H_i^2}$ approaches 0 (Fig. 11) while for ($H_a < 500$ Oe), particularly for those materials with H_a about 300 Oe, the linear slope is less evident. Apparently the b term no longer is dominant. This happens in those samples which contain zinc. Some recent work by G. White³ suggests that the paramagnetic susceptibility term χ_0 can be significant in Li zinc samples. For this reason we have ignored the region near $\frac{1}{H^2} \approx 0$ and have attempted to assign a linear region for slightly larger values of $\frac{1}{H^2}$.

The χ'_{demag} are determined from the shift in a cavity resonance frequency caused by introducing the sample into a microwave cavity resonant at approximately 5.5 GHz. Even though the sample is in an E field null, there is a slight shift due to the dielectric constant of the sample. To correct for this, a nonmagnetic sample of equivalent dielectric constant ($\epsilon = 18$) is first inserted to determine the unperturbed resonance frequency.

The results of determining H_a by these two techniques are summarized in Table 1. We investigated many compositions, considering substitution of Ga, In, Cr, Al, Ni, and Zn. In almost all of these compositions there were low levels of Mn, which kept down the dielectric loss, and of Co, which raised the high power threshold. The compositions containing Al, Ni, and Zn were considered the most promising and were therefore selected for evaluation as a function of temperature. Compositions containing Ga, In, and Cr were eliminated from further consideration because these elements are very expensive and because the properties they offered could be obtained with the other substitutes. The results of the evaluation are contained in Figs. 17-34, in which the temperature dependence of $4\pi M_s$, $4\pi M_r$, $H_a(\text{ATS})$ and $H_z(\chi'_{\text{demag}})$ are given. In some of these figures it can be seen that there is a significant difference in the temperature dependence given by ATS and χ'_{demag} . Therefore, we decided to do phase shifter testing on several of these compositions. This required adding binder and hand mixing, as these powders had only been processed in small

3. G. O. White, C. A. Edmondson, R. B. Goldfarb and C. E. Patton
J. Appl. Phys. 50(3), 2381.

TABLE 1
COMPOSITION, $4\pi M_s$ AND H_a ON FERRITE MATERIALS

Composition in Atoms Per Formula Unit												
Designation	Batch Size (kg)	Li	Mn	Ti	Zn	Ni	Co	Fe	Al	Other Bi_2O_3	wt. % Bi_2O_3	Remarks
LAF 55 (2)		.500	.100					1.85	.550		.20	
LACF 55		.4975					.005	1.8475	.550		.20	1026 863 692/701
LTAC 10-57-005	0.4	.5475	.100	.100			.005	1.6775	.570		.20	1344* 748*
LTAC 25-40-10-005	0.4	.5725	.100	.250	.100		.005	1.5725	.400		.20	
LTAC 15-50-10-005	0.4	.5225	.100	.15	.100		.005	1.6225	.500		.20	
LTANC 25-30-05-005	0.4	.5375	.100	.254		.05	.005	1.5275	.300		.20	
LTN 53-05 (2)	2.2	.7650	.100	.530		.05	.005	1.555			.20	
LTZNC 57-05-05-005 (2)	2.2	.7575	.100	.570	.05	.05	.005	1.4675			.20	1167 585/660 506/591
LTC 545-005 (2)	2.2	.770	.100	.545			.005	1.580			.20	
LTNC 53-05-005 (2)	2.2	.7625	.100	.530		.05	.005	1.553			.20	
LTANC 25-30-05-005 (4)	0.4	.5975	.100	.250		.05	.005	1.6975	.300		.20	
LTAC 25-30-0025 (2)	0.4	.6238	.100	.250			.0025	1.7238	.300		.20	
LTAC 25-30-0075 (2)	0.4	.6213	.100	.250			.0075	1.7213	.300		.20	
LTZNC 61-10-05-005 (3)	2.2	.7525	.100	.610	.100	.05	.005	1.3625			.15	Decision was reached on final composition. Preparation of large batches begins.
LTZNC 61-10-05-005 (4)	2.2	.7525	.100	.610	.100	.05	.005	1.3686			.15	
LTZNC 61-10-05-005 (5)	2.2	.7525	.100	.610	.100	.05	.005	1.3686			.15	
LTZNC 61-10-05-005 (6)	2.2	.7525	.100	.610	.100	.05	.005	1.3686			.15	
LTZNC 61-10-05-005 (7)	2.2	.7525	.100	.610	.100	.05	.005	1.3686			.15	
LTZNC 61-10-05-005 (8)	2.2	.7525	.100	.610	.100	.05	.005	1.3686			.15	
LTZNC 63-10-05-005 (1)	2.2	.7375	.100	.630	.100	.05	.005	1.3775			.15	1137 284/297
LTZNC 63-10-05-005	2.2	.7375	.100	.630	.100	.05	.005	1.3637			.15	
LTM 475	3.0	.7375	.100	.475				1.6875			.20	1366 545/576
LTM 53	3.0	.760	.100	.530				1.605			.20	1163 482
LTM 50	2.2	.745	.100	.500			.010	1.645			.20	1298 487/556
LTZC 55 025-005	0.4	.775	.100	.550	.025		.005	1.560			.15	1208 513 430/449

* Quenched at 1000°C

TABLE 1
COMPOSITION, $4\pi M_s$ AND H_a ON FERRITE MATERIALS (Continued)

Composition in Atoms Per Formula Unit

Designation	Batch Size (kg)	Li	Mn	Ti	Zn	Ni	Co	Fe	Al	Other	wt. % Bi_2O_3	Remarks	$4\pi M_s$	H_a (ATS)	H_a (°)
LTZC 50-30-005	0.4	.750	.300	.500			.005	1.450			.20	M in excess of normal amount first Al sub. for Ti	1146	505/564	490/496
LTAC 50-10-005	0.4	.750	.100	.500			.005	1.550			.20			434/582	335
LTGaC 50-10-005	0.4	0.750	.100	.500			.005	1.550		.010 (Ga)	.20	these two batches had high $4\pi M_s$	1466	399/473	
LTIC 50-10-005	0.4	0.750	.100	.500			.005	1.550		.010 (In)	.20		1379	412/518	318/359
LTZC 64-10-005	0.4	0.768	.100	.640	.10		.005	1.388			.20	remake of comp. 20 with small % Ti contract	1063	238/297	266/269
LTA 25-30	0.4	.625	.100	.250				1.725	.30		.20		1157/1176	578/596	560
LTA 40-15	0.4	.700	.100	.400				1.650	.15		.20		1341*	493	476/511
LAF 55 (1)	0.4	.50	.100					1.85	.550		.20		1163	558	771/812
LCrF 55 (1)	0.4	.50	.100					1.85		.550 (Cr)	.20		1272	---	619/624
LIF 55 (1)	0.4	.50	.100					1.85		.550 (In)	.20		2295	---	---
LTZC 61-10-005 (2)	2.2	.725	.100	.610	.100		.005	1.4325			.15		1410	441/521	266/284
LTZC 61-10-005 (3)	2.2	.7525	.100	.610	.100		.005	1.4325			.15				
LTZNC 61-10-05-005(1)	0.4	.7525	.100	.610	.10	.05	.005	1.3825			.20	First processing of Ni doped compositions Assuming substitution as Ni^{+3}	1143/1272	210/325	---
LTZNC 57-05-05-005(1)	0.4	.7525	.100	.570	.05	.05	.005	1.4675			.20		1225	370	213/221
LTNC 53-05-005	0.4	.7625	.100	.530		.05	.005	1.5525			.20				
LTN 53-05	0.4	.7650	.100	.530		.05		1.555			.20				
LTAC 25-30-005	0.4	.6225	.100	.250			.005	1.7225	.30		.20		1317	475	415/435
LTZAC 25-35-10-01	0.4	.57	.100	.250	.100		.005	1.820	.35		.20				
LTAC 25-30-005	0.4	.62	.100	.250	.100		.005	1.720	.30		.20				
LTZC 61-10-005 (5)	2.2	.7525	.100	.610	.100		.005	1.4325			.15	higher calcine temperature than normal ($\pm 35^\circ$)			
LTZNC 61-10-05-005(2)	2.2	.7525	.100	.610	.100	.05	.005	1.3825			.15				
LTAC 25-30-0025		.6238	.100	.250			.0025	1.7230	.300		.20	beginning of studies of Al doped materials	1344	625	357
LTAC 25-30-0075		.6213	.100	.250			.0075	1.7213	.300		.20		1308	589	429/447

* Quenched at 1000°C

TABLE 1

COMPOSITION, $4\pi M_s$ AND H_a ON FERRITE MATERIALS (Continued)

LITHIUM FERRITE COMPOSITIONS

Composition in Atoms Per Formula Unit

Designation	Batch Size (kg)	Li	Mn	Ti	Zn	Ni	Co	Fe	Al	Other	wt. % Bi_2O_3	Remarks	$4\pi M_s$	H_a /ATS	H_a / H_c
LTC 50-05-005 (1)	0.4	.7225	.100	.500	.050		.005	1.6225			.15	Bi_2O_3 added initially			
LTC 50-05-005 (2)	0.4	.7225	.100	.500	.050		.005	1.6225			.15	Bi_2O_3 added in final milling			
LTC 57-05-005 (1)	0.4	.760	.100	.570	.050		.005	1.515			.15	Normal processing (one 850°C 5 hour calcine and two millings.)	1224	423	402
LTC 57-05-005 (2)	0.4	.790	.100	.570	.050		.005	1.515			.15				
LTC 53-05-005 (1)	2.2	.7375	.100	.530	.050		.005	1.5775			.20	two 850°C calcines and three millings 55 powder in top sagger appeared more reacted (darker) than 53			
LTC 55-025-005 (1)	2.2	.760	.100	.550	.025		.005	1.56			.20				
LTC 53-005 (1)	2.2	.765	.100	.530			.005	1.605			.20	(1) had normal millings in methanol			
LTC 53-005 (2)	2.2	.765	.100	.530			.005	1.605			.20	(2) had second milling in demin. H_2O			
LTC 57-05-005 (3)	0.4	.7575	.100	.570	.050		.005	1.5175			.20	series of experimental compositions to study effect of Ti(x) and Zn(z) on properties			
LTC 82-10-005 (1)	0.4	.7575	.100	.62	.100		.005	1.4175			.20		1180	291/321	308/333
LTC 82-05-005 (1)	0.4	.7825	.100	.62	.050		.005	1.4425			.20		1024	384	345/373
LTC 87-10-005 (1)	0.4	.7825	.100	.67	.100		.005	1.3425			.20		984	294	284/321
LTC 525-005	0.4	.760	.100	.525			.005	1.610			.20		1266	444	412/482
LTC 55-025-005	0.4	.760	.100	.550	.025		.005	1.560			.20				
LTC 565-005	0.4	.780	.100	.565			.005	1.550			.20		1084	485/613	422/441
LTC 59-025-005	0.4	.780	.100	.590	.025		.005	1.500			.20		1057	514	422/444
LTC 545-005	0.4	.770	.100	.545			.005	1.580			.20				
LTC 57-025-005	0.4	.770	.100	.570	.025		.005	1.530			.20		1136	443	374/405
LTC 59-05-005	0.4	.7675	.100	.590	.050		.005	1.4875			.20		1127	420	435/460
LTC 87-10-005	0.4	.7825	.100	.670	.100		.005	1.3425			.20				

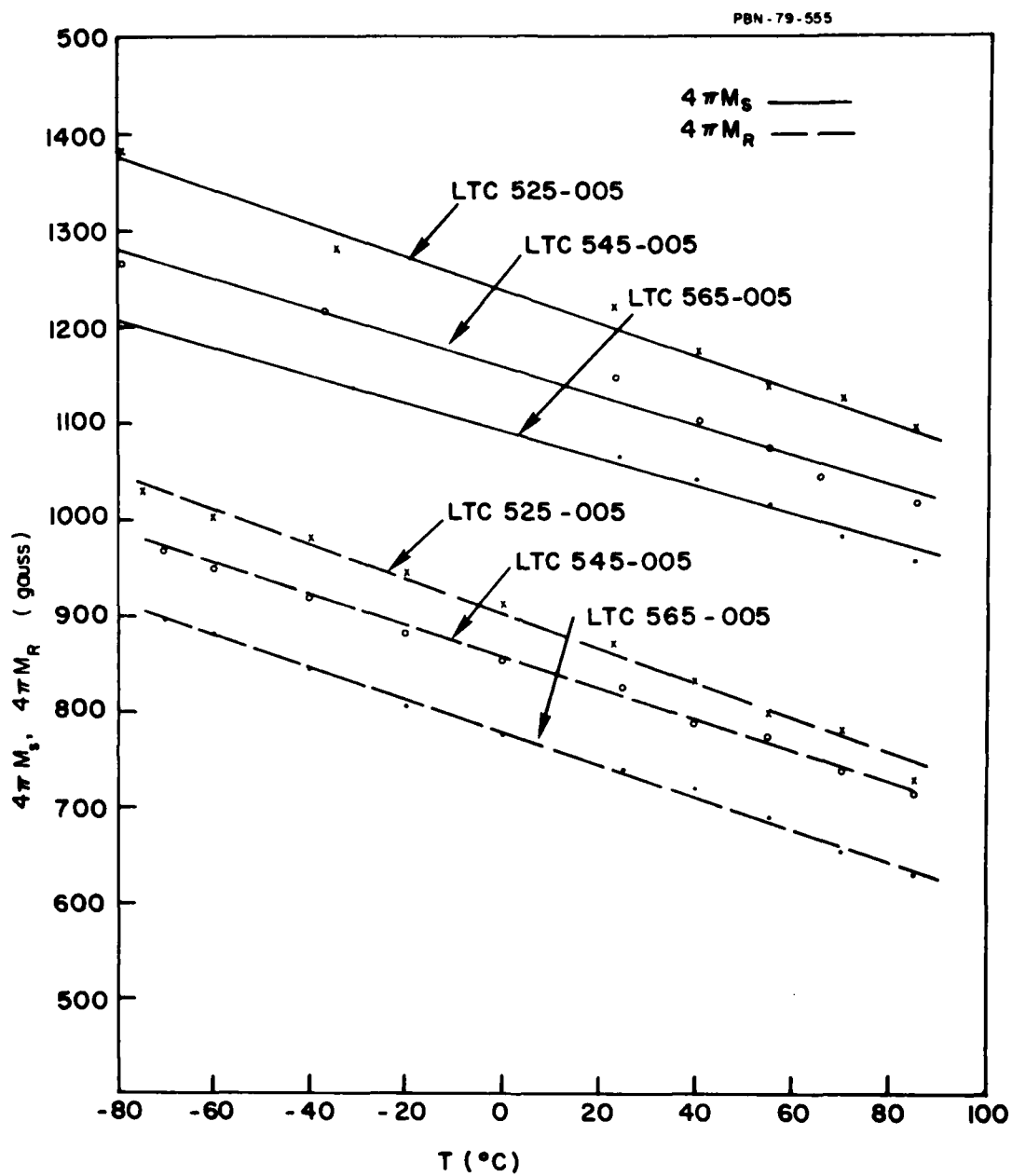


Figure 17. Saturation Magnetization as a Function of Temperature.

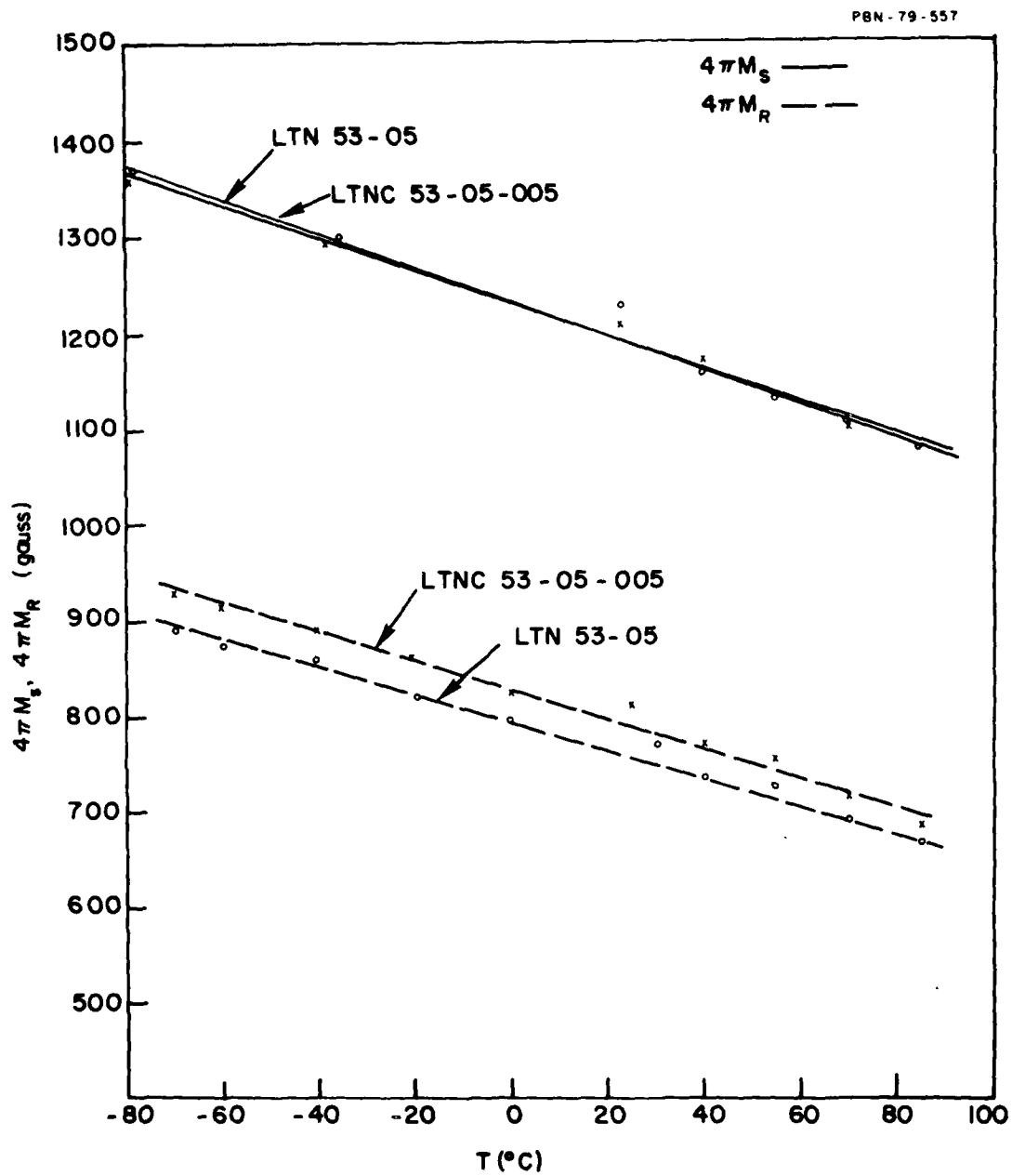


Figure 18. Saturation Magnetization as a Function of Temperature.

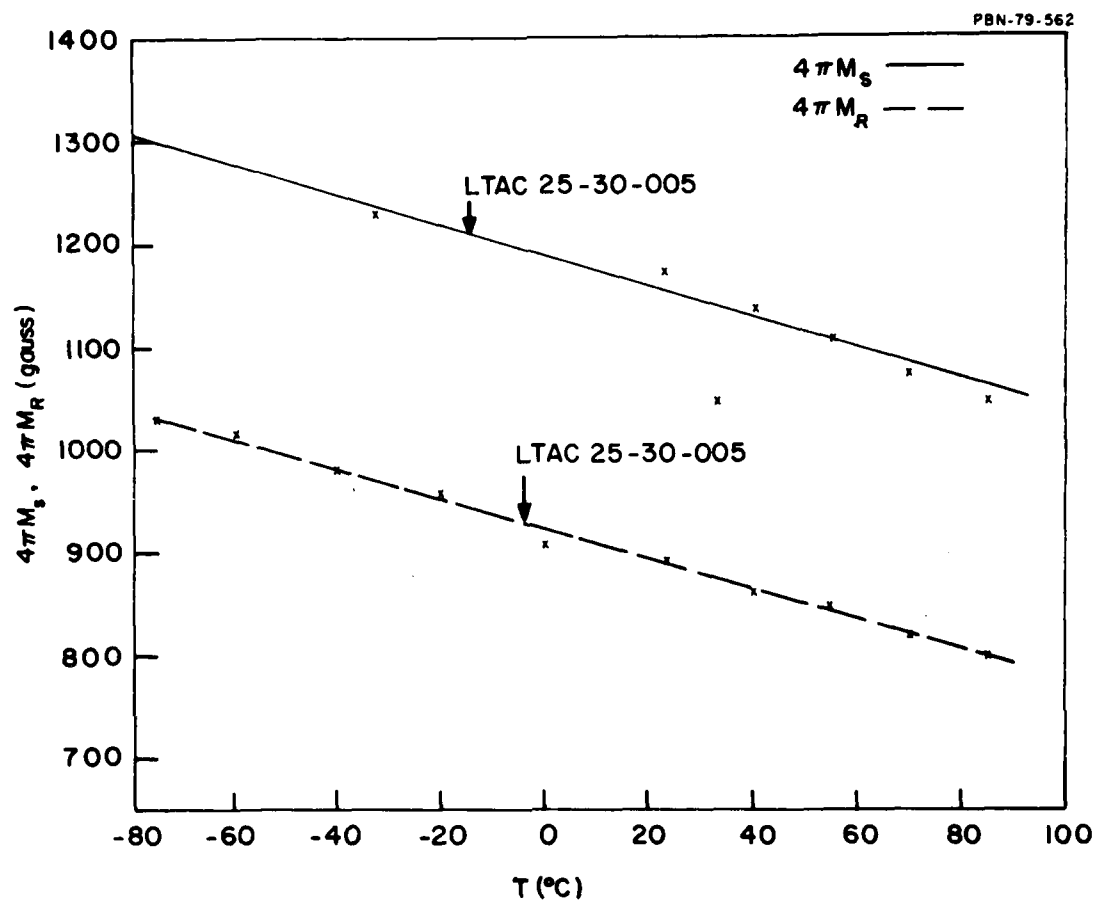


Figure 19. Saturation Magnetization as a Function of Temperature.

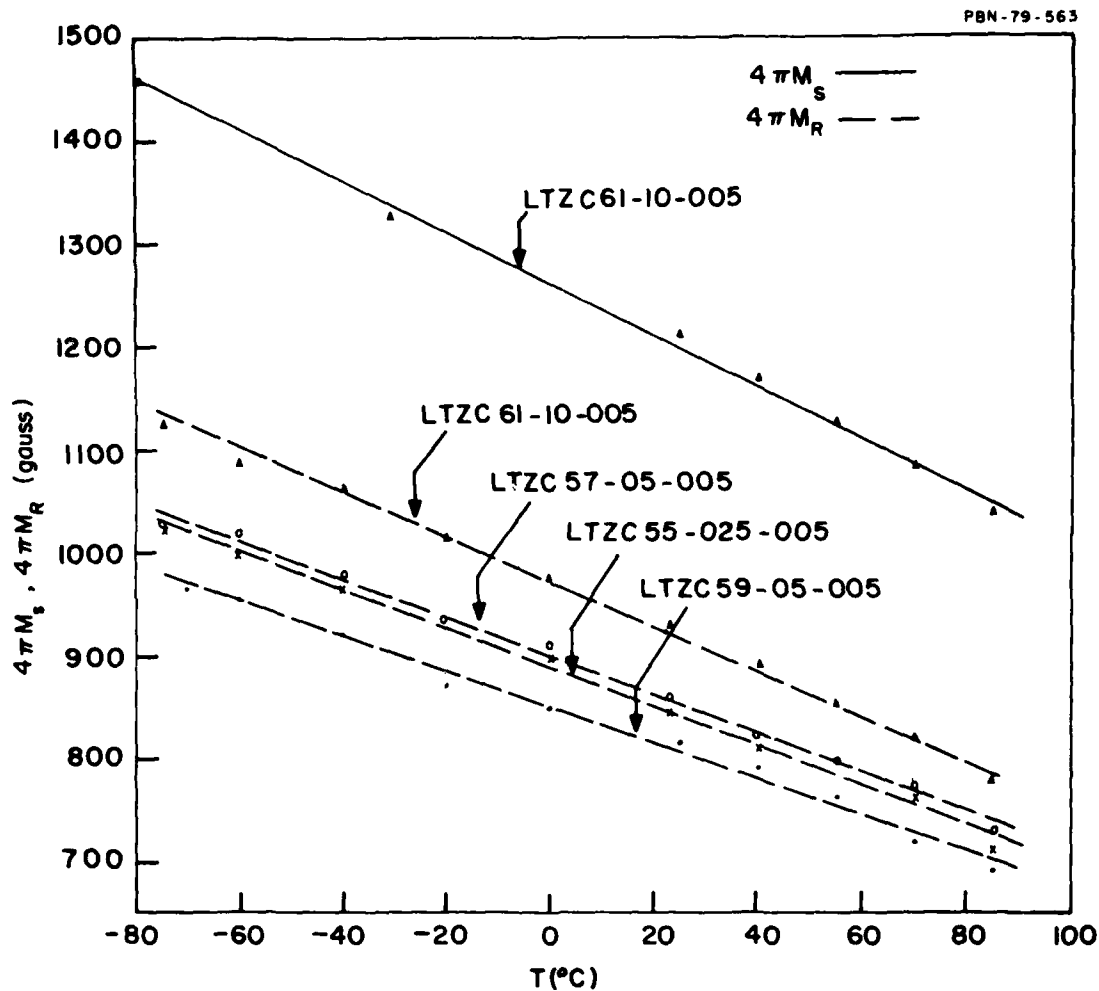


Figure 20. Saturation Magnetization as a Function of Temperature.

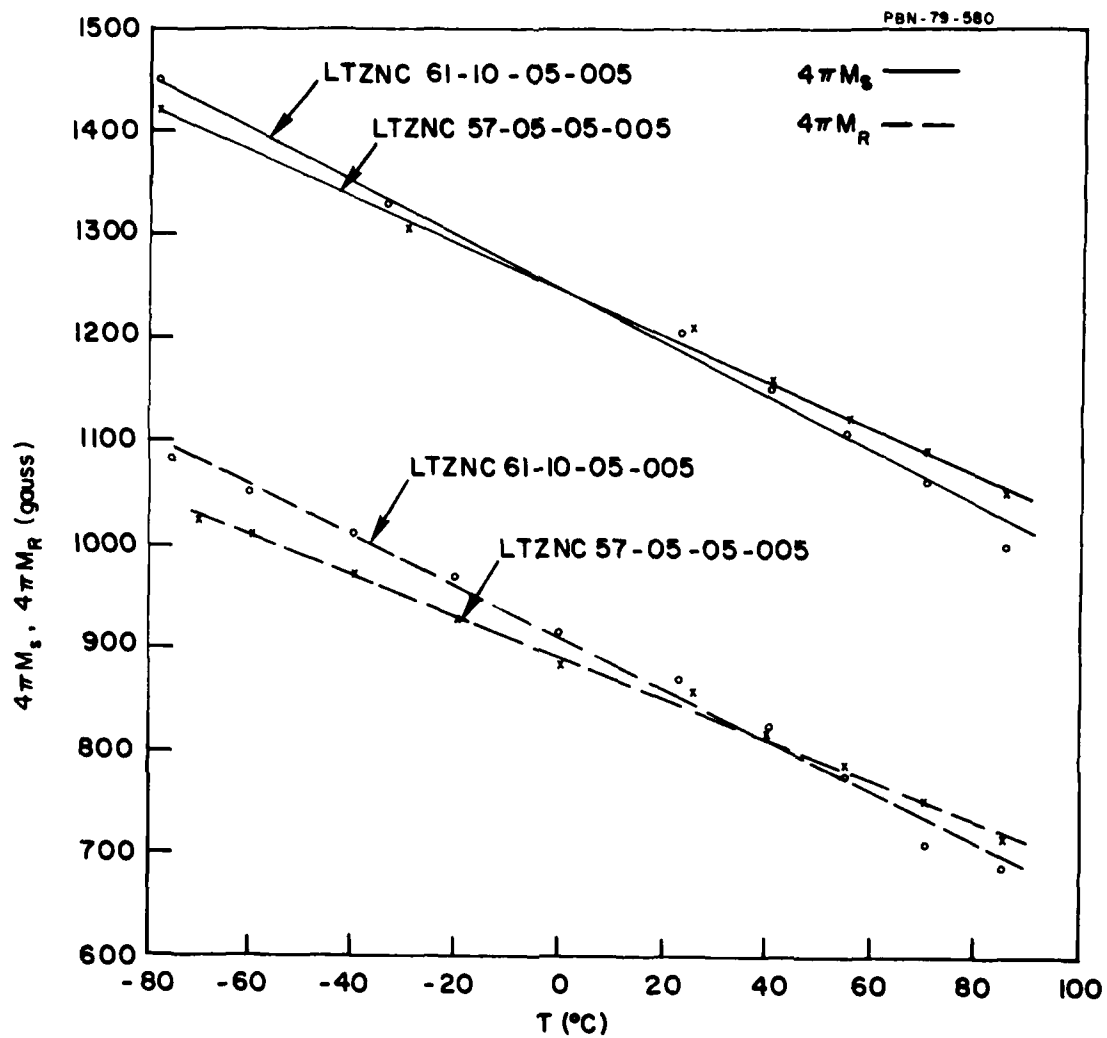


Figure 21. Saturation Magnetization as a Function of Temperature.

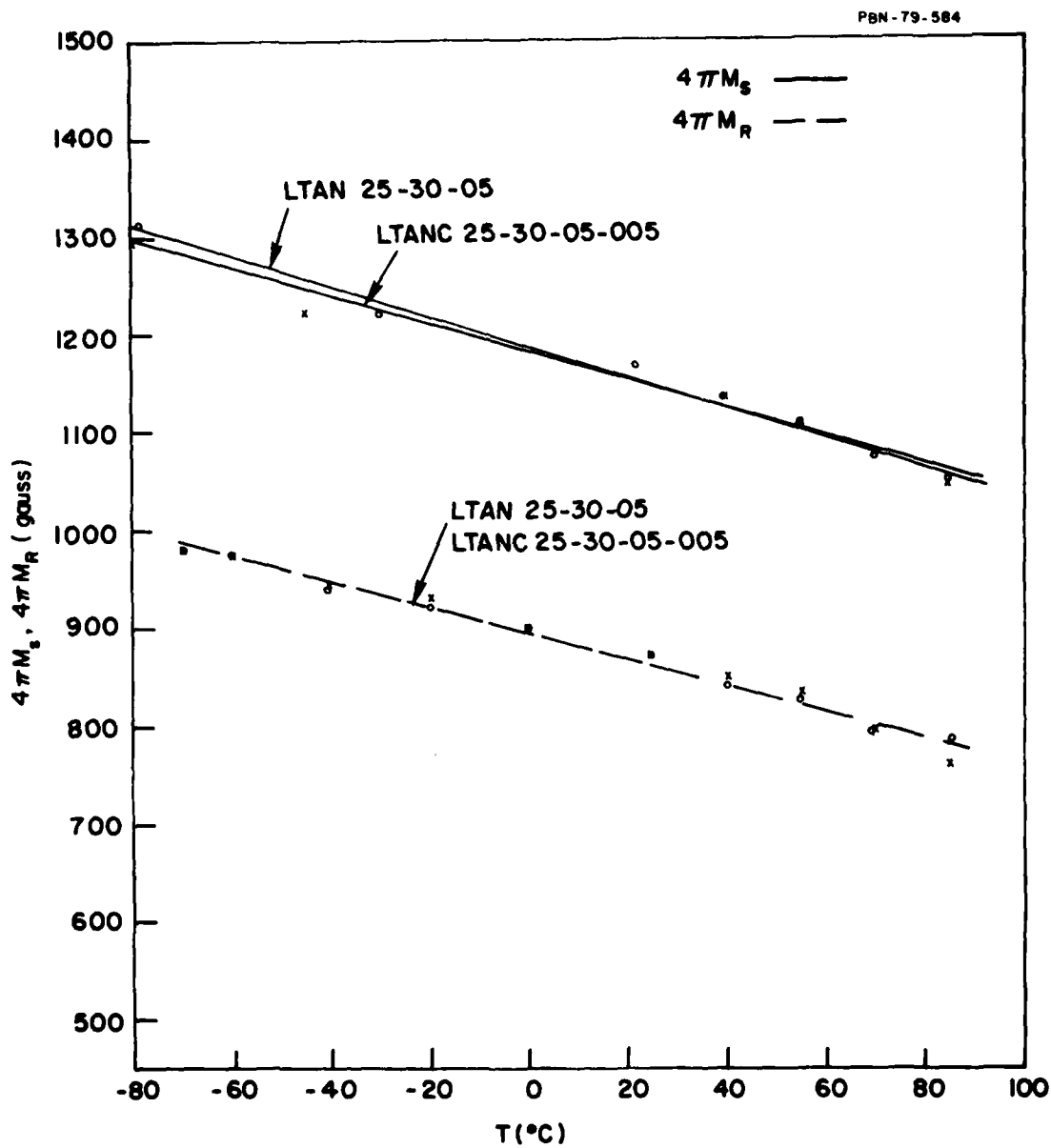


Figure 22. Saturation Magnetization as a Function of Temperature.

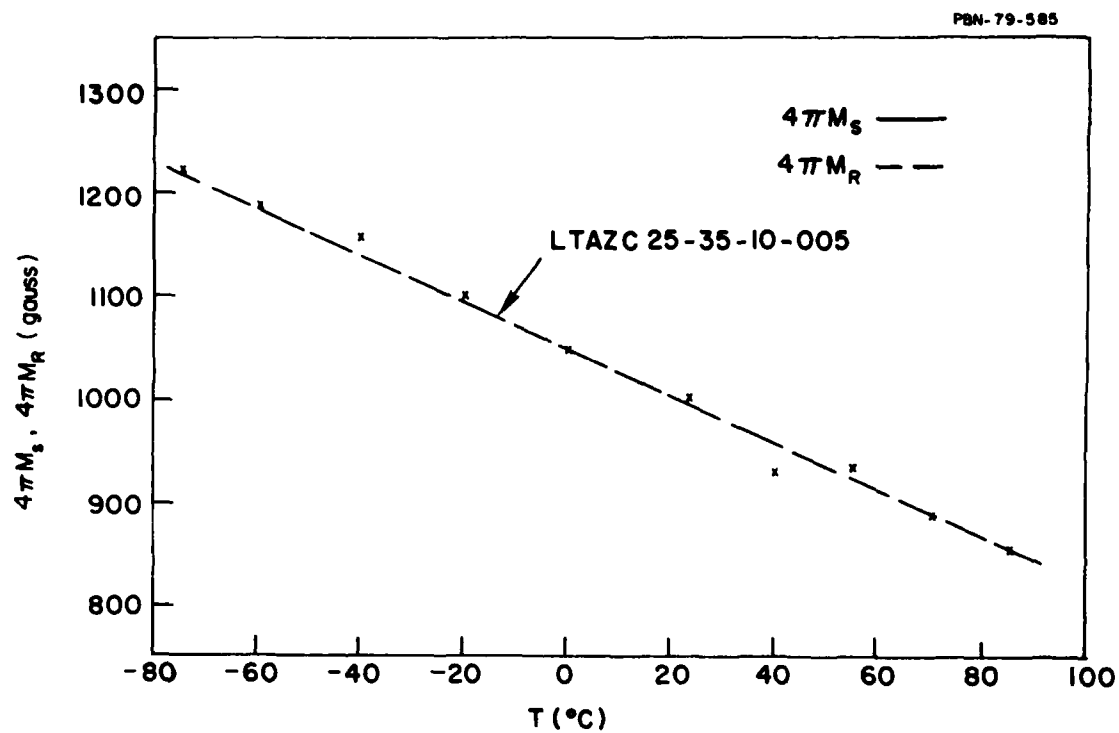


Figure 23. Saturation Magnetization as a Function of Temperature.

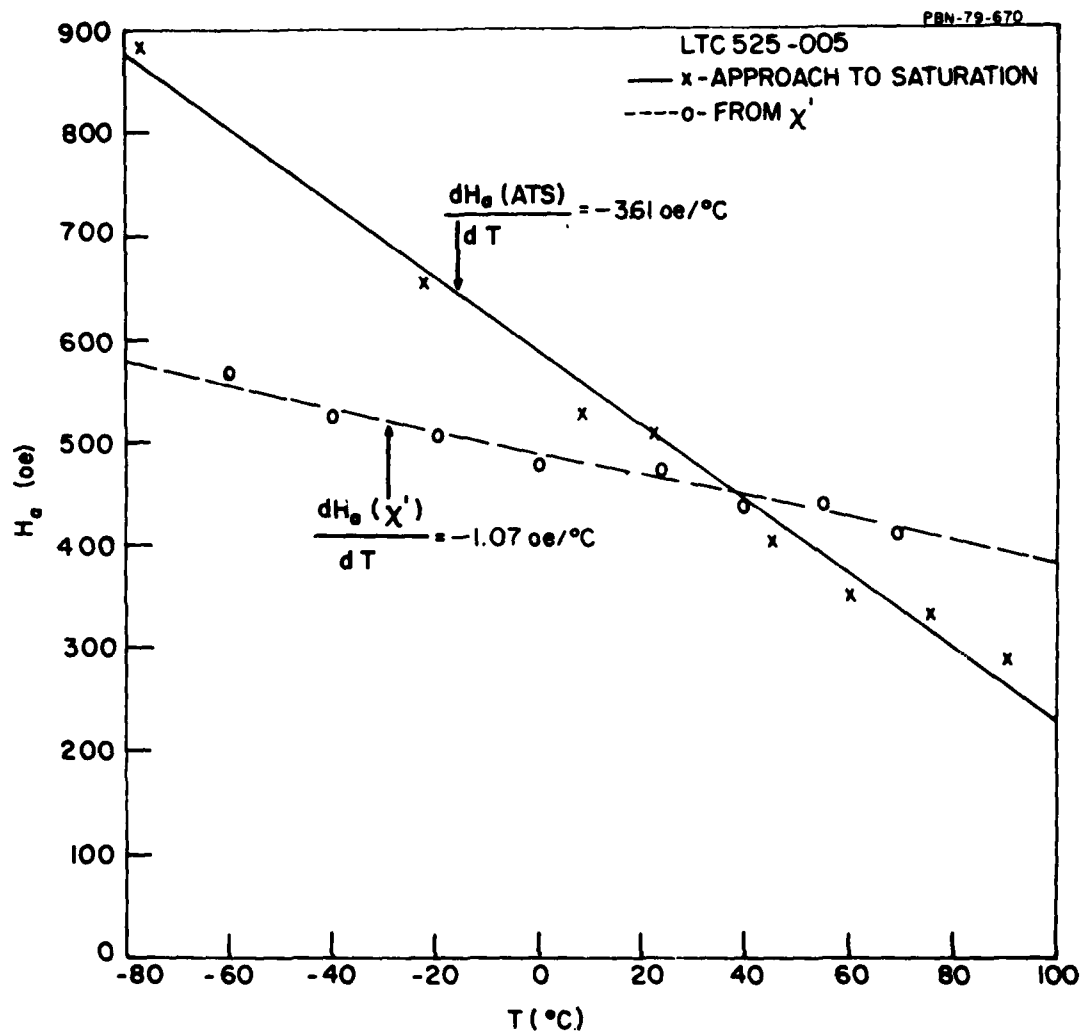


Figure 24. Anisotropy Field as a Function of Temperature.

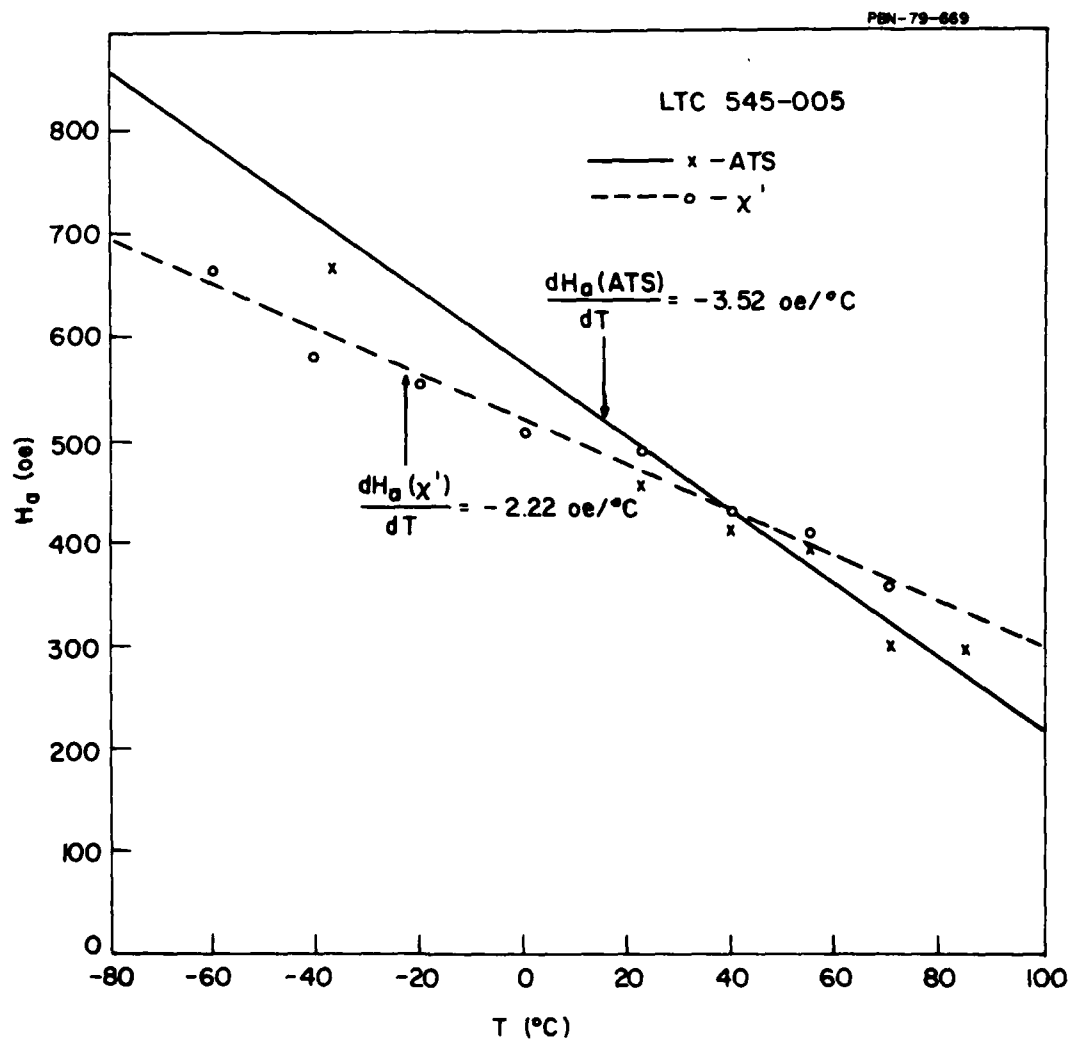


Figure 25. Anisotropy Field as a Function of Temperature.

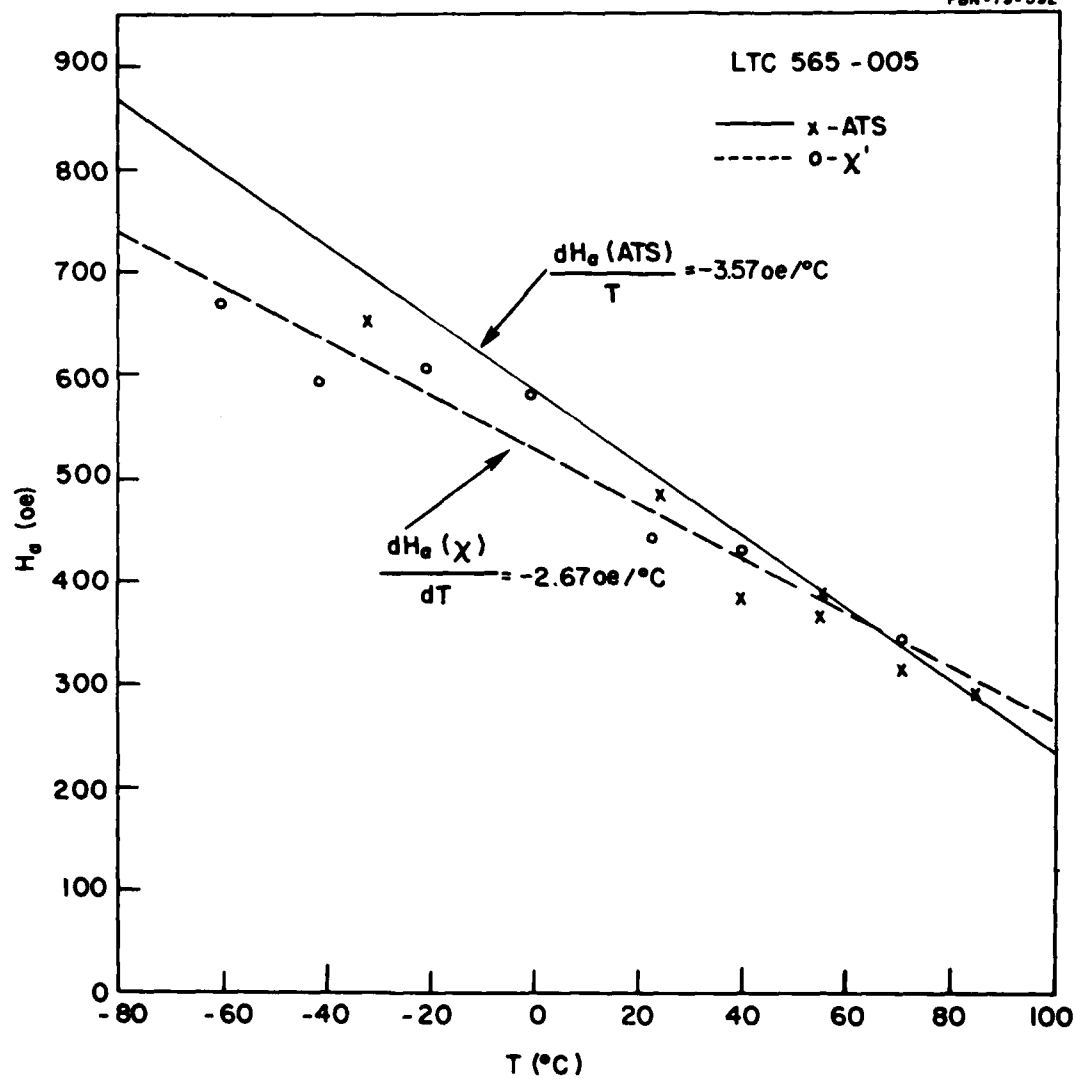


Figure 26. Anisotropy Field as a Function of Temperature.

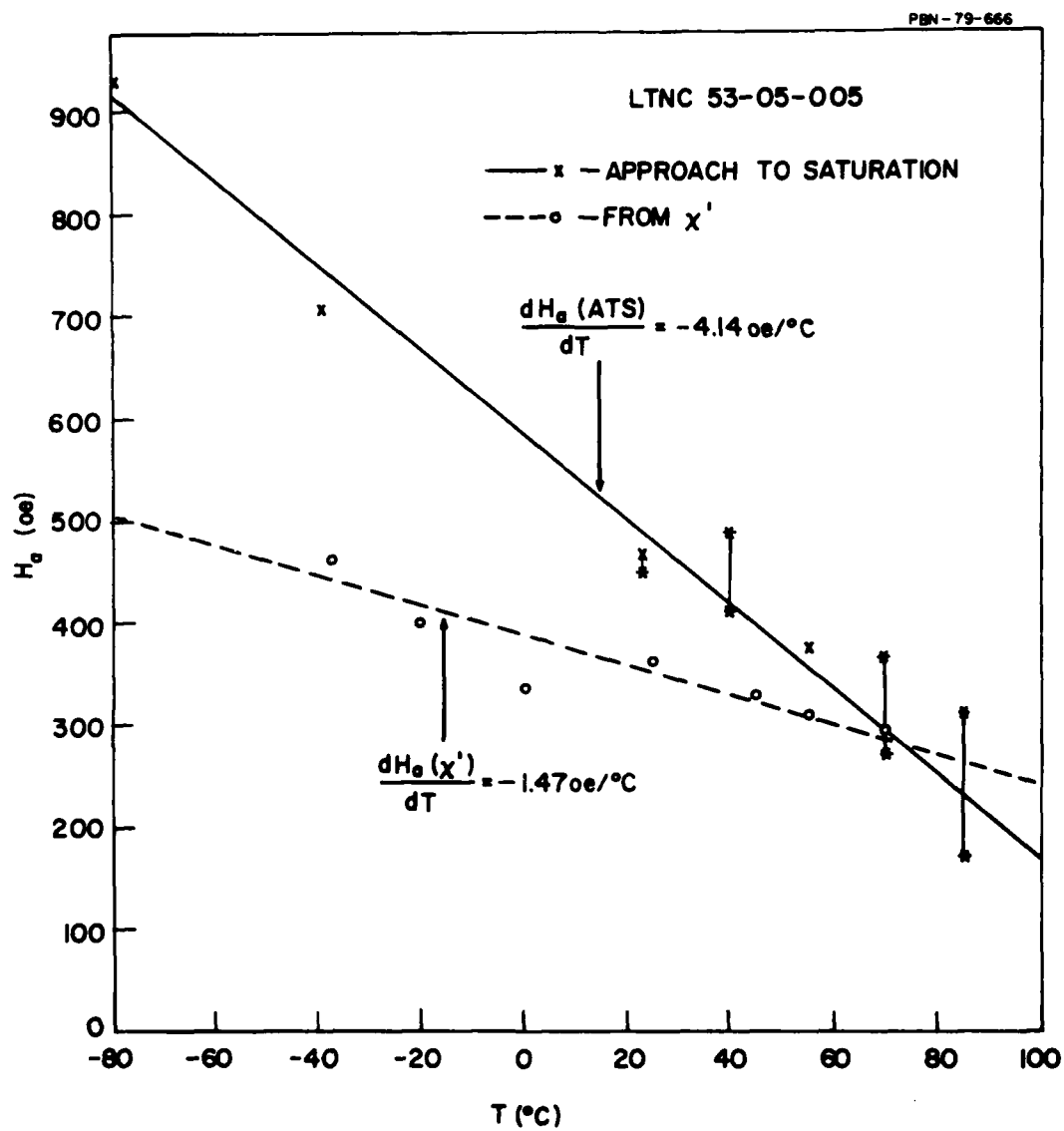


Figure 27. Anisotropy Field as a Function of Temperature.

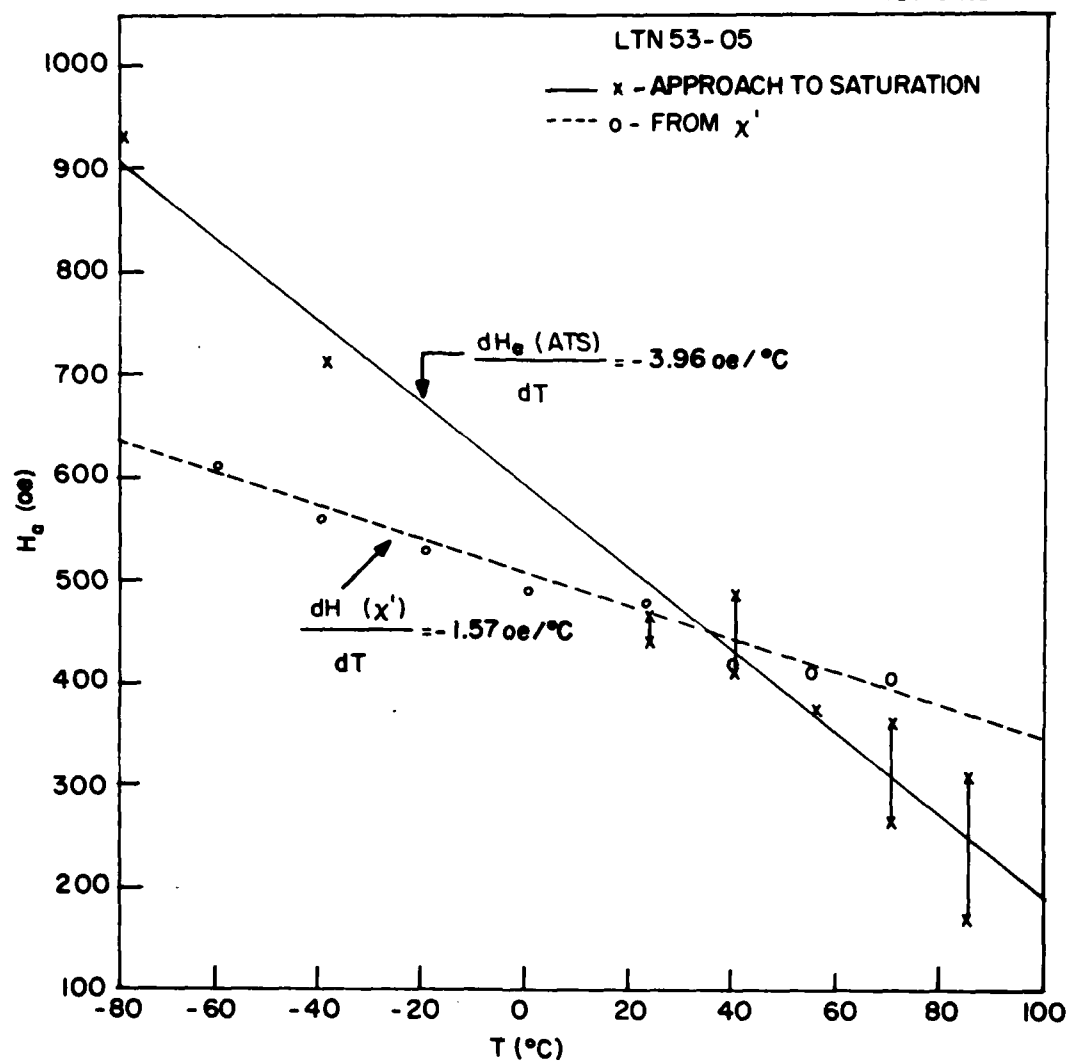


Figure 28. Anisotropy Field as a Function of Temperature.

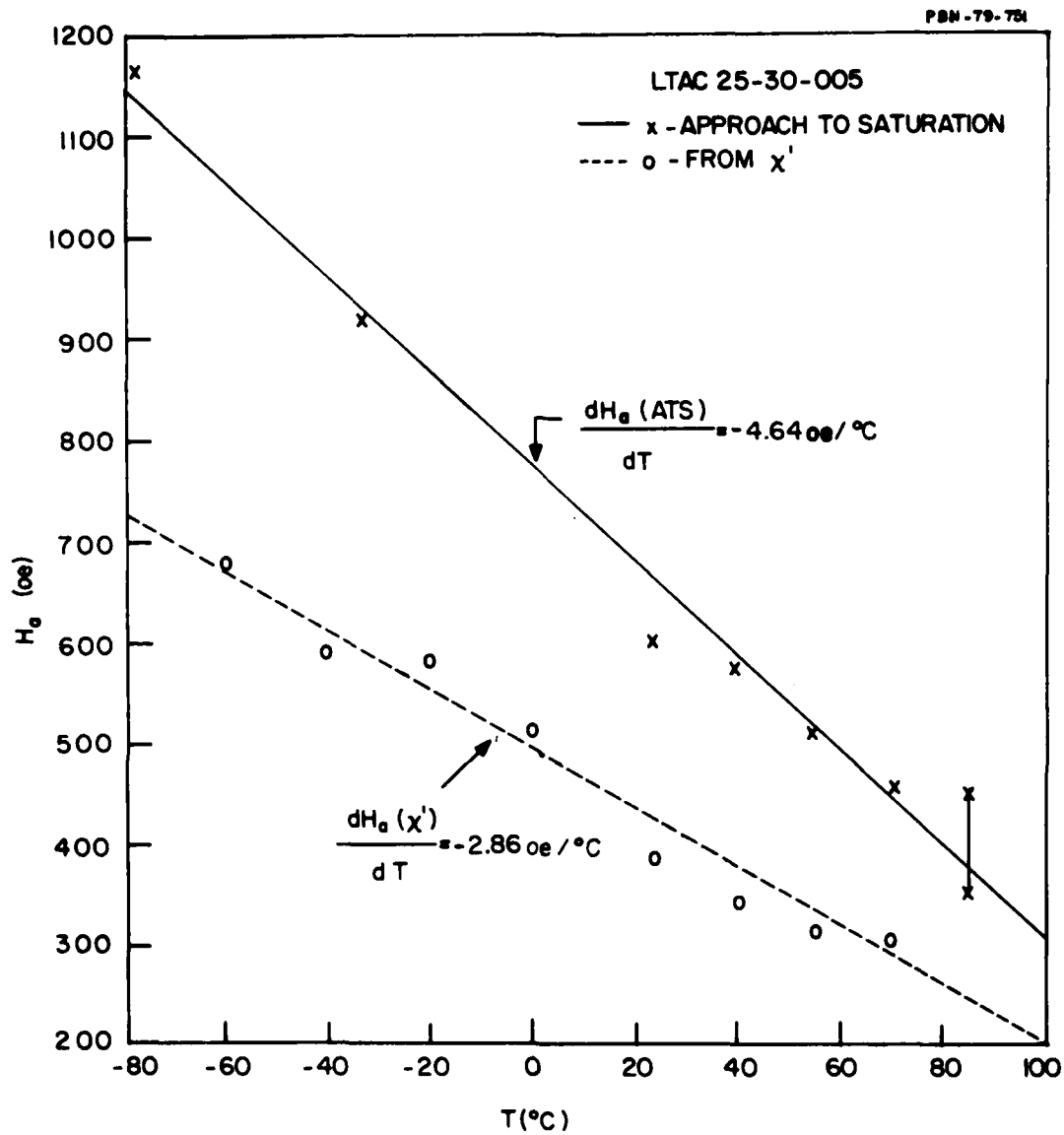


Figure 29. Anisotropy Field as a Function of Temperature.

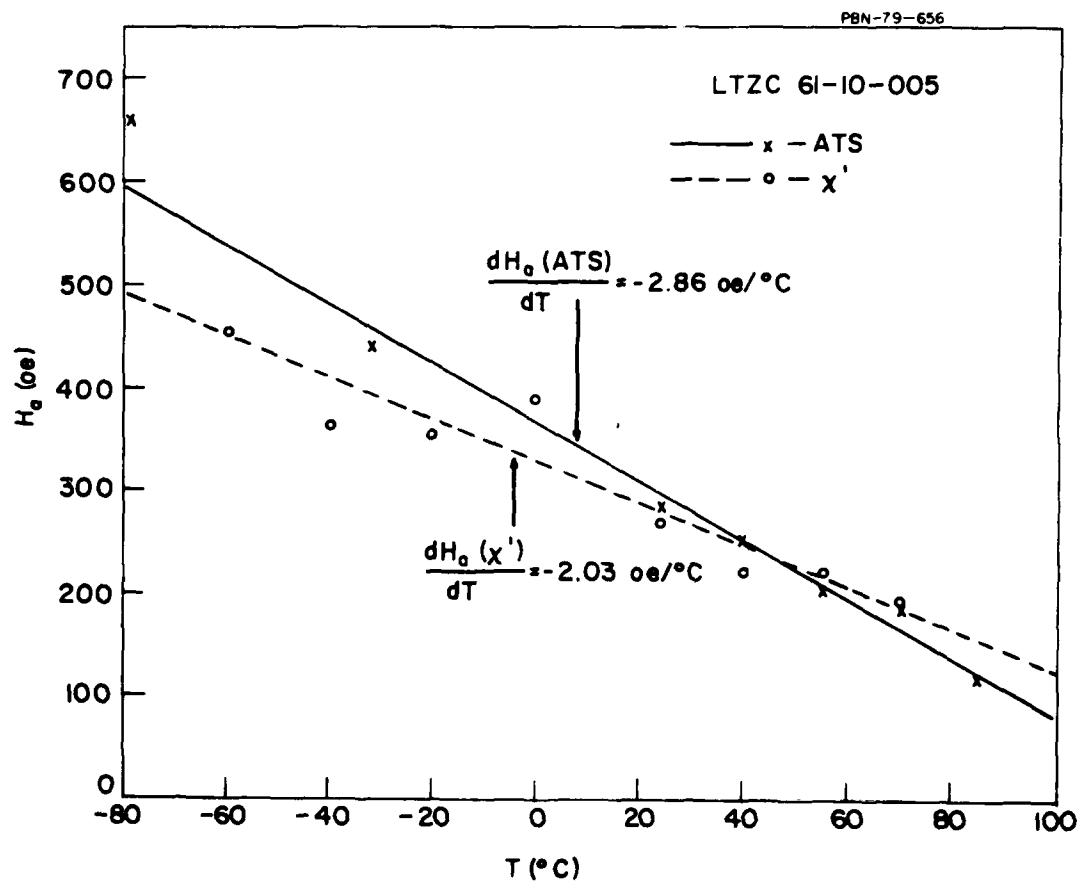


Figure 30. Anisotropy Field as a Function of Temperature.

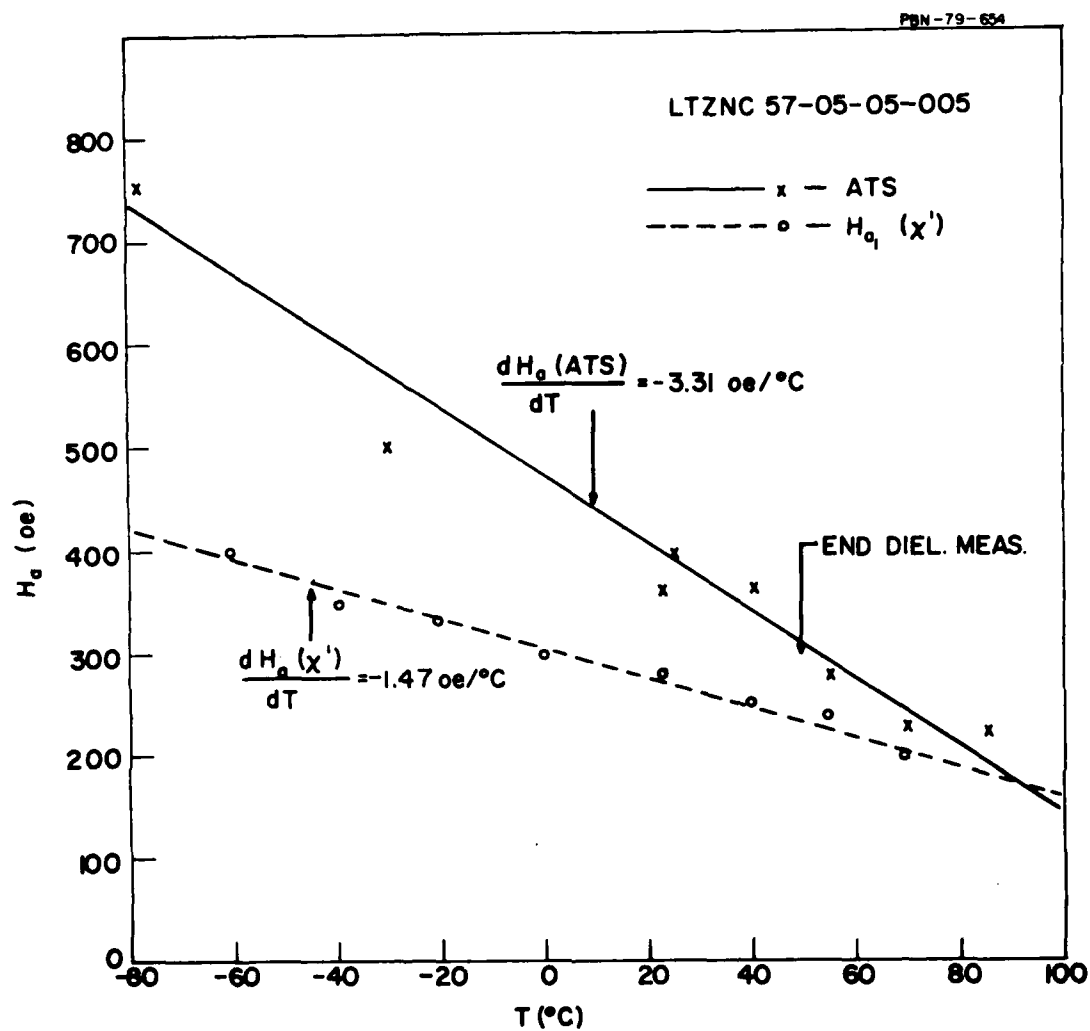


Figure 31. Anisotropy Field as a Function of Temperature.

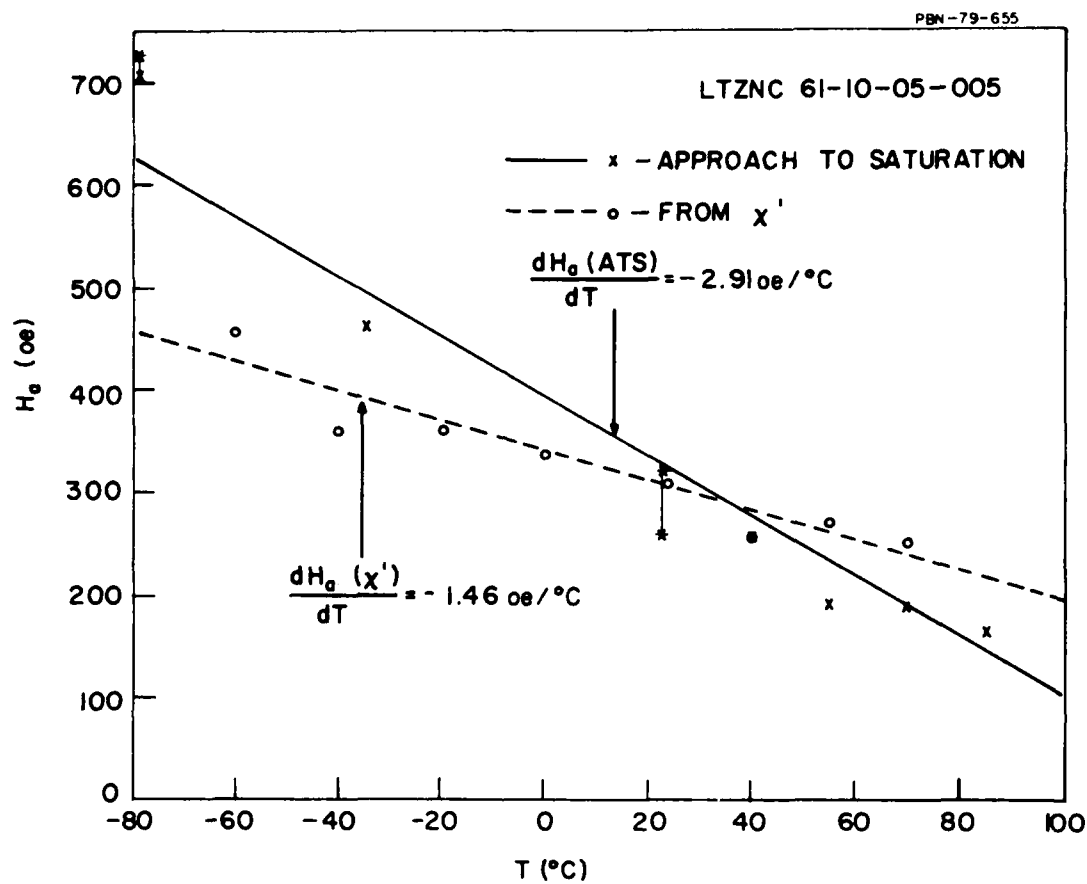


Figure 32. Anisotropy Field as a Function of Temperature.

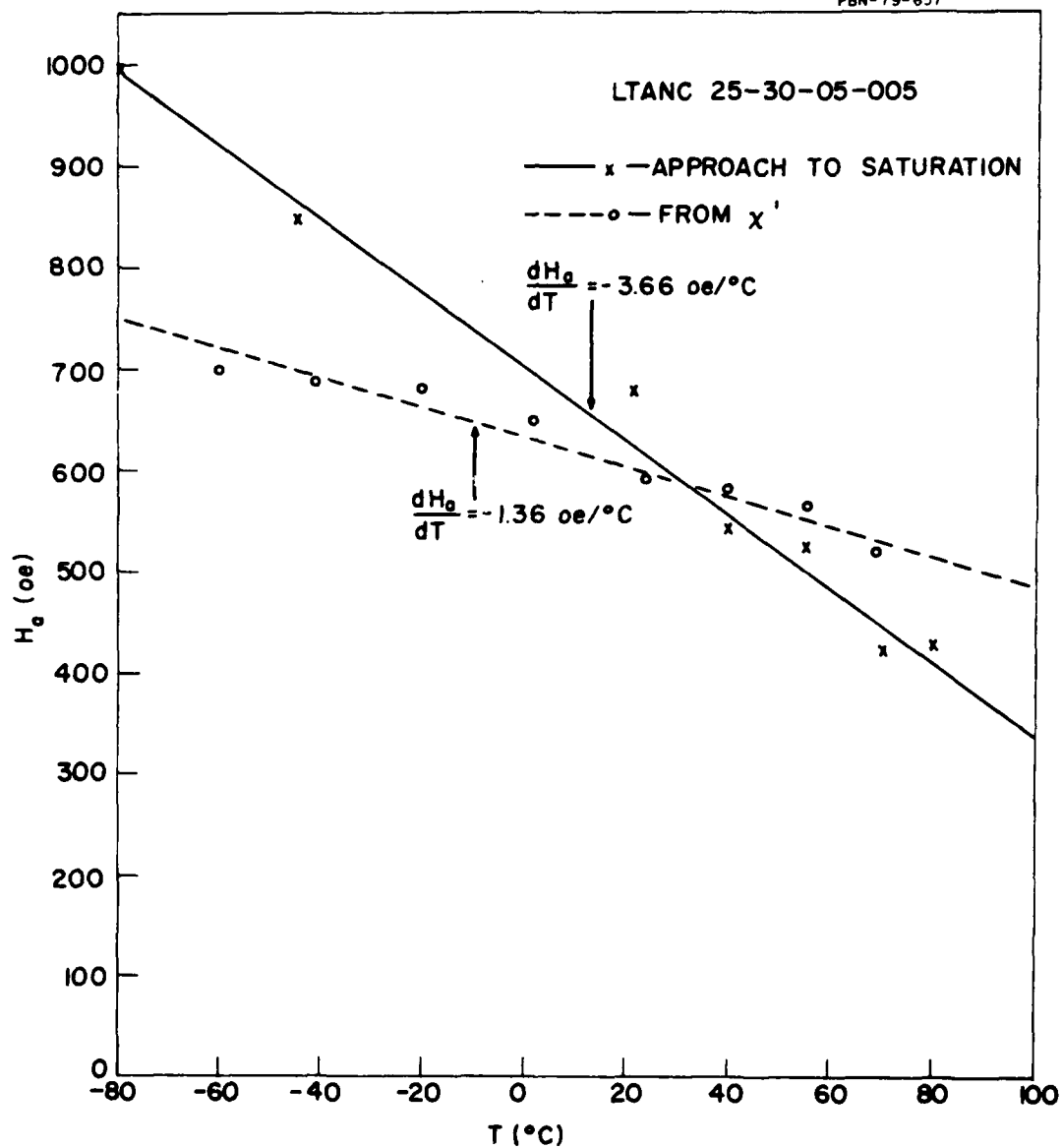


Figure 33. Anisotropy Field as a Function of Temperature.

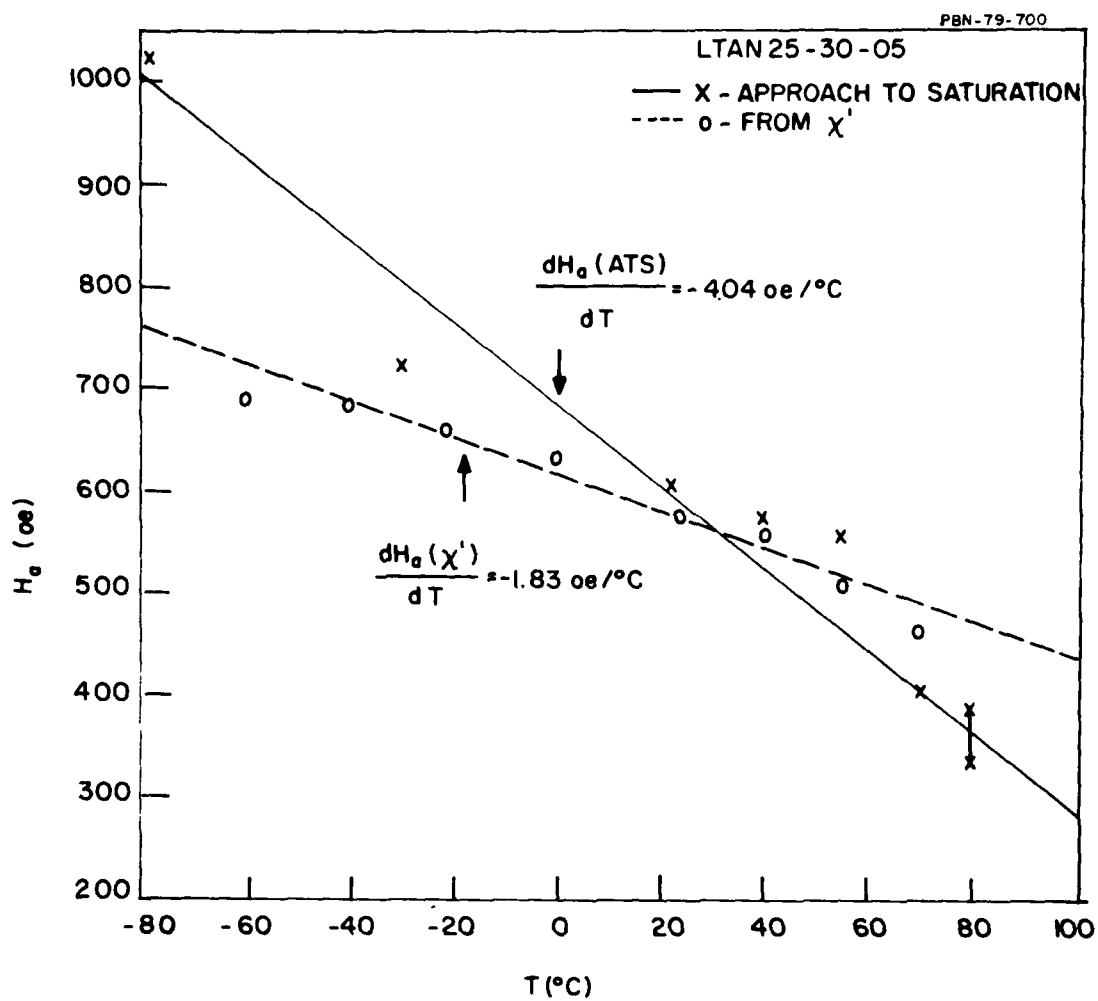


Figure 34. Anisotropy Field as a Function of Temperature.

experimental batches, a procedure for which a great deal of patience and special care was needed. The results of these measurements are contained in Figs. 35-48. The insertion phase in these plots is somewhat arbitrary, since it frequently included some connectors and matching sections. In some cases we arbitrarily took the unmagnetized state at 5.2 GHz and 22°C at 1000° of insertion phase. One must remember that it is the temperature variation that is important. The slope of the short phase shift state (the more temperature-sensitive state) was determined at -20°C and at +40°C.

Since some toroids gave less than 360° of phase shift at 80°C, either because of a thin phase shifting wall or because of low remanence on the particular waveguide toroid, all slopes were multiplied by $360^\circ/\Delta\phi(80^\circ\text{C})$. These values are summarized in Table 2.

Based on these results the LTZNC 61-10-05-005 composition was chosen to be used for the fabrication of 200 waveguide toroids. Its temperature coefficients were the lowest measured. Similar measurements made later in the program (Sec. 2.7) indicate even better temperature coefficients for the G10 large powder batch. Because of iron deficiency adjustments made in the preparation of the large batch powders, these materials are actually more like a LTZNC 63-10-05-005 small batch formulation. This is probably the reason for the further improvement of the temperature coefficient.

2.2 Toroid Processing and Raw Materials Quality Control

2.2.1 Raw materials

The basic oxide and carbonate raw materials used in the Research Division for experimental ferrite batches were obtained from Raytheon's Special Microwave Device Operations (SMDO). The same starting materials were used by SMDO in preparing the two production batches (30 kg) of the final 1200 gauss ferrite compositions.

The chemicals purchased by SMDO are reagent grade (> 99 percent purity) with lot analysis accompanying each container. Lithium, manganese, and cobalt

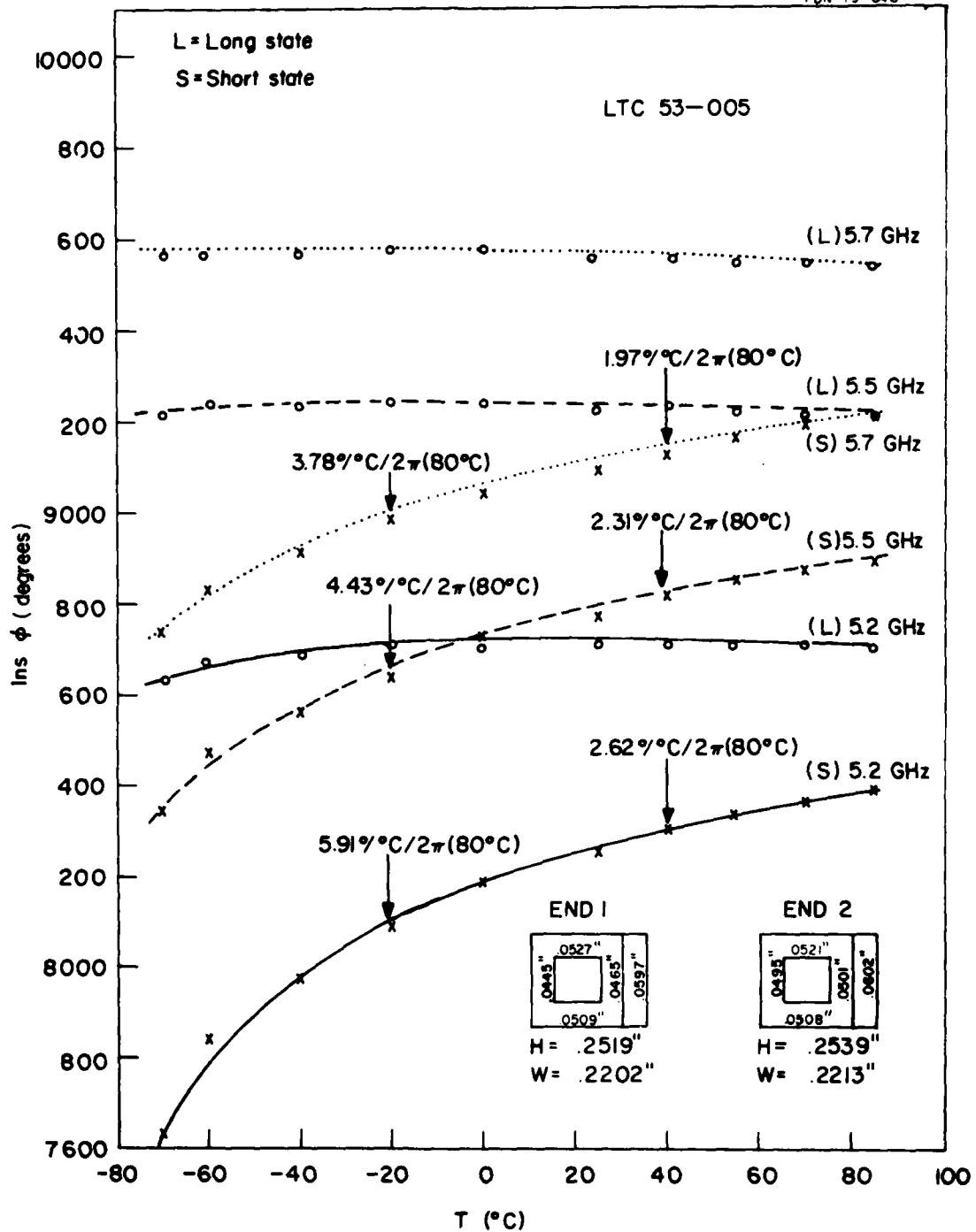


Figure 35. Saturated Insertion Phase as a Function of Temperature.

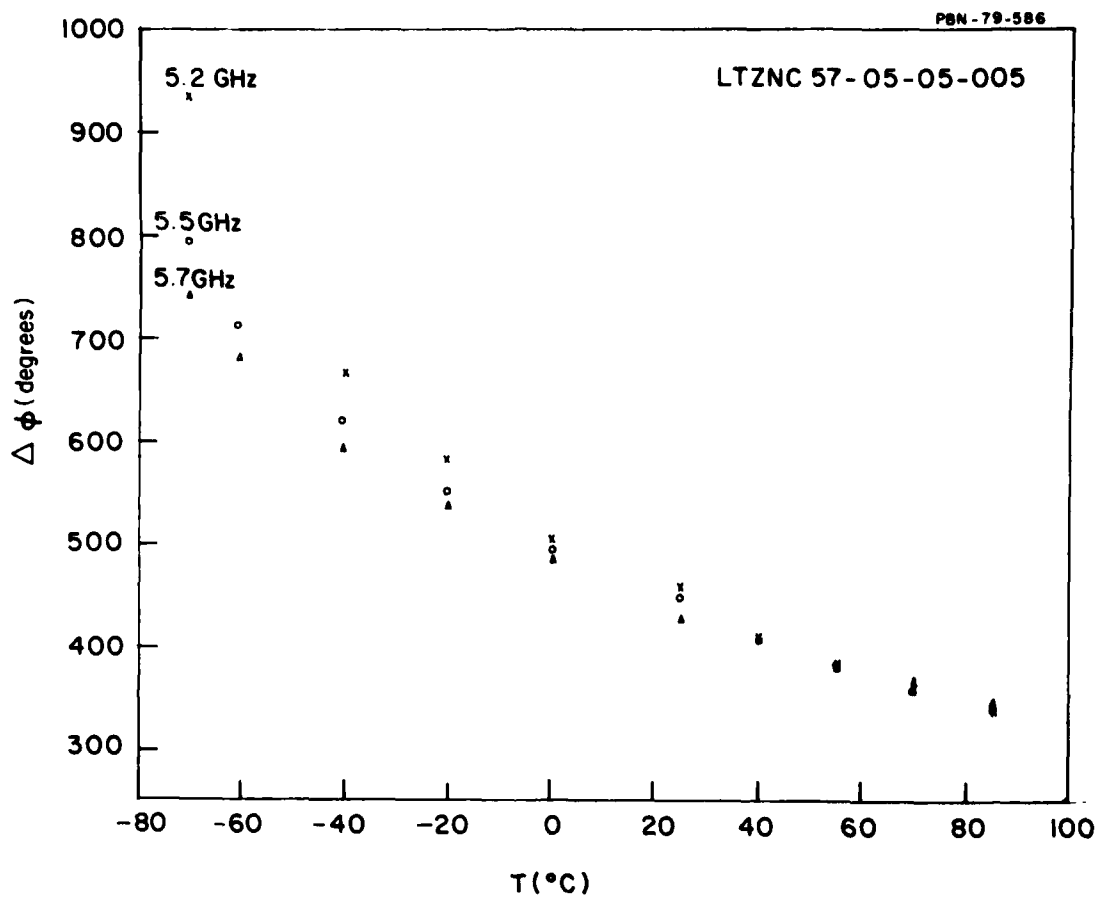


Figure 36. Saturated Differential Phase as a Function of Temperature.

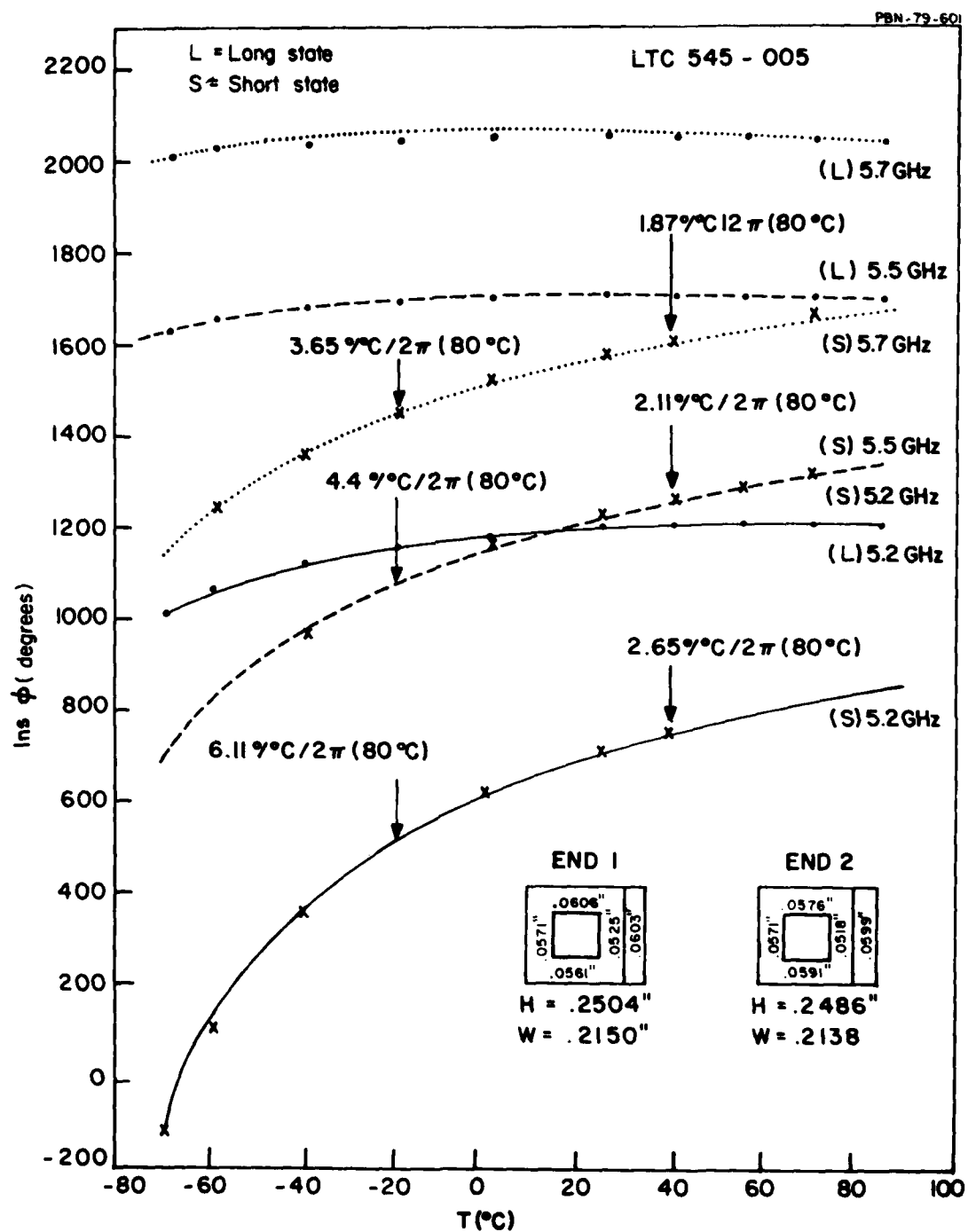


Figure 37. Saturated Insertion Phase as a Function of Temperature.

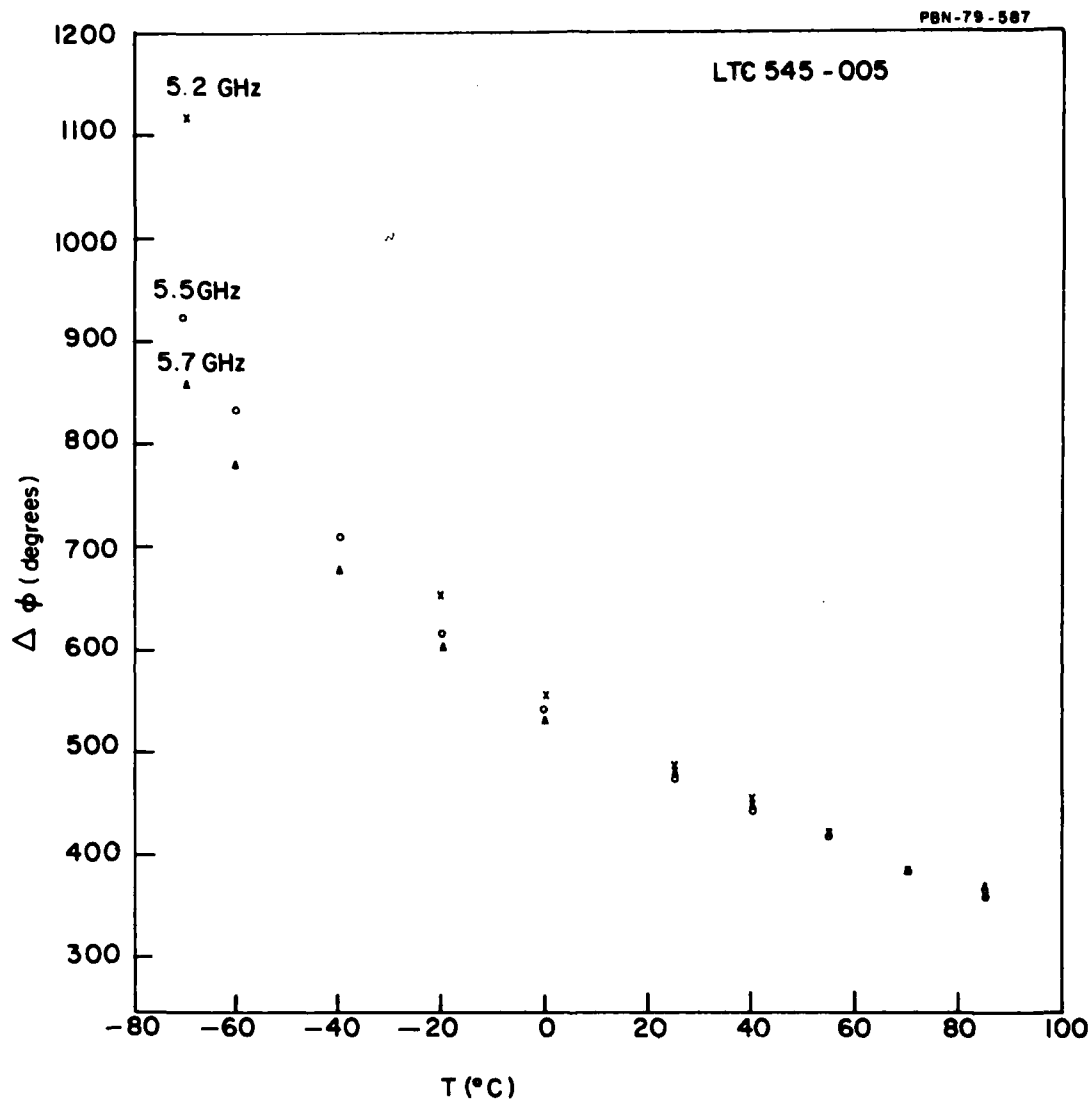


Figure 38. Saturated Differential Phase as a Function of Temperature.

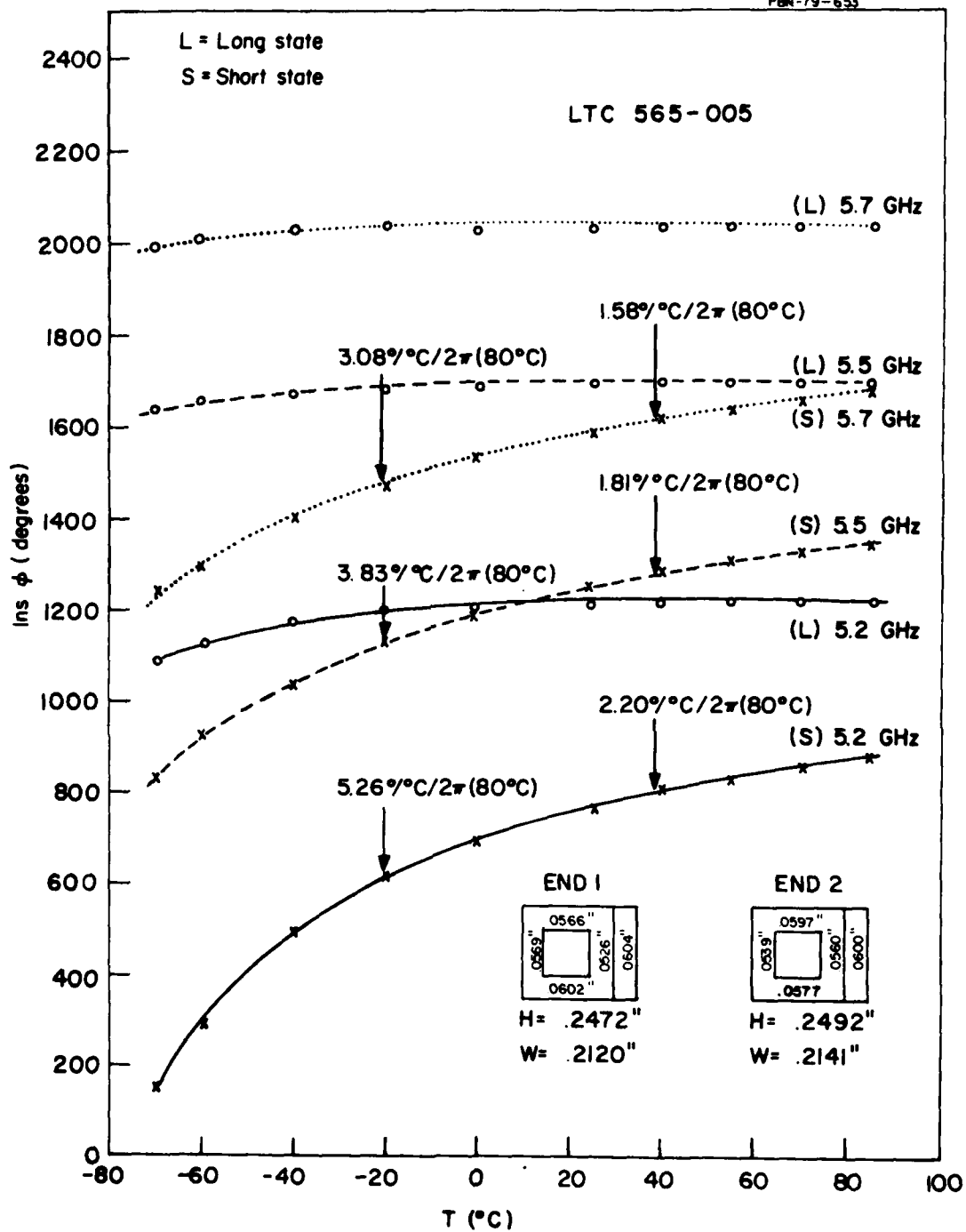


Figure 39. Saturated Insertion Phase as a Function of Temperature.

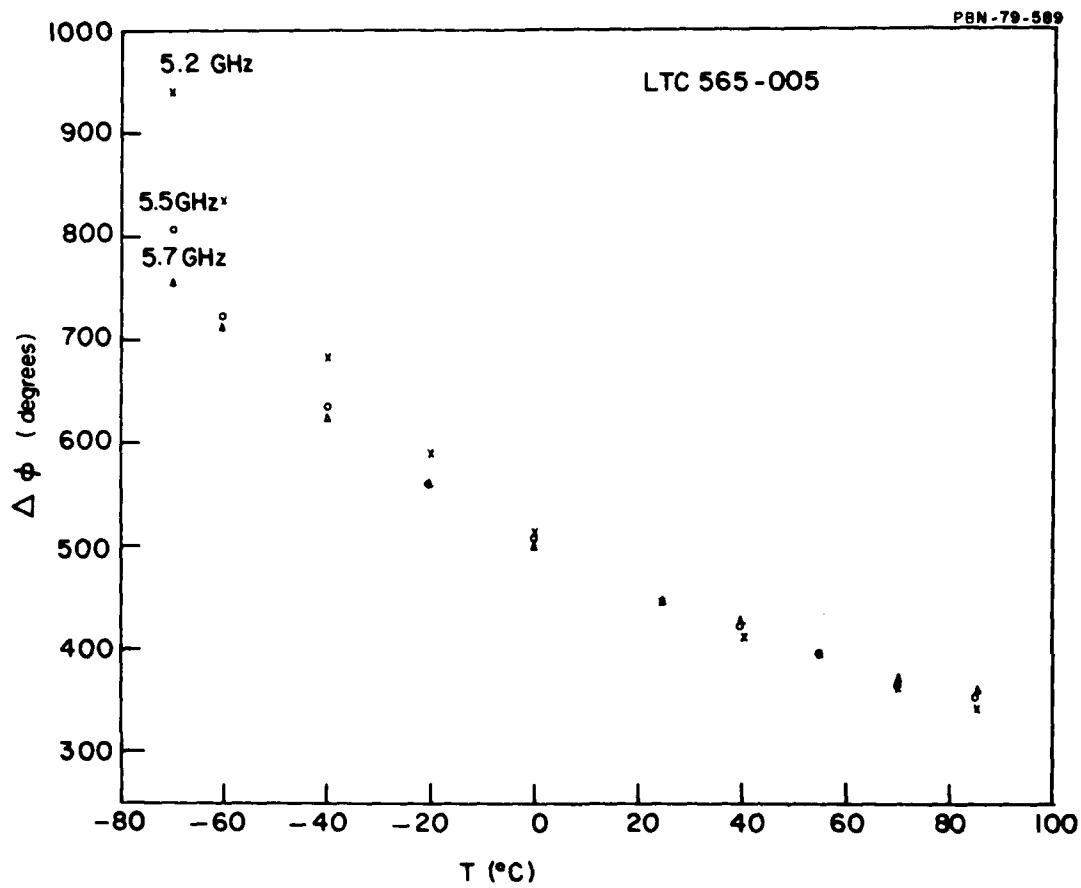


Figure 40. Saturated Differential Phase as a Function of Temperature.

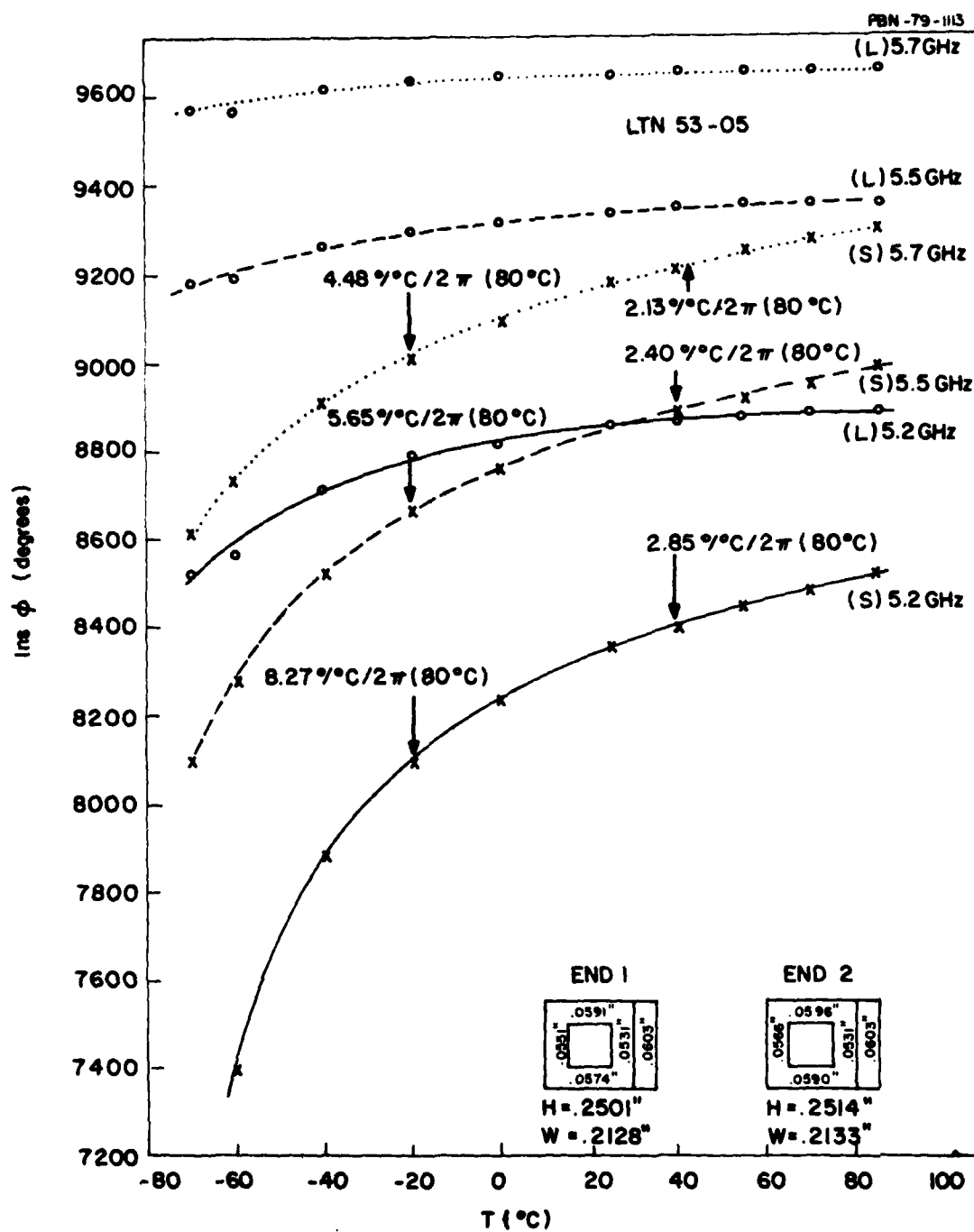


Figure 41. Saturated Insertion Phase as a Function of Temperature.

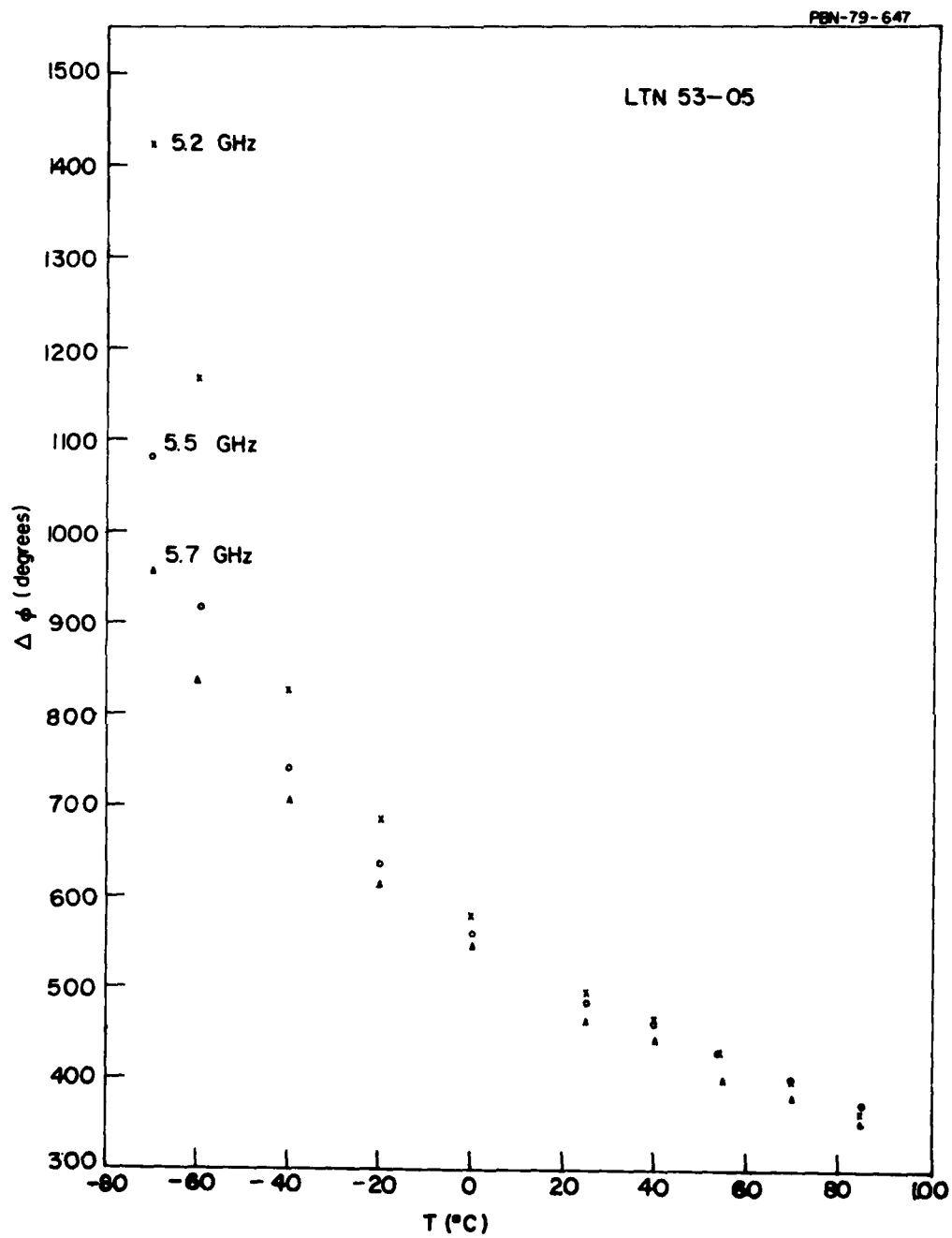


Figure 42. Saturated Differential Phase as a Function of Temperature.

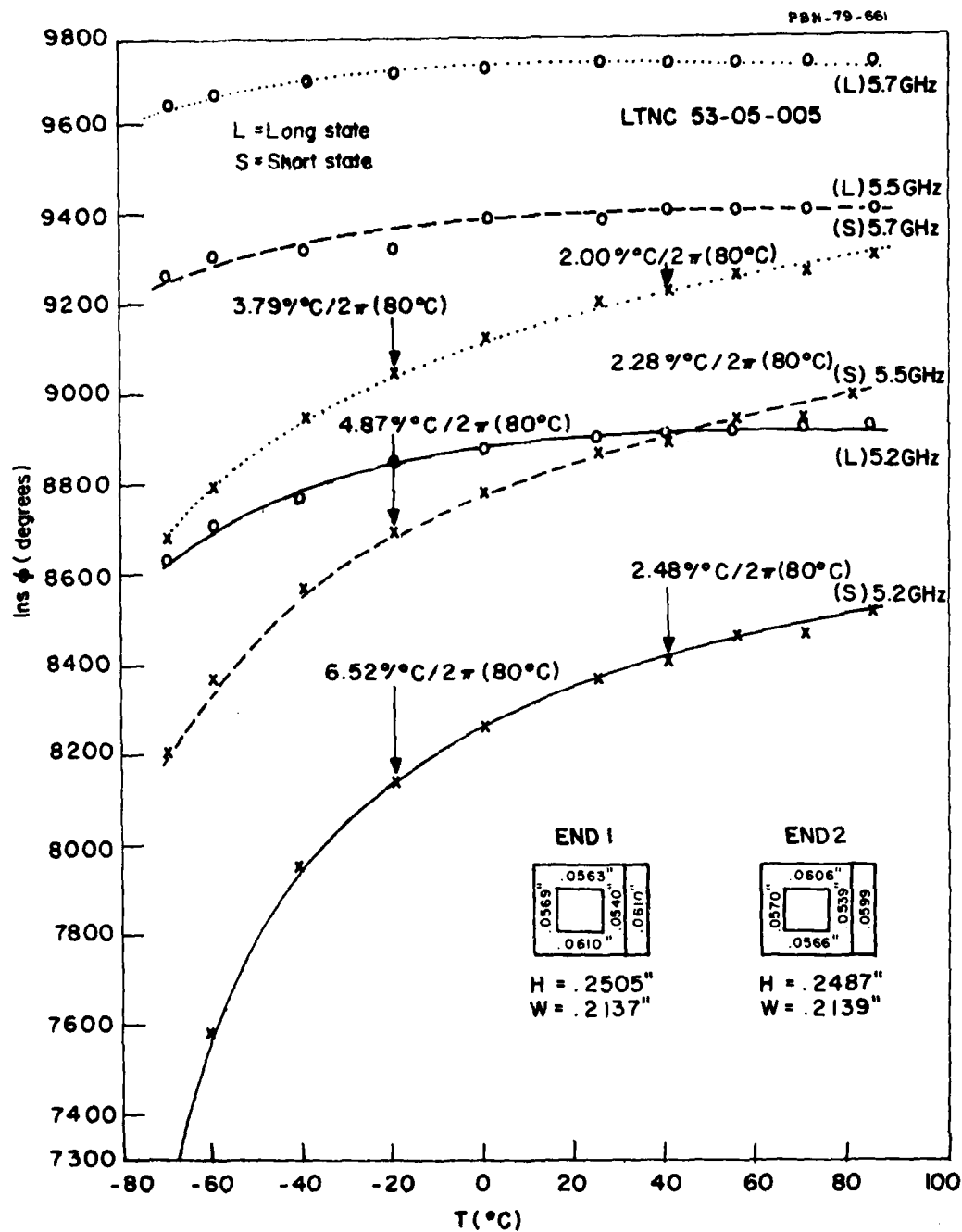


Figure 43. Saturated Insertion Phase as a Function of Temperature.

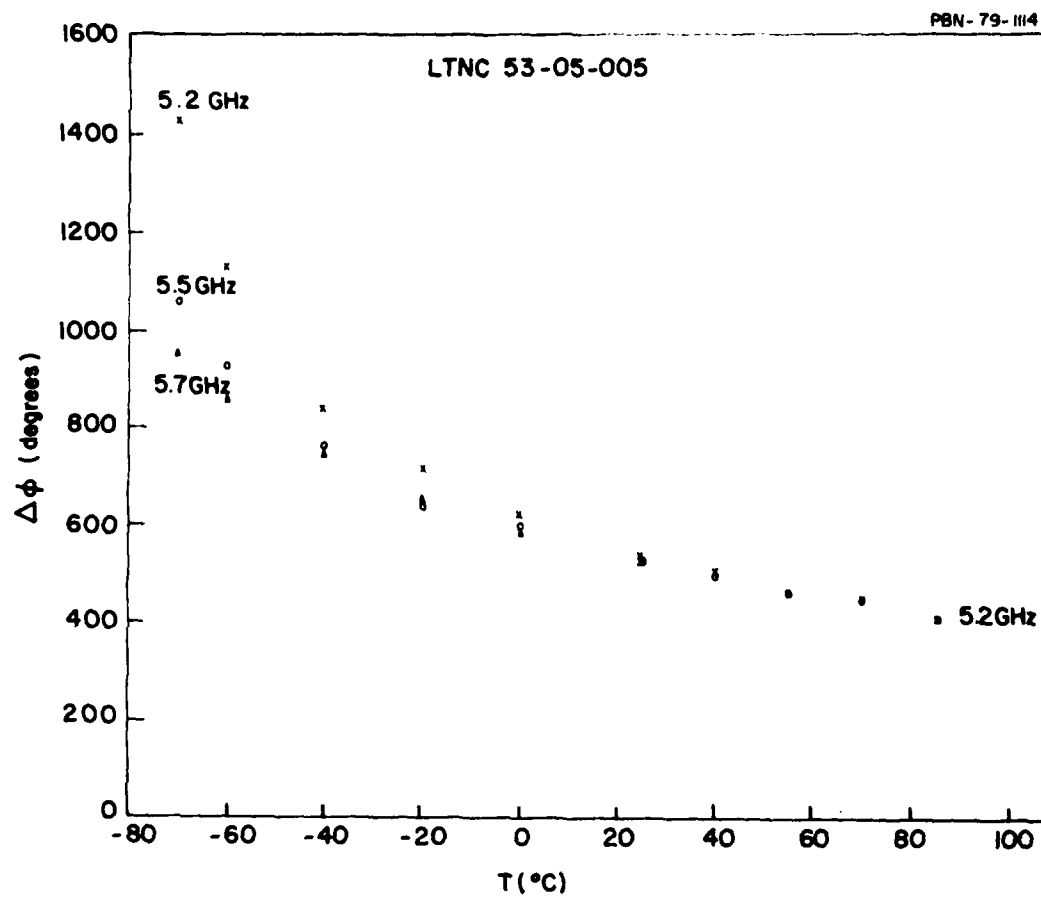


Figure 44. Saturated Differential Phase as a Function of Temperature.

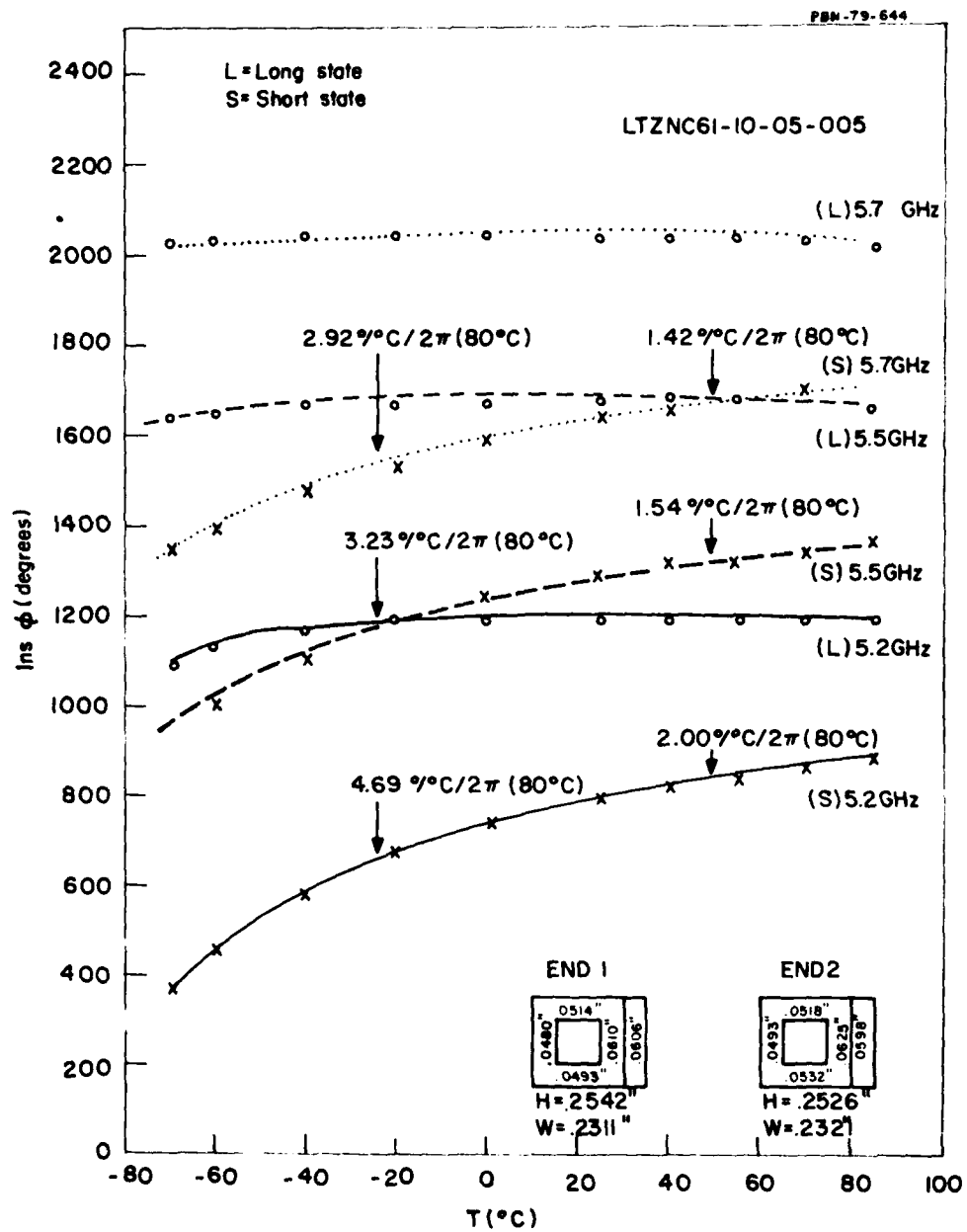


Figure 45. Saturated Insertion Phase as a Function of Temperature.

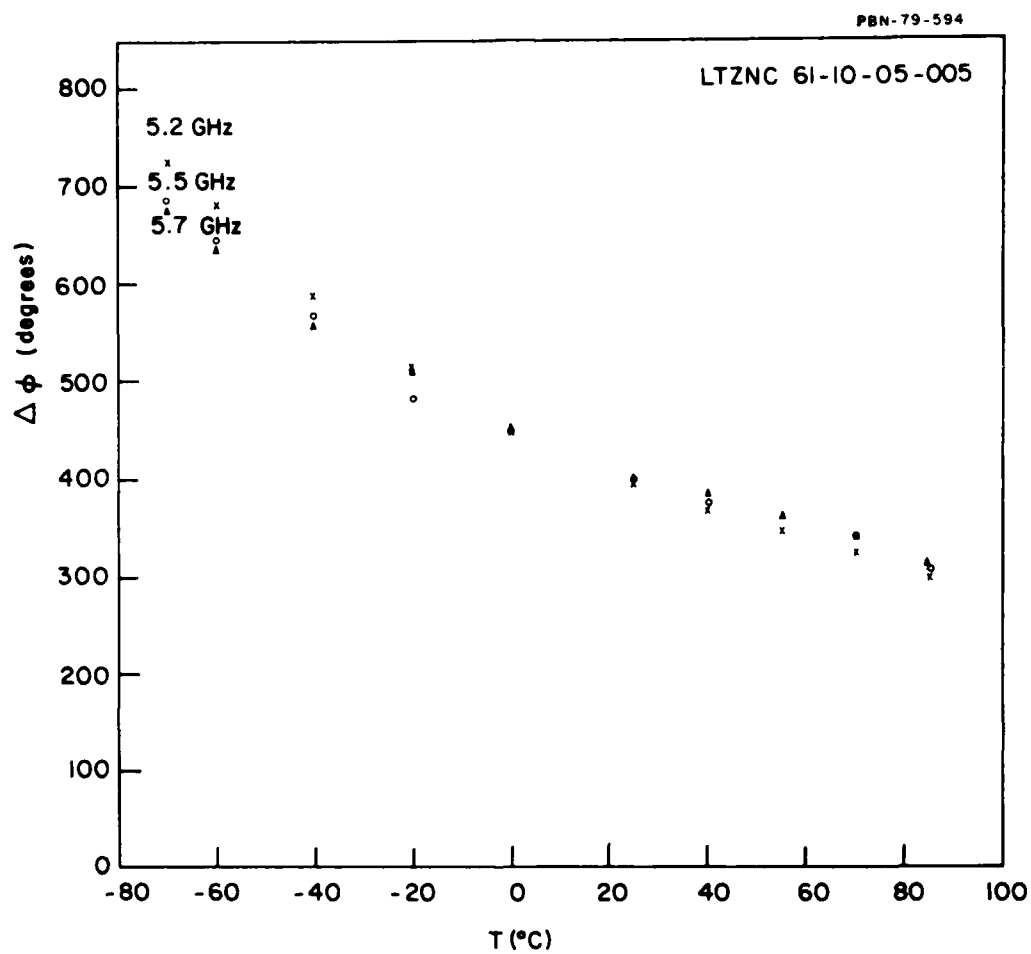


Figure 46. Saturated Differential Phase as a Function of Temperature.

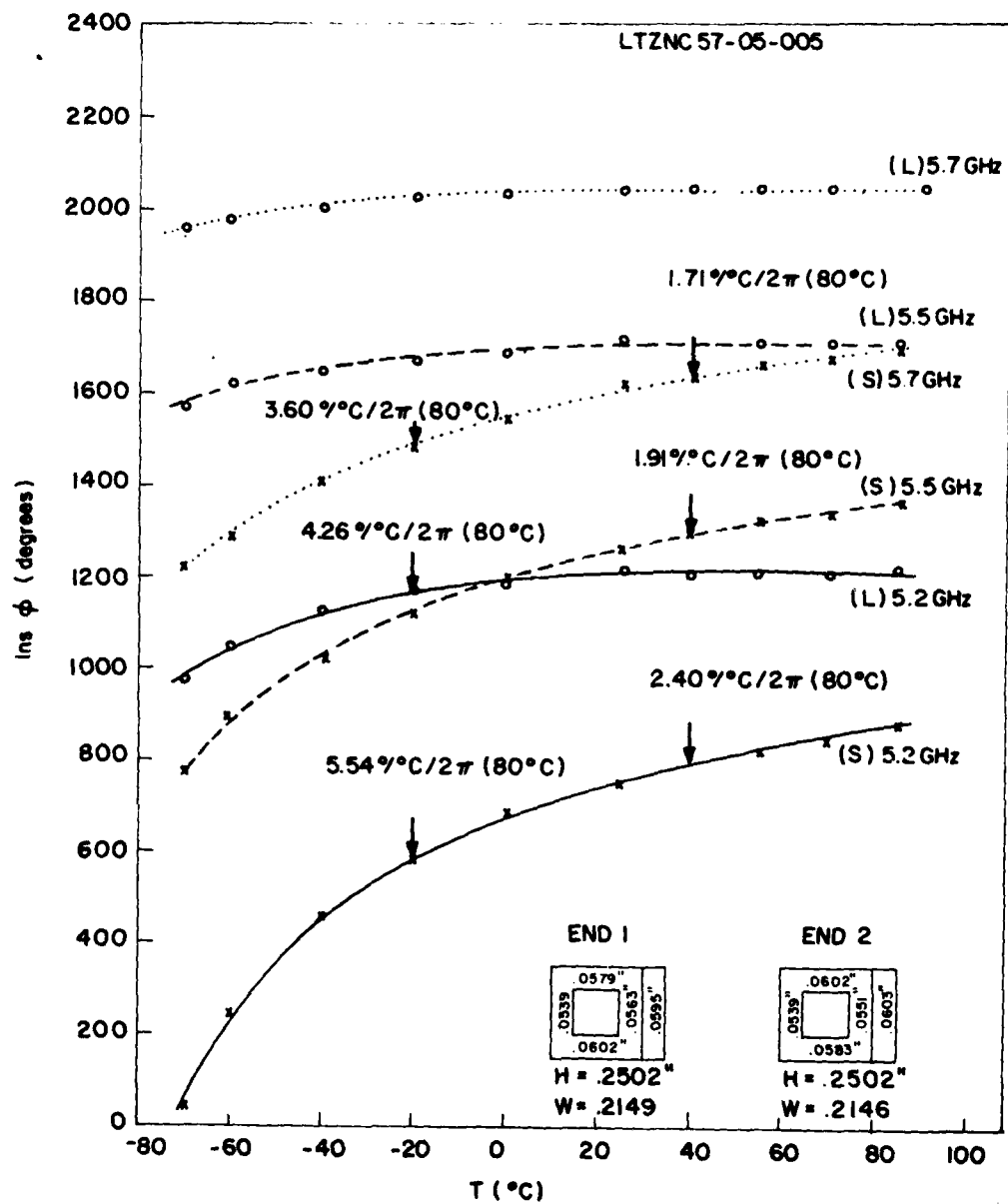


Figure 47. Saturated Insertion Phase as a Function of Temperature.

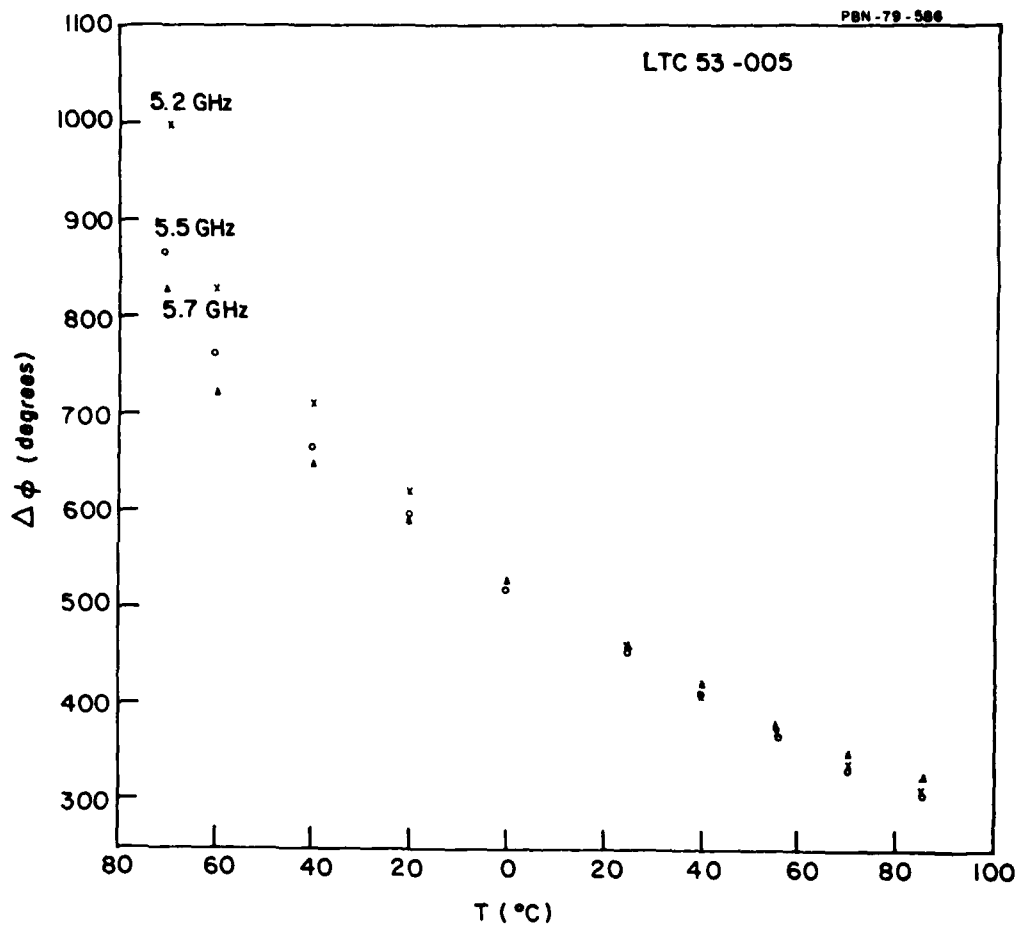


Figure 48. Saturated Differential Phase as a Function of Temperature.

TABLE 2

TEMPERATURE DEPENDENCE OF INSERTION PHASE (SHORT STATE)

(degree/degree centigrade/360° $\Delta\phi$ at 80°C)

<u>Material</u>	<u>Temp</u>	<u>5.2 GHz</u>	<u>5.5 GHz</u>	<u>5.7 GHz</u>
LTC 53-005	-20°	5.91	4.43	3.78
	40°	2.62	2.31	1.97
LTC 545-005	-20°	6.11	4.45	3.65
	40°	2.65	2.11	1.87
LTC 565-005	-20°	5.26	3.83	3.08
	40°	2.20	1.81	1.58
LTN 53-05	-20°	8.27	5.65	4.48
	40°	2.85	2.40	2.13
LTNC 53-05-005	-20°	6.52	4.87	3.79
	40°	2.48	2.28	2.00
LTZNC 57-05-05-005	-20°	5.54	4.26	3.60
	40°	2.40	1.91	1.71
LTZNC 61-10-05-005	-20°	4.69	3.23	2.92
	40°	2.00	1.54	1.42

are purchased as carbonates with a total metal ion impurity of > 0.5 percent. Aluminum was obtained as $\text{Al}(\text{OH})_3$ from Baker Chemical Company and Aluminum Company of America. Total metallic impurities in this case were > 0.05 percent, well under the rejection level, but the water content was found to be variable and required an assay to provide the necessary data on stoichiometry. Titanium and iron are purchased as the reagent grade oxides TiO_2 and $\alpha\text{Fe}_2\text{O}_3$. Zinc was also used in the oxide (ZnO) form. All had reported impurities of > 0.5 percent by weight.

The raw materials were further checked at Research by weight loss after heating to $800 - 1000^\circ\text{C}$, excepting Li_2CO_3 , which could not be tested this way (Li_2O is volatile at elevated temperatures). The firing left the oxides in their stable form and converted the carbonates CoCO_3 and MnCO_3 to the oxides Co_3O_4 and Mn_2O_3 . From the change in weight on firing we then determined volatile content, i.e., H_2O , CO_2 , organics if any, and made corrections in the chemical assay. Loss on ignition for $\alpha\text{Fe}_2\text{O}_3$ was 0.2 percent; for TiO_2 , 0.2 percent; for MnCO_3 , 2.4 percent; and for Li_2CO_3 a 100°C desiccation indicated a moisture content of 0.1 percent.

2.2.2 Powder processing

After determining the proper chemical formulation (Sec. 2.1), the raw materials were weighed on top-loading balances to ± 0.005 g and transferred to steel jar mills. Electronic grade methanol was added to make a slurry of the proper consistency for the first milling. The mixture was then milled with steel balls for 16 hours to give a homogeneous product. The slurry was dried in stainless steel pans and screened in preparation for calcining. A flow chart for the powder processing with these and subsequent steps is shown in Fig. 49.

The calcining step reacts the mixture of raw materials at elevated temperature to produce a single phase spinel. During the step the iron picked up during initial milling is oxidized and incorporated into the spinel matrix, allowance having been made for its addition. The only direct indicator of the effectiveness of the calcining step is X-ray diffraction of the high angle spinel

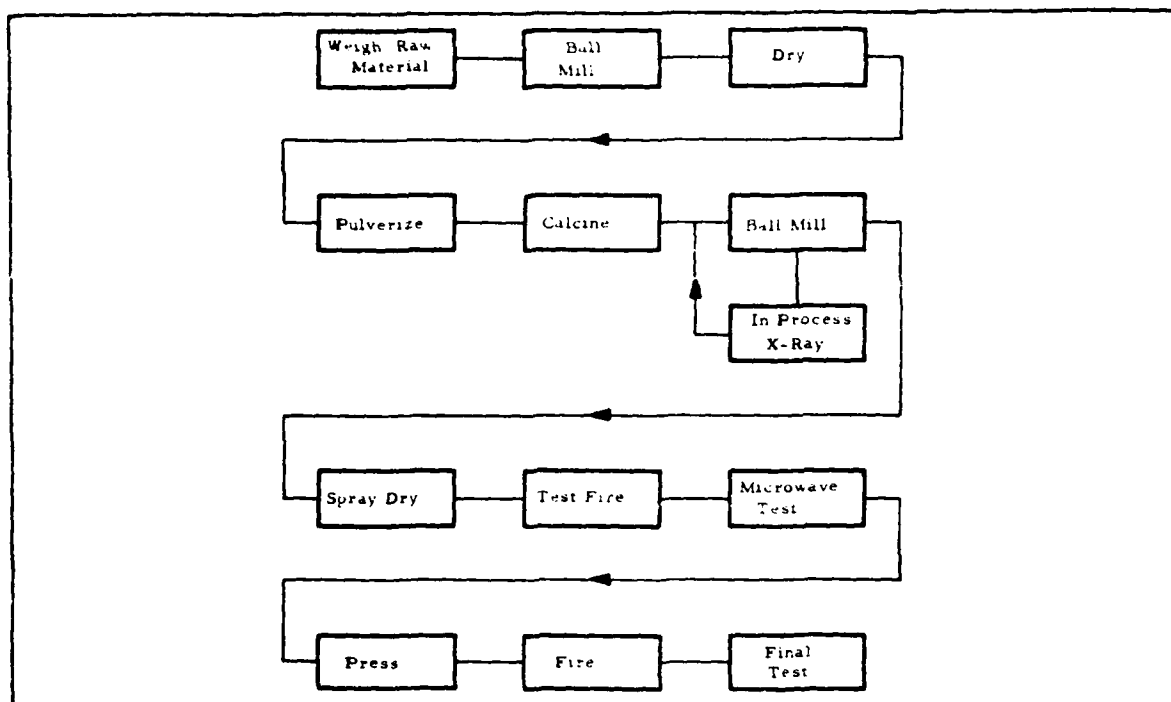


Figure 49. Flow Chart for Production of Microwave Ferrite Material.

peaks. A normal diffraction scan is not sensitive enough to indicate small differences in the degree of product homogeneity, but lineshape analysis can provide this information. Several investigators have shown that the formation of Li-Ti ferrite compositions does not occur as a single-step solid state reaction. The first product is pure Li-ferrite, which then reacts with remaining Mn, Ti, Zn, and other more slowly diffusing components to produce the final Li-Ti-Zn ferrite solid solution. Since there is a variation in lattice parameter with composition, one can use the broadening of high angle diffraction peaks to indicate the presence of a range of spinel compositions which would be characteristic of an incompletely reacted material. With extended calcining time or high temperature, the broad peak gives way to the sharply defined diffraction peak of a well-crystallized homogeneous material.

After calcining, the ferrite powder must be reground to give a fine particle size ($> 1 \mu\text{m}$) suitable for sintering. The second milling again uses a liquid medium, although this time either methanol or water is suitable, since we no longer have water soluble components as in the first milling. After milling and the addition of any binder materials, the slurry is again dried and screened preparatory to pressing and final firing.

Several additional tests are made at this point. One of these is analysis by X-ray fluorescence to establish iron content and to check on the proper concentration of other minor components. Fluorescence analysis is done on a routine basis as a check on the weighed-in concentrations, to determine additional iron pickup, and to check on cation content in materials made at SMDO, which has different weighing and powder processing equipment.

2.2.3 Toroid forming

Two different manufacturing processes have been used in the microwave industry to form garnet toroids for dielectric-loaded phase shifters. One uses a steel die to form the part around a center pin. A double-acting press is usually needed to give the uniformity and shrinkage control required on all four walls. A second method is to isostatically press the part around a steel

center pin using a flexible rubber bag. In both of these forming processes a free-flowing spray-dried powder must be used to allow even filling of the mold.

For die pressing, a double-acting press is a minimum requirement for forming a toroid. Even with a high content of organic lubricants in the ferrite powder, a unidirectional press could not be expected to press uniformly against the toroid side walls because of the large aspect ratio. (length to thickness parallel to the pressing direction). The situation is much improved with double-acting machinery, but even here one must realize that the die walls cannot produce uniform compaction with a fluctuating powder density unless there is enough lubricant to allow the sideways displacement of powders from adjacent regions. Even the best free-flowing powders will always give some local variation in packing density. The use of steel dies will therefore require higher concentration of lubricating additives. It has been our experience that organic additives always lead to some degradation in final density no matter how careful the burnout or how fine-grained and well-dispersed the additive. The isostatic forming process therefore has the advantage of allowing the use of a minimum of binder and lubricants in the ferrite powder.

The toroidal samples are formed at 15,000 psi around a hardened steel pin. During the contract period we had considerable discussion with our vendor about whether he could provide steel pins with the 0.123×0.157 inch cross sections which were straight to within 0.001 inch or better along the full 7.5 inch length. Straightness is important to allow dismounting the pressed shape without cracking the toroid and because an initial bow, even if successfully dismounted, might favor a continued distortion in shape during firing. It is not a simple task to press and fire a ceramic to the degree of straightness specified for latching-type phase shifters. The aspect ratio of sample length (5 inches) to the straightness required for wall uniformity (± 0.002 inch) is about 1000:1. Since it is not practical or cost effective to machine interior surfaces of the toroid and since the exterior surface machining automatically produces wall thickness variations if the center hole is not kept straight, it is obviously very important to maintain control over this property throughout the manufacturing process.

One way of controlling this problem is to maintain complete records of every step in processing and firing which could contribute to shape distortion. One can then evaluate the effect of corrective actions throughout the entire process. A first step in this direction is the development of a test procedure for rapid and nondestructive measurement of the property we wish to control, i.e., toroid wall thickness. A quantitative method using ultrasonic thickness gauge has been developed. Extensive data were obtained and recorded manually on nearly all of the phase shifters produced under this contract. Forty-four individual measurements were made on each toroid, eleven per wall, at half-inch intervals. The results were used to calculate hysteresis properties and to assess mean values of wall thickness and their standard deviation on all of the machined toroids. The data are presented in Sec. 2.7. The other aspect of this problem, that of keeping detailed records of processing and firing, will be covered in this section.

One of the initial checks on processing conditions was measurements of pin straightness for isostatic pressing. Table 3 shows the results of micrometer gauge measurements on the steel pins after about 5 to 10 forming operations. The bowed upwards surfaces in the two orthogonal directions were found and their departure from flatness was recorded at 0.5 inch intervals. A previous check on cross-sectional dimensions had found them constant to within ± 0.0002 inch, so the recorded variations in height are due entirely to shape distortion. In the table the AC values of bowing are perpendicular to the larger cross-sectional dimension, the stronger pin direction, and BD represents bowing observed in the weaker direction. As shown, the bowing in the two orthogonal directions is about 1.5 mils (0.0015 inch) in pin No. 10, about 4 mils in the weaker cross-sectional direction for pin No. 11, and about 1 mil or less for pins Nos. 13, 16 and 17.

The information on the pin used and the relation of the formed toroid to the die pin and to the setter plate in the kiln (i.e., which surface was up and which oriented downward) was also recorded for each toroid. Finally, the location of each toroid in the kiln and all of the other particulars about the firing were also noted so that we could check back at a later date and determine

TABLE 3

DEPARTURE FROM STRAIGHTNESS IN MILS FOR THE STEEL PINS
USED IN FORMING OF Li-Ti-FERRITE TOROIDS

Pin No.	Distance in Inches from Base of the Pin														
	0	0.5	1	1.5	2	2.5	3	3.5	4	4.5	5	5.5	6	6.5	7
10 AC	0	0.1	0.6	0.8	0.9	1.0	1.0	1.2	1.3	1.5	1.6	1.6	1.5	1.2	0.7
10 BD	0	0.2	0.3	0.3	0.4	0.6	0.8	1.0	1.3	1.4	1.4	1.2	1.1	0.9	0.6
11 AC	0	0.6	1.2	1.7	2.0	2.0	1.9	1.8	1.5	1.4	1.2	1.0	0.9	0.6	0.4
11 BD	0	0.5	1.0	1.6	2.4	3.2	3.7	4.0	4.1	4.1	3.9	3.5	2.9	2.1	1.2
13 AC	0	0	0	0.2	0.3	0.4	0.5	0.3	0	0.1	0.4	0.4	0.3	0.2	0.1
13 BD	0	1.0	1.4	1.4	1.3	1.4	1.3	1.2	1.1	1.2	1.3	1.3	1.3	1.2	0.8
16 AC	0	-0.2	-0.2	+0.1	0	+0.1	0.3	0.4	0.35	0.35	0.65	0.10	0.2	0.2	0.1
16 BD	0	0.3	0.2	0.2	0.2	0.1	0.25	0.5	0.70	0.65	0.6	0.65	0.90	0.6	0.4
17 AC	0	0.25	0.6	0.6	0.5	0.3	0.3	0.5	0.5	0.65	0.55	0.4	0.4	0.2	0.15
17 BD	0	0.2	0	0.15	0.6	0.8	1.2	1.55	1.2	1.1	0.85	0.4	0.4	0.4	0.3

whether any one factor or combination of factors was primarily responsible for the bowing. All of these data are summarized along with the hysteresis loop properties in the master chart in Sec. 2.7.

2.3 Toroid Property Verification

2.3.1 Methods of record keeping for toroids

The first step in evaluating the results of a given firing is to record all the details about individual toroid location and orientation on the V-groove alumina setter plates within the kiln. We need this detailed information in order to look for systematic variations in toroid straightness or other physical or magnetic properties which can be correlated with the firing process. Each toroid also carries with it the information on powder processing and forming conditions so that these factors can also be considered in analyzing phaser performance. The cataloging of the toroid records begins with a careful numbering of each sample, noting its position on the setter plate and the location of the setter in the kiln if more than one plate was used. We also record the upfacing surfaces of the toroid, i.e., those not in contact with the supporting setter plate, and the relation of these surfaces to those of the steel pin in the original forming process.

After the firing is completed, each toroid is numbered and its position and orientation within the kiln noted. Toroids are then examined visually for cracks or other flaws and for distortions in external shape. Using a six-inch metal rule and strong back-lighting, one can readily detect a bowing of 0.005 inch or more on external surfaces. Since the part is isostatically pressed, these surfaces are not smooth enough to warrant more quantitative study of external shape. In any event, the critical test for straightness involves the internal toroid surfaces, i.e., the straightness of the center hole, since all external surfaces are machined.

2.3.2 Toroid straightness evaluation

Straightness of the rectangular center hole is determined primarily by a pin clearance test. This was a standard test for this configuration phase shifter. A ceramic pin machined to dimensions about 6 percent smaller than the fired cross section of the toroid is used. The pin is required to fall through the hole by its own weight.

We have used two pins in our pin clearance evaluation of Li-Ti-ferrite toroids. The smallest corresponds to the same percent undersize as used in production testing. The other is two mils larger in each dimension making it about 4 percent undersize in cross section. Assuming a uniform cross section for the hole, the larger clearance pin will not pass through a toroid with a bow of greater than 4 mils.

After testing for pin clearance, the toroids are placed in individual plastic boxes with complete composition and firing information recorded on the box. Samples are then sent to a local machine shop for grinding to the desired wall thicknesses. The wall thickness control at the machine shop must be kept to a mechanical measurement at the ends of the toroid, since the shop has no way of establishing an average wall thickness value by making measurements along the length.

Uniformity in wall thickness on the machined toroid depends on the precision in keying to the toroid ends and on the straightness of the center hole relative to the outer surfaces. For the evaluation of wall thickness after machining, we have made use of an ultrasonic thickness gauge (Panametrics, Inc., Waltham, Mass.). This gauge is capable of continuous thickness determination along the length of the toroid. It operates on the pulse echo principle, in which transit time is measured for sound waves launched from the outside surface and reflected from the interior surface of the toroid. A measurement precision of ± 0.0003 inch is claimed for the instrument. With micrometer measurements at the ends of the toroid, one can achieve an accuracy of ± 0.0005 inch. In a separate study to be described in this section we have

been able to establish that toroid density is constant along the length in isostatically pressed samples. One may therefore assume that the sound velocity, which depends on density, will be constant and that thickness determinations can be obtained directly.

The results of ultrasonic measurements of wall thickness on machined toroidal samples will be covered in Sec. 2.7, along with data on hysteresis properties. The remainder of this section will be concerned with bulk property measurements on the composition finally chosen for the phase shifter studies.

2.3.3 Bulk property measurements

Before the ultrasonic equipment was available for evaluation of wall thickness, two firings were made involving toroids from a series of 2 kg experimental batches of the final 1200 gauss ferrite composition. Measurements of center hole dimensions and wall thickness were made on toroids cut into 0.5 inch segments. Determinations were also made of density, average grain size, and hysteresis loop properties on unannealed and annealed materials.

2.3.3.1 Experimental procedures

The toroids were isostatically formed at 15,000 psi around a rectangular cross-steel pin. They were substantially fired at a standard heating rate of 60°C/hr. to 1020°C, a soak at 1020° for 10 hours, and a cooling rate of 60°/m to 700°, all in flowing oxygen gas.

After firing, the toroids were sent out for machining on the exterior surfaces along the five-inch length. Wall thickness was to be 0.058 inch on all four sides. The machining on the exterior surfaces was to be parallel to the center hole surfaces so as to produce uniform ferrite walls as viewed at the opposite ends of the toroid. Since the external surfaces were made true and parallel by machining, any deviations in straightness of the center hole along its length would result in a local thickening and thinning of the toroid

walls. A series of transverse cuts would then reveal the variations along the length of the toroid. At the same time, one could check on the constancy of the center hole dimensions. Any variation in these dimensions would also affect toroid wall thickness.

Segments were polished and etched for microscopic study. Grain size was determined on thermally etched sections. Average grain size values were obtained by linear grain count analysis from photographs at various magnifications. Photographs at 275X are shown in Figs. 50a, 50b, 50c, and 50d.

2.3.3.2 Experimental results

Measurements on these early toroidal samples dealt primarily with the question of constancy in the center hole dimension. Any variations here would indicate that the density of the compacted powder and/or the fired density of the toroid was changing from one region to the next. We were able to establish by displacement measurements that the fired density was the same, within experimental error, for each segment of the toroid. Therefore, any fluctuation in center hole dimensions would be directly attributable to variations in shrinkage, and this could only be caused by variations in green density.

Using a travelling stage microscope, we measured center hole dimensions of segments cut from each of three toroids. The accuracy of this microscope is estimated to be ± 0.0005 inch at the 50X magnification. Another nine toroids cut into short segments were measured with a dial-indicating micrometer, which has a measurement accuracy in the same range. All of these data indicated constant dimensions of 0.106×0.134 inch for the center hole. The standard deviation was $S = 0.0009$, or about one percent of the dimensions measured.

Values of toroid wall thickness measured at the same time and reported in detail in Table 4 show considerably more variation within each toroid and between toroids as well. The toroids were produced from 2 kg experimental batches at the beginning of the toroid verification phase of the MMT program.

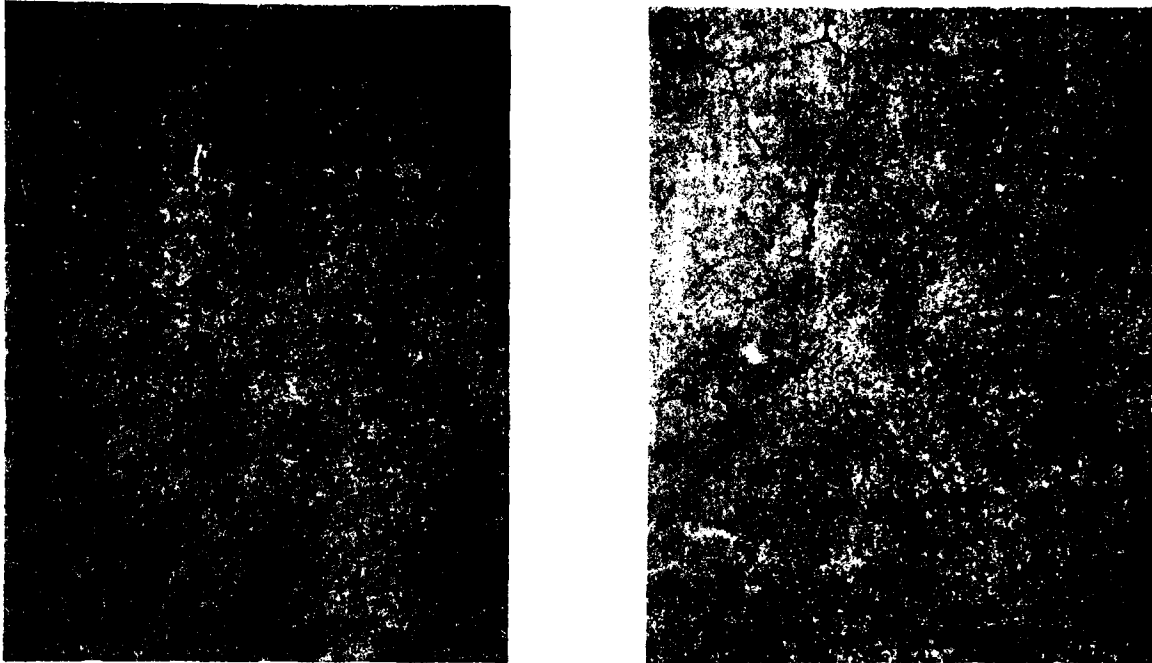


Figure 50a. Photographs at 275X of 1200 Gauss Ferrite Material.

PBN-80-13

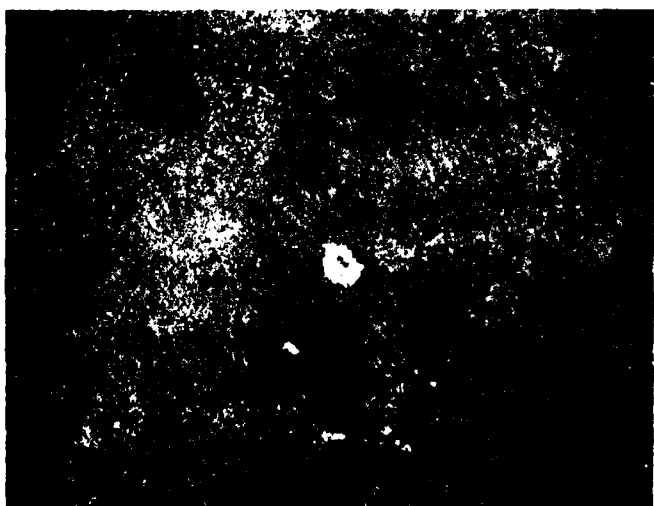
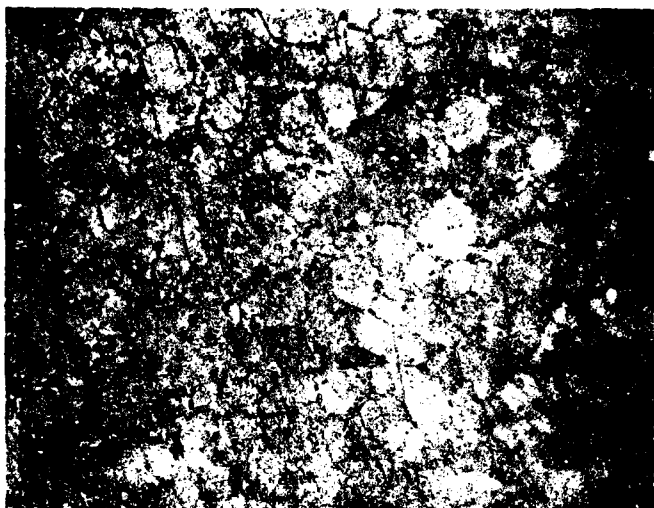
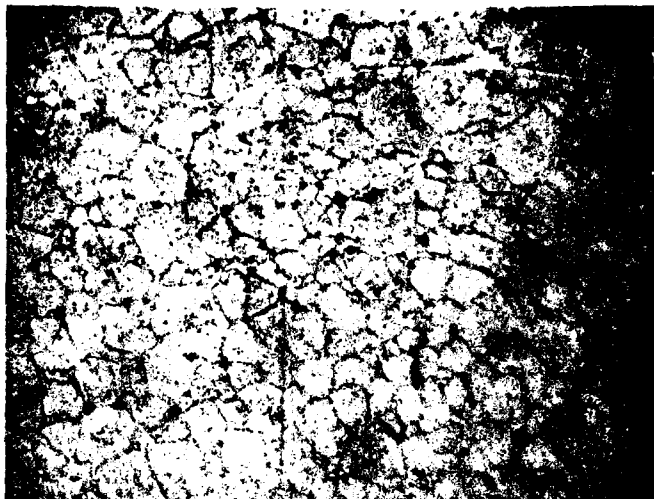


Figure 50b. Photographs at 275X of 1200 Gauss Ferrite Material.

PBN-80-14

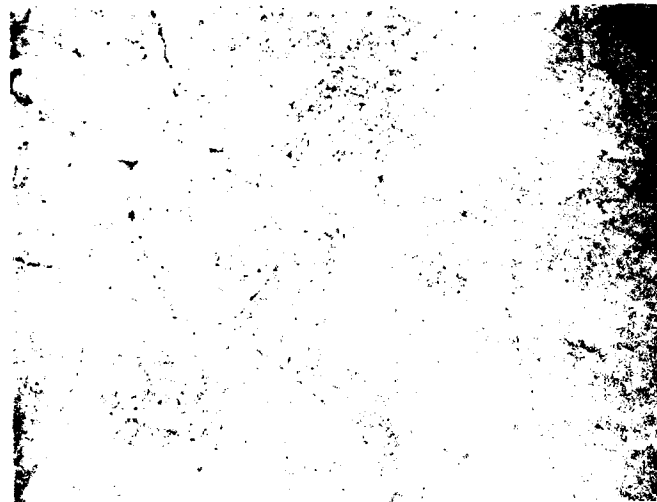


Figure 50c. Photographs at 275X of 1200 Gauss Ferrite Material.

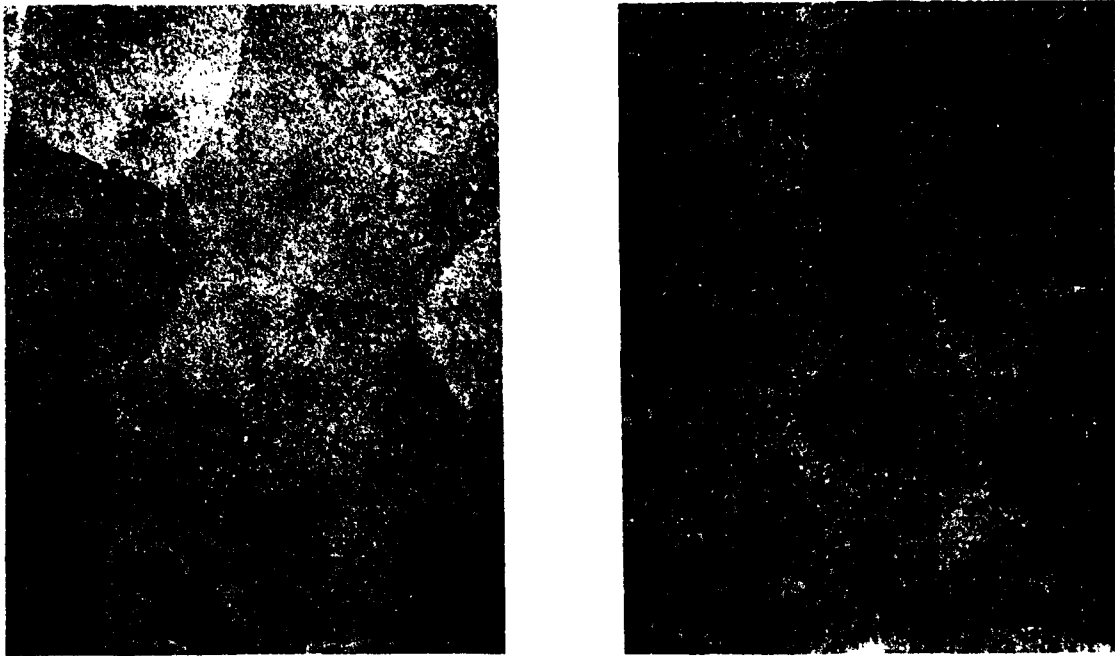


Figure 50d. Photographs at 275X of 1200 Gauss Ferrite Material.

TABLE 4
COMPOSITION AND PHYSICAL PROPERTIES OF FERRITE TOROIDS

Toroid No.	Composition	Firing Conditions		Pin No.	Setter Location	Pin Clearance Test		Thin Wall	Av. Thick.	Stand. Dev.	H _c	B _r	No. Samples Fired	Comments
		Temp.	Time			0.127" - 0.097"	0.125" - 0.096"							
1	LTC 365-005	1000	10	II	1/1	Not Measured				1.10	548	3	Improved machined setter and alum. caps were used.	
2	LTZNC 57-05-005	985	10	II	1/1					1.12	864	3		Slight warp
3	LTC 545-005	1000	10	II	1/1					1.01	552	3		
4	LMTCF 53-005(2)	1000	5	II	7					0.94	893	5		
5	LTZNC 61-10-05-005(2)	1000	10	II	1/1					0.99	822	6		
6	LTZNC 57-05-005(2)	1000	10	II	2/2					0.72	960	5		
7	LTZNC 57-05-005(2)	1020	10	III	1/1					0.59	837	4	Density = 4.36g/cc	
8	LTC 53-05-005	1000	10	II	1/1					1.65	857	3		
9	LTZC 61-10-005(5)	1000	10	II	1/1					0.78	646	6		
10	LTZC 61-10-005(5)	1000	10	II	1/1					2.51	972	6		
11	LTC 545-005	985	10	II	1/1					1.21	860	3		
12	LTC 365-005	985	10	II	1/1					1.45	782	3		
13	LTN 53-05	1020	10	II	1/1					1.37	826	3		
14	LTNC 53-05-005	1020	10	II	1/1					1.36	846	3		
15	LMTCF 005-53(2)	1000	5	II	5					0.92	799	5		
16	LTC 565-005	1000	10	II	1/1					0.76	681	3		
17	LTZNC 57-05-005	1020	10	II	1/1					1.12	881	3		
18	LTZNC 61-10-05-005(2)	990	5	II	1/1	--	--	B	0.0549	0.0012	1.41	904	5	Density = 99.3%
19	LTZNC 61-10-05-005(2)	1000	10	II	1/1	--	--	B	0.0536	0.0019	1.15	856	2	Density = 98.8%
20	LTZNC 61-10-05-005(2)	1000	10	II	1/1	--	--	D	0.0523	0.0009	1.09	883	2	Density = 99.0%
21	LTZNC 61-10-05-005(3)	1000	10	II	1/1	--	--	B	0.0534	0.0006	1.21	888	3	
22	LTZNC 61-10-05-005(3)	1000	10	II	1/1	--	--	B	0.0521	0.0010	1.17	891	4	Powder dried @ 80°C

TABLE 4

COMPOSITION AND PHYSICAL PROPERTIES OF FERRITE TOROIDS (Continued)

Toroid No.	Composition	Firing Conditions		Pin No.	Setter Location	Pin Clearance Test			Av. Thick.	Stand. Dev.	H_c	B _r	No. Samples Fired	Comments
		Temp.	Time			0.127" ± 0.097"	0.125" ± 0.096"	Thin Wall						
23	LTZNC 61-10-05-005(3)	1000	10	II	1/1	--	No Go	D	0.0542	0.0029	1.16	860	4	Pin Reject
24	LTZNC 61-10-05-005(3)	1000	10	II	1/1	--	--	B	0.0536	0.0004	1.18	867	4	
25	LTZNC 61-10-05-005(3)	1020	10	II	1/1	--	--	B	0.0531	0.0007	1.23	883	4	First use of oxidation soak
26	LTZNC 61-10-05-005(3)	1020	10	II	1/1	--	--	D	0.0550	0.0014	1.26	869	4	First use of oxidation soak
27	LTZNC 61-10-05-005(3)	1020	10	II	1/1	--	--	D	0.0533	0.0016	1.26	868	4	First use of oxidation soak
28	LTZNC 61-10-05-005(3)	1020	10	II	1/1	--	--	D	0.0547	0.0010	1.26	869	4	First use of oxidation soak
29	LTZNC 61-10-05-005(3)	1020	10	II	1/1	--	--	B	0.0539	0.0011	0.88	932	4	Density = 99.4%
30	LTZNC 61-10-05-005(3)	1020	10	II	1/1	--	--	B	0.0526	0.0010	1.13	871	4	Density = 98.5%
31	LTZNC 61-10-05-005G-10	1020	10	V	1/1	--	--	--	--	--	0.76	794	6	
32	LTZNC 61-10-05-005G-10	1020	10	V	1/1	--	--	--	--	--	0.76	802	6	
33	LTZNC 61-10-05-005G-10	1020	10	V	1/1	--	--	--	--	--	0.79	794	6	Density = 98.8%
34	LTZNC 61-10-05-005G-10	1020	10	V	1/1	--	--	--	--	--	0.70	802	6	
35	LTZNC 61-10-05-005G-10	1020	10	V	1/1	--	--	--	--	--	0.74	869	6	
36	LTZNC 63-10-05-005(1)	1020	10	III	9	1/1	Drop	Drop	0.46	847	4	4		
37	LTZNC 63-10-05-005(1)	1020	10	III	11	1/1	Push	Push	0.47	858	4	4		
38	LTZNC 63-10-05-005(2)	1020	10	III	9	1/1	Push	Push	0.50	903	4	4		
39	LTZNC 63-10-05-005(2)	1020	10	III	11	1/1	Push	Push	0.50	864	4	4		
40	LTZNC 61-10-05-005(G-10)	1020	10	VI	9	2/3	Drop	Drop	0.97	765	12	12		Three fired-in-place (FIP) samples included.
41	LTZNC 61-10-05-005G10	1020	10	VI	11	1/3	Drop	Drop	1.02	862	12	12		Three regular toroids were cut into 9 sections each for annealing experiment
42	LTZNC 61-10-05-005G-10	1020	10	VI	9	3/3	Push	Push	1.01	822	12	12		
43	LTZNC 61-10-05-005G-10	1020	10	VI	10	3/3	Push	Push	1.06	849	15	15		7 samples were cut into 3 sections for comparison measurements
44	LTZNC 61-10-05-005(6)	1020	10	VI	9	3/3	Drop	Drop	0.73	925	15	15		

TABLE 4

COMPOSITION AND PHYSICAL PROPERTIES OF FERRITE TOROIDS (Continued)

Toroid No.	Composition	Firing Conditions		Pin No.	Pin Location	Pin Clearance Test		Thin Wall	Av. Thick.	Stand. Dev.	H _c	B _r	No. Samples Fired	Comments
		Temp.	Time			0.125" x 0.097"	0.125" x 0.096"							
45	LTZNC 61-10-05-005(6)	1020	10	VI 11	3/3	Drop	--	Not Measured			0.81	963	15	
46	LTZNC 61-10-05-005(5)	1020	10	VI 9	3/3	Drop	--				1.01	848	15	
47	LTZNC 61-10-05-005(2)	1020	10	VI 11	2/3	Drop	--				1.08	900	15	
48	LTZNC 61-10-05-005(3)	1020	10	VI 11	2/3	Drop	--				1.10	871	15	
49	LTZNC 61-10-05-005(7)	1020	10	II 10	1/2	Push	Drop				0.78	920	6	
50	LTZNC 61-10-05-005(8)	1020	10	II 10	2/2	Push	Drop				1.09	861	6	
51	LTZNC 61-10-05-005(7)	1020	10	V 13	1/1	Drop	--	B	0.0551	0.0006	0.76	951	5	H _c values low and B _r values high for all 5 samples
52	LTZNC 61-10-05-005(7)	1020	10	V 10	1/1	Push	Drop	B	0.0527	0.0020	0.73	949	5	
53	LTZNC 61-10-05-005(7)	1020	10	V 11	1/1	Push	Drop	D	0.0548	0.0015	0.76	943	5	
54	LTZNC 61-10-05-005(6)	1020	10	V 11	1/1	Push	Drop	D	0.0542	0.0023	0.70	975	5	
55	LTZNC 61-10-05-005(6)	1020	10	V 11	1/1	Push	--	B	0.0545	0.0019	0.71	947	5	
56	LTZNC 61-10-05-005(5)	1020	10	VI 17	1/3	Drop	--	B	0.0563	0.0015	1.14	836	21	First firing with new pins No. 16 and No. 17 New pins No. 14 and No. 15 are rejects.
57	LTZNC 61-10-05-005(6)	1020	10	VI 11	1/3	Push	--	B	0.0540	0.0025	0.83	940	21	
58	LTZNC 61-10-05-005(6)	1020	10	VI 10	1/3	Push	Drop	D	0.0546	0.0022	0.85	947	21	
59	LTZNC 61-10-05-005(6)	1020	10	VI 13	1/3	Drop	--	D	0.0570	0.0015	0.88	925	21	
60	LTZNC 61-10-05-005(5)	1020	10	VI 16	1/3	Drop	--	B	0.0577	0.0012	1.18	840	21	
61	LTZNC 61-10-05-005(7)	1020	10	VI 16	2/3	Drop	--	D	0.0541	0.0003	1.09	979	21	Bottom and middle setter samples had one cap per sample
62	LTZNC 61-10-05-005(7)	1020	10	VI 17	2/3	Drop	--	D	0.0550	0.0007	1.11	936	21	
63	LTZNC 61-10-05-005(7)	1020	10	VI 11	2/3	Push	Drop	B	0.0565	0.0009	1.06	896	21	
64	LTZNC 61-10-05-005(7)	1020	10	VI 10	2/3	Drop	--	D	0.0581	0.0009	1.14	907	21	
65	LTZNC 61-10-05-005(5)	1020	10	VI 10	2/3	Drop	--	D	0.0535	0.0009	1.11	868	21	
66	LTZNC 61-10-05-005(5)	1020	10	VI 17	2/3	Drop	--	B	0.0539	0.0008	1.12	885	21	
67	LTZNC 61-10-05-005(6)	1020	10	VI 13	2/3	Push	Drop	D	0.0583	0.0013	0.87	918	21	
68	LTZNC 61-10-05-005(7)	1020	10	VI 13	3/3	Push	Drop	C	0.0572	0.0016	1.12	864	21	

TABLE 4

COMPOSITION AND PHYSICAL PROPERTIES OF FERRITE TOROIDS (Continued)

Toroid No.	Composition	Firing Conditions		Pin No.	Setter Location	Pin Clearance Test		Thin Wall	Av. Thick.	Stand. Dev.	H _c	B _r	No. Samples Fired	Comments
		Temp.	Time			0.127" ± 0.097"	0.125" ± 0.096"							
69	LTZNC 61-10-05-005(6)	1020	10	VI 17	3/3	Push	Drop	B	0.0582	0.0012	0.93	927	21	An extra cap was used on these samples to bridge the usual two caps
70	LTZNC 61-10-05-005(6)	1020	10	VI 16	3/3	Push	Drop	D	0.0564	0.0017	0.92	938	21	
71	LTZNC 61-10-05-005(6)	1020	10	VI 10	3/3	Drop	--	D	0.0577	0.0010	0.90	950	21	
72	LTZNC 61-10-05-005(6)	1020	10	VI 11	3/3	Push	Drop	B	0.0554	0.0021	0.88	949	21	
73	LTZNC 61-10-05-005(6)	1020	10	VI 17	3/3	Drop	--	B	0.0555	0.0004	0.87	951	21	
74	LTZNC 61-10-05-005(6)	1020	10	VI 11	3/3	Drop	--	D	0.0561	0.0017	0.90	934	21	Alumina pin first used in this firing for two samples. O ₂ flow increased from 3 lpm to 5 lpm
75	LTZNC 61-10-05-005(6)	1020	10	VI 16	3/3	Drop	--	B	0.0569	0.0008	0.92	938	21	
76	LTZNC 61-10-05-005(3)	1020	10	VI 9	3/3	Drop	--	C	0.0562	0.0017	1.16	817	21	
77	Panametrics (5)	1020	10	VI 17	1/3	Drop	--	--	--	Broken	--	--	21	
78	Panametrics (5)	1020	10	VI 13	1/3	Drop	--	--	--	Broken	--	--	21	
79	Panametrics (5)	1020	10	VI 16	1/3	Drop	--	--	--	--	--	--	21	Pin dismounted from base
80	LTZNC 61-10-05-005(8)	1020	10	VI 10	2/3	Push	Drop	D	0.0594	0.0014	1.18	829	21	
81	LTZNC 61-10-05-005(8)	1020	10	VI 9	2/3	Drop	--	B	0.0588	0.0015	1.17	842	21	
82	LTZNC 61-10-05-005(5)	1020	10	VI 13	2/3	Push	Drop	D	0.0578	0.0009	1.17	830	21	
83	LTZNC 61-10-05-005(5)	1020	10	VI 13	2/3	Drop	--	B	0.0544	0.0019	1.09	884	21	
84	LTZNC 61-10-05-005(5)	1020	10	VI 16	2/3	Drop	--	B	0.0591	0.0005	1.20	838	21	Thermal caps again varied with no obvious trend, e.g., No. 84 - 1 long cap No. 85 - 3 caps No. 86 - reg. 2 caps No. 87 - reg. 2 caps No. 88 - 3 caps No. 89 - 2 caps No. 90 - 3 caps No. 91 - 2 caps
85	LTZNC 61-10-05-005(8)	1020	10	VI 17	3/3	Push	--	B	0.0557	0.0030	1.10	814	21	
86	LTZNC 61-10-05-005(8)	1020	10	VI 16	3/3	Push	Drop	B	0.0582	0.0011	1.19	833	21	
87	LTZNC 61-10-05-005(8)	1020	10	VI 11	3/3	--	Push	B	0.0546	0.0020	1.07	818	21	
88	LTZNC 61-10-05-005(8)	1020	10	VI 10	3/3	Push	--	D	0.0581	0.0014	1.15	817	21	
89	LTZNC 61-10-05-005(8)	1020	10	VI 17	3/3	--	Push	B	0.0537	0.0029	1.06	838	21	
90	LTZNC 61-10-05-005(8)	1020	10	VI 16	3/3	Drop	--	B	0.0589	0.0017	1.15	811	21	

TABLE 4

COMPOSITION AND PHYSICAL PROPERTIES OF FERRITE TOROIDS (Continued)

Toroid No.	Composition	Firing Conditions		Pin No.	Setter Location	Pin Clearance Test		Thin Wall	Av. Thick.	Stand. Dev.	H _c	B _r	No. Samples Fired	Comments
		Temp.	Time			0.127"	0.125"							
91	LTZNC 61-10-05-005(8)	1020	10	VI 11	3/3	Push	--	B	0.0532	0.0027	1.10	852	21	O ₂ flow 5 lpm
92	LTZNC 61-10-05-005G-11	1020	10	VI 11	1/3	Push	--	D	0.0531	0.0021	1.05	832	20	
93	LTZNC 61-10-05-005G-11	1020	10	VI 13	1/3	Drop	--	D	0.0577	0.0012	1.11	858	20	
94	LTZNC 61-10-05-005G-11	1020	10	VI 10	1/3	Drop	--	D	0.0576	0.0010	1.07	836	20	Pin Reject Standard
95	LTZNC 61-10-05-005G-11	1020	10	VI 17	1/3	--	--	D	0.0551	0.0020	1.05	829	20	
96	LTZNC 61-10-05-005G-11	1020	10	VI 10	1/3	Push	Drop	D	0.0573	0.0020	1.12	827	20	
97	LTZNC 61-10-05-005G-11	1020	10	VI 11	1/3	Push	Drop	B	0.0580	0.0015	1.15	811	20	Pin Reject Standard
98	LTZNC 61-10-05-005G-11	1020	10	VI 13	1/3	Push	--	D	0.0552	0.0032	1.14	827	20	
99	LTZNC 61-10-05-005G-11	1020	10	VI 17	1/3	Push	--	D	0.0561	0.0021	1.14	836	20	
100	LTZNC 61-10-05-005(8)	1020	10	VI 11	2/3	Push	Drop	D	0.0559	0.0018	1.19	857	20	Pin Reject Standard
101	LTZNC 61-10-05-005(8)	1020	10	VI 13	2/3	Drop	--	D	0.0591	0.0007	1.22	835	20	
102	LTZNC 61-10-05-005(8)	1020	10	VI 10	2/3	Drop	--	D	0.0584	0.0011	1.20	845	20	
103	LTZNC 61-10-05-005(8)	1020	10	VI 17	2/3	Push	Drop	D	0.0532	0.0026	1.13	875	20	Pin Reject Standard
104	LTZNC 61-10-05-005(8)	1020	10	VI 10	2/3	Push	--	D	0.0568	0.0017	1.22	860	20	
105	LTZNC 61-10-05-005(8)	1020	10	VI 11	2/3	Push	Drop	D	0.0602	0.0013	1.24	811	20	
106	LTZNC 61-10-05-005(8)	1020	10	VI 13	2/3	Push	Drop	D	0.0577	0.0011	1.22	853	20	Pin Reject Standard
107	LTZNC 61-10-05-005(8)	1020	10	VI 17	2/3	Drop	--	D	0.0573	0.0025	1.14	819	20	
108	LTZNC 61-10-05-005G-11	1020	10	VI 16	3/3	Push	Drop	D	0.0577	0.0015	1.14	836	20	
109	LTZNC 61-10-05-005G-11	1020	10	VI 16	3/3	Push	Drop	B	0.0561	0.0020	1.19	839	20	Pin Reject Standard
110	LTZNC 61-10-05-005(8)	1020	10	VI 16	3/3	Push	Drop	D	0.0583	0.0012	1.20	829	20	
111	LTZNC 61-10-05-005(8)	1020	10	VI 16	3/3	Drop	--	D	0.0583	0.0012	1.20	829	20	

TABLE 4

COMPOSITION AND PHYSICAL PROPERTIES OF FERRITE TOROIDS (Continued)

Toroid No.	Composition	Firing Conditions		Pin Location	Pin Clearance Test		Thin Wall	Av. Thick.	Stand. Dev.	H _c	B _r	No. Samples Fired	Comments
		Temp.	Time		0.127"	0.125"							
112	LTZNC 61-10-05-005(6)	1020	10	V1 13	Drop	--	D	0.0575	0.0012	0.88	952	15	Second firing which used oxidation soak @ 600°-700°
113	LTZNC 61-10-05-005(6)	Standard Firing Conditions with 700° 3 Hrs. Soak		V1 16	Drop	--	D	0.0580	0.0003	0.90	980	15	
114	LTZNC 61-10-05-005(6)			V1 17	Drop	--	B	0.0573	0.0012	0.88	979	15	
115	LTZNC 61-10-05-005(6)			V1 10	Drop	--	B	0.0580	0.0005	0.89	978	15	
116	LTZNC 61-10-05-005(6)			V1 11	Drop	--	B	0.0582	0.0071	0.91	955	15	
117	LTZNC 61-10-05-005(8)			V1 17	Drop	--	B	0.0584	0.0003	1.22	852	15	
118	LTZNC 61-10-05-005(8)			V1 16	Drop	--	D	0.0587	0.0008	1.20	843	15	
119	LTZNC 61-10-05-005(8)			V1 13	Drop	--	D	0.0569	0.0006	1.19	862	15	
120	LTZNC 61-10-05-005(8)			V1 11	Push	Drop	D	0.0557	0.0011	1.18	865	15	
121	LTZNC 61-10-05-005(8)			V1 10	Push	--	B	0.0534	0.0022	1.15	871	15	
122	LTZNC 61-10-05-005(8)			V1 17	Push	Drop	D	0.0578	0.0007	1.15	838	15	
123	LTZNC 61-10-05-005(8)			V1 16	Drop	--	B	0.0561	0.0017	1.18	861	15	
124	LTZNC 61-10-05-005(8)			V1 13	Push	Drop	D	0.0591	0.0015	1.19	822	15	
125	LTZNC 61-10-05-005(8)			V1 11	Push	--	B	0.0575	0.0010	1.17	832	15	
126	LTZNC 61-10-05-005(8)			V1 10	Push	--	B	0.0571	0.0013	1.16	853	15	
127	LTZNC 61-10-05-005G-10			V1 10	Drop	--	D	0.0543	0.0014	1.06	866	25	G-10 and G-11 samples more susceptible to warping
128	LTZNC 61-10-05-005G-10			V1 11	Drop	--	D	0.0581	0.0005	0.98	832	25	
129	LTZNC 61-10-05-005G-10			V1 13	Push	Drop	B	0.0557	0.0013	1.07	837	25	
130	LTZNC 61-10-05-005G-10			V1 16	Push	--	D	0.0461	0.0043	0.96	847	25	
131	LTZNC 61-10-05-005G-10			V1 17	--	Push	B	0.0533	0.0022	1.02	825	25	
132	LTZNC 61-10-05-005G-10			V1 10	Drop	--	B	0.0583	0.0015	1.01	820	25	
133	LTZNC 61-10-05-005G-10			V1 11	--	Push	C	0.0493	0.0056	1.05	725	25	
134	LTZNC 61-10-05-005G-10			V1 17	Drop	--	D	0.0587	0.0018	1.03	839	25	
135	LTZNC 61-10-05-005G-10			V1 16	--	Push	B	0.0578	0.0024	1.11	832	25	
136	LTZNC 61-10-05-005(6)			V1 17	Push	--	D	0.0553	0.0026	0.88	979	25	
137	LTZNC 61-10-05-005(6)			V1 16	Drop	--	D	0.0586	0.0010	0.89	958	25	
138	LTZNC 61-10-05-005(6)			V1 13	Drop	--	B	0.0575	0.0005	0.89	967	25	

TABLE 4

COMPOSITION AND PHYSICAL PROPERTIES OF FERRITE TOROIDS (Continued)

Toroid No.	Composition	Firing Conditions		Pin Setter Location	Pin Clearance Test		Thin Wall	Av. Thick.	Stand. Dev.	H _c	B _r	No. Samples Fired	Comments
		Temp.	Time		0.127" ± 0.097"	0.125" ± 0.096"							
139	LTZNC 61-10-05-005G-11	1020	10	VI 11	2/3	Push	--	D 0.0521	0.0027	0.88	978	25	
140	LTZNC 61-10-05-005G-11	Standard Firing		VI 10	2/3	Push	Drop	B 0.0557	0.0012	0.87	969	25	
141	LTZNC 61-10-05-005G-11	Conditions with 700° 3 hrs.		VI 10	3/3	Push	--	B 0.0577	0.0010	1.09	816	25	
142	LTZNC 61-10-05-005G-11			VI 17	3/3	Push	--	D 0.0574	0.0023	1.06	807	25	
143	LTZNC 61-10-05-005G-11	Soak		VI 10	3/3	Push	Drop	D 0.0585	0.0014	1.04	818	25	
144	LTZNC 61-10-05-005G-11			VI 11	3/3	Drop	--	B 0.0557	0.0010	0.99	854	25	
145	LTZNC 61-10-05-005G-11			VI 13	3/3	--	--	D 0.0476	0.0075	1.00	822	25	Pin Reject
146	LTZNC 61-10-05-005G-11			VI 16	3/3	Push	Drop	D 0.0563	0.0025	1.06	823	25	
147	LTZNC 61-10-05-005G-11			VI 17	3/3	Push	--	C 0.0555	0.0032	1.06	814	25	
148	LTZNC 61-10-05-005G-10			VI 13	3/3	Push	Drop	D 0.0590	0.0015	1.10	820	25	
149	LTZNC 61-10-05-005G-10			VI 11	1/3	Drop	--	D 0.0537	0.0016	1.08	861	20	
150	LTZNC 61-10-05-005G-10			VI 10	1/3	Drop	--	D 0.0568	0.0011	1.07	858	20	
151	LTZNC 61-10-05-005G-10			VI 17	1/3	Push	--	D 0.0564	0.0027	1.04	746	20	
152	LTZNC 61-10-05-005G-10			VI 16	1/3	Push	--	B 0.0509	0.0032	0.99	844	20	
153	LTZNC 61-10-05-005G-10			VI 13	1/3	Push	Drop	A 0.0585	0.0016	1.06	823	20	
154	LTZNC 61-10-05-005G-10			VI 11	1/3	Drop	--	D 0.0560	0.0017	1.07	842	20	
155	LTZNC 61-10-05-005G-10			VI 16	1/3	Push	--	C 0.0526	0.0035	1.04	783	20	
156	LTZNC 61-10-05-005G-11			VI 11	2/3	Push	Drop	B 0.0569	0.0013	1.08	859	20	
157	LTZNC 61-10-05-005G-11			VI 10	2/3	Push	Drop	B 0.0564	0.0015	1.07	850	20	
158	LTZNC 61-10-05-005G-11			VI 17	2/3	Push	Drop	D 0.0554	0.0016	1.08	840	20	
159	LTZNC 61-10-05-005G-11			VI 16	2/3	Push	--	B 0.0535	0.0019	1.04	826	20	
160	LTZNC 61-10-05-005G-11			VI 13	2/3	--	Push	D 0.0501	0.0032	1.00	827	20	
161	LTZNC 61-10-05-005G-11			VI 11	2/3	Push	--	D 0.0550	0.0032	1.05	820	20	

TABLE 4

COMPOSITION AND PHYSICAL PROPERTIES OF FERRITE TOROIDS (Continued)

Toroid No.	Composition	Firing Conditions		Pin No.	Setter Location	Pin Clearance Test		Thin Wall	Av. Thick.	Stand. Dev.	H _c	H _r	No. Samples Fired	Comments
		Temp.	Time			0.127" > 0.097"	0.125" > 0.096"							
162	LTZNC 61-10-05-005G-11	1020	10	VI 10	2/3	Drop	--	B	0.0565	0.0011	1.06	847	20	O ₂ flow of 5 lpm still continuing
163	LTZNC 61-10-05-005G-11	Standard Firing		VI 13	3/3	Push	Drop	D	0.0589	0.0016	1.04	848	20	
164	LTZNC 61-10-05-005G-10	Conditions with 700°		VI 17	3/3	Push	Drop	D	0.0585	0.0018	1.06	825	20	
165	LTZNC 61-10-05-005G-10	3 Hrs. Soak		VI 17	3/3	Push	--	D	0.0543	0.0021	1.05	861	20	
166	LTZNC 61-10-05-005G-10			VI 13	3/3	Push	--	D	0.0595	0.0025	1.07	811	20	

The toroids machined to have uniform 0.058-inch walls at the ends before sectioning showed thickness ranging from 0.048 to 0.064 inches in extreme cases, i.e., 0.058 ± 0.010 . The more typical deviations from thickness uniformity was ± 0.007 inch, or about 1.2 percent of the long (5.2 inch) dimension.

The results of measurement on eleven toroids are shown in Table 5. Following the first two columns, which give sample and segment identification numbers, the next five columns give results on displacement density measurements for each segment. The density measurements are the same to within ± 0.3 percent, which is within measurement precision for this size sample. The toroid segments were all machined to the same external dimensions (within ~ 0.6 percent or 1.8 percent in volume) so that constancy in toroid volume (col. 6, Table 5) is a further indication that the center hole dimensions were also unchanging. The average value for toroid volume was 0.370 cc. with $S = 0.0046$, a standard deviation of 1.2 percent from the mean.

Density values between samples were also very nearly constant, a fact which is notable considering that they represent seven different batches of the given ferrite composition. The average density for these toroids was 4.303, about 99 percent of the X-ray value. The standard deviation was $S = 0.017$, or 0.4 percent of the mean density.

The next four columns of the table give wall thickness values measured at the two exposed ends of the toroid segments on each of the four walls. For example, in the first entry the thicknesses are 50.5 and 48.2 mils (0.0505 and 0.0482 inch) at the two exposed ends of the toroid sidewall designated No. 0. As this wall becomes thinner from one end (L) to the other (R), the opposite wall (No. 2) becomes thicker in the same direction, i.e., from 63.3 to 65.2 mils.

The results on wall thickness are consistent throughout. When the No. 1 wall gets thinner in one direction for a given segment, the corresponding data for wall No. 3 shows thickening in that same direction, and at the same rate. If, for example, sidewall No. 0 remains constant in thickness, sidewall No. 2 also remains constant along the segment length. An example of this is the

Table 5. TOROID STRAIGHTNESS AND PHYSICAL PROPERTIES

Designation	No.	Weight Air	Water Weight	Time	Volume	Density	Wall 0 Side	1 Top	2 Bottom	0 + 2 2	1 + 1 2	Ave Grain Size, μ	Porosity Fraction	Porosity N.B.S. H _g	Sum of Abs. H _g	at 10 Hz	at 5 GHz	4 + 4 ₀			
26025-74 LTZNC61(4)02	2	1.583	1.216	1.714	0.368	4.302	1.58.2 R. 48.2 AVE 48.4	61.0 60.2 60.8	55.9 56.5 56.2	56.8	56.3	95	1.01	5.5	4.53	2.63	18.6	0.00396	0.2455	1200	
5	1.540	1.214	1.714	0.367	4.305		55.0 55.0 55.0	59.2 59.2 59.2	57.4 57.4 57.4	57.3	56.4			6.4	8.48						
8	1.578	1.213	1.714	0.365	4.311		54.2 57.0 57.0	58.2 58.9 58.8	58.9 58.9 58.9	54.0	56.8			65	409						
26025-74 LTZNC61(5)03	1	1.584	1.226	1.714	0.371	4.302	58.2 58.2 58.2	57.7 57.7 57.7	58.4 58.4 58.4	58.2	56.1	132	1.01	6.2	2.66	4.08	16.5	0.00221	0.2426	1231	
6	1.540	1.204	1.714	0.365	4.296		58.9 58.9 58.9	58.3 58.3 58.3	58.4 58.4 58.4	57.7	57.6			6.2	2.64						
9	1.594	1.224	1.714	0.371	4.296		58.8 58.8 58.8	58.3 58.3 58.3	58.4 58.4 58.4	58.6	58.3			6.5	752						
26025-74 LTZNC61(7)05	1	1.605	1.232	1.714	0.374	4.291	58.3 58.3 58.3	58.3 58.3 58.3	58.3 58.3 58.3	58.6	56.4	14	0.99	1.37	959	4.68	18.3	0.00283	0.1996	1217	
5	1.610	1.235	1.714	0.376	4.282		58.4 58.4 58.4	58.3 58.3 58.3	58.3 58.3 58.3	58.9	58.9			1.11	822						
9	1.616	1.241	1.714	0.376	4.298		58.8 58.8 58.8	58.3 58.3 58.3	58.4 58.4 58.4	59.2	58.7			1.00	888						
26025-74 LTZNC61(3)06	1	1.601	1.228	1.714	0.374	4.281	58.8 58.8 58.8	58.3 58.3 58.3	58.4 58.4 58.4	58.7	58.0	30	0.987	1.13	831	4.78	18.41	0.00339	0.2445	1228	
4	1.622	1.246	1.714	0.378	4.294		58.7 58.7 58.7	58.2 58.2 58.2	58.3 58.3 58.3	58.6	58.7			1.14	858						
9	1.621	1.244	1.714	0.378	4.288		58.7 58.7 58.7	58.2 58.2 58.2	58.4 58.4 58.4	58.7	58.7			1.15	866						
26025-74 LTZNC61(5)011	1	1.580	1.213	1.712	0.368	4.293	61.3 61.3 61.3	63.1 63.1 63.1	63.1 63.1 63.1	58.5	63.1	24	0.99	1.12	862	5.32	18.7	0.00324	0.2166	1234	
4	1.570	1.205	1.712	0.366	4.290		58.7 58.7 58.7	58.2 58.2 58.2	58.3 58.3 58.3	57.8	57.9			1.14	872						
9	1.575	1.209	1.712	0.367	4.292		59.4 59.4 59.4	58.6 58.6 58.6	58.7 58.7 58.7	58.2	57.9			1.11	892						
26025-74 LTZNC61(8)012	1	1.583	1.199	1.712	0.365	4.282	51.3 51.3 51.3	59.9 59.9 59.9	64.2 64.2 64.2	55.7	58.4	31	0.99	1.10	898	5.39	18.06	0.00315	0.2213	1227	
4	1.549	1.189	1.712	0.365	4.291		58.9 58.9 58.9	58.3 58.3 58.3	58.4 58.4 58.4	57.5	56.4			1.11	859						
9	1.568	1.204	1.712	0.365	4.296		58.1 58.1 58.1	58.8 58.8 58.8	59.2 59.2 59.2	57.5	56.5			1.15	847						
26025-74 LTZNC61(6)014	1	1.604	1.214	1.712	0.371	4.323	55.2 55.2 55.2	54.5 54.5 54.5	56.8 56.8 56.8	58.7	58.7	3	1.015	86	866	5.39	18.06	0.00309	0.2814	1240	
4	1.608	1.226	1.712	0.373	4.311		56.7 56.7 56.7	55.3 55.3 55.3	58.6 58.6 58.6	56.9	57.1			84	959						
9	1.610	1.239	1.712	0.372	4.328		56.7 56.7 56.7	55.3 55.3 55.3	58.6 58.6 58.6	58.8	58.7			86	984						
26025-78 LTZNC61(7)02	1	1.615	1.244	1.712	0.372	4.341	58.2 58.2 58.2	62.2 62.2 62.2	60.3 60.3 60.3	59.4	58.2	100	1.001	82	922	7.03	18.27	0.00288	0.2384	1256	
4	1.576	1.213	1.712	0.364	4.320		58.8 58.8 58.8	61.5 61.5 61.5	60.7 60.7 60.7	58.8	58.7			83	930						
9	1.592	1.225	1.712	0.368	4.326		58.8 58.8 58.8	61.5 61.5 61.5	60.7 60.7 60.7	58.8	58.7			83	930						
26025-78 LTZNC61(8)06	1	1.603	1.213	1.712	0.371	4.321	58.8 58.8 58.8	61.5 61.5 61.5	60.7 60.7 60.7	58.8	58.7	27	1.075	1.78	889	4.92	18.41	0.00361	0.2381	1218	
3	1.605	1.235	1.712	0.371	4.326		58.8 58.8 58.8	61.5 61.5 61.5	60.7 60.7 60.7	58.8	58.7			1.19	893						
8	1.610	1.236	1.712	0.375	4.333		58.8 58.8 58.8	61.5 61.5 61.5	60.7 60.7 60.7	58.8	58.7			1.09	881						
26025-81 LTZNC61(8)08						(4.27)															
26025-81 LTZNC61(9)11						(4.26)															

61(5) composition (fourth entry down) segment No. 1 in Table 5, where wall thickness remains constant along the sample length. In contrast, sidewall No. 0 becomes thinner (60.6 to 59.2 mils) and the opposite sidewall becomes thicker (55.7 to 57.1 mils) in the same direction.

The next two columns give values of average grain size and analyzed cation content on processed powders. Grain size shows considerable variation in these different experimental batches, primarily as a function of iron concentration. The reason for this is that increasing Fe content enhances sintering and leads to somewhat better density and larger grain size. The variations in iron stoichiometry were deliberate attempts to examine the effect of this variable on the ferrite microstructure. The other major influence on microstructure is Bi_2O_3 content. This was held constant throughout the series of LTZNC61 batches.

The hysteresis properties H_c and B_r are also seen to be microstructure dependent. The data reported are on annealed samples for these and the phase shifter samples. A separate study has been made on the effect of a post-machining anneal on loop properties. Experiments were run at 200°, 400°, 600°, and 800°C and 600°C was chosen for all subsequent machined samples. The values of B_r and H_c for the various segments were calculated based on the average thickness of the smallest cross-sectional "flux limiting" wall.

Examination of the data indicated a correlation between ceramic density on the one hand and iron stoichiometry, grain size H_c and B_r . Since the remanent flux B_r is directly related to phase shift, this property was plotted versus density in Fig. 51.

The dielectric constant and dielectric loss tangent at 10 GHz are shown in Table 5. The measurement is made on rod-shaped samples by a waveguide perturbation technique in which the shift in cavity resonance for a sample of known volume yields the dielectric constant ϵ' . Measurement accuracy of ϵ' depends on the knowledge of sample volume. With rods approximately 1 mm in diameter, micrometer accuracy was ± 0.001 inch, which amounts to ± 0.025 mm

AD-A088 764

RAYTHEON CO WALTHAM MA RESEARCH DIV

F/G 17/9

PRODUCTION OF LITHIUM FERRITE ASSEMBLIES FOR PHASED ARRAY RADAR--ETC(U)

JUN 79 J J GREEN, H J VAN HOOK

DAAK40-78-C-0082

UNCLASSIFIED

S-2554

NL

2 OF 2

200
ALPHA

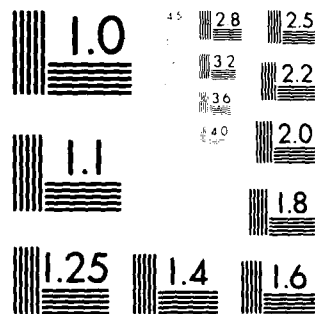
END

DATE

FILED

10-30

DTIC



MICROCOPY RESOLUTION TEST CHART
NATIONAL BUREAU OF STANDARDS-1963-A

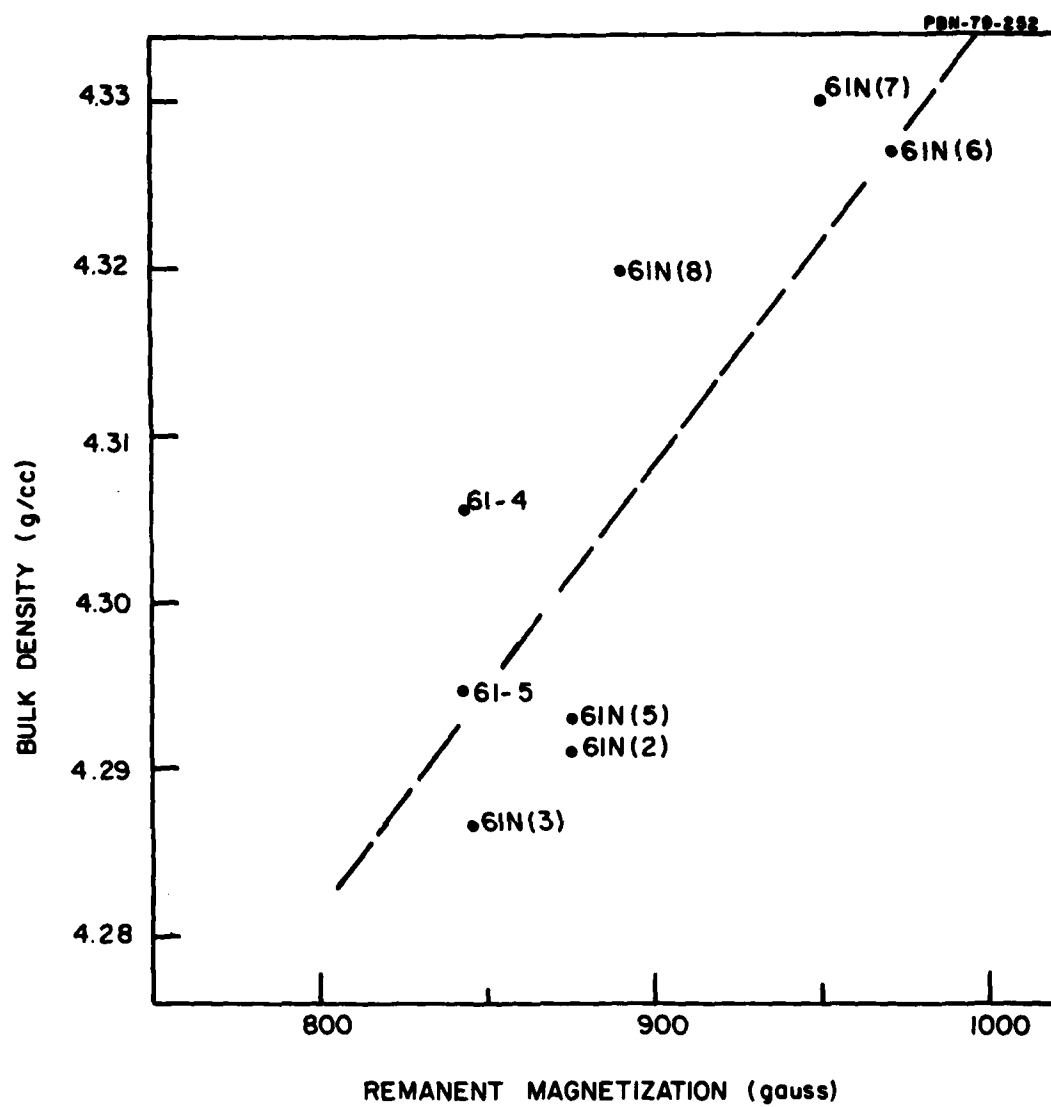


Figure 51. $4\pi M_r$ vs. Density in 1200 g Li-Ti-Ferrite.

or ± 2 percent in volume. Thus, variations in ϵ' of 18.3 ± 0.03 are within experimental error. Samples from the production batches G10 and G11 lie below this range, indicating densities below the other samples, a fact confirmed by density measurement. Data on dielectric loss tangent are in the range of 3 to 7×10^{-4} with no particular trend with ferrite composition or firing conditions.

The measurements of microwave permeability and magnetic loss were made at 5.5 GHz. As mentioned earlier, the permeability is affected by sample density and by changes in crystalline anisotropy. The permeability is apparently strongly dependent on density or Fe content, changing by as much as a factor of two in this series.

On the other hand, magnetic loss appears rather constant, with lower values for the first two nickel-free compositions and larger numbers for the remainder.

2.4 Development of Dielectric Material

The development of a dielectric composition suitable for firing in place (FIP) with the 1200 gauss Li-Ti-ferrite is one aspect of this program that gradually lost emphasis as the work progressed. The impetus for this change took place largely outside the Research Division through interactions between U. S. Army technical personnel and Raytheon systems engineering. For reasons that were outlined in the introduction, the need for a center-loaded phase control element which could make use of the FIP process was superseded by a side-loaded toroid-dielectric geometry. Nevertheless, in the interest of future systems design, it is well to outline the work accomplished in matching ferrite characteristics with an appropriate dielectric material.

In essence, the FIP process is the firing of a ferrite green body on to a premachined dense ceramic core whose dimensions are matched to the expected ferrite shrinkage and whose thermal expansion characteristic is closely mated to the ferrite to minimize stresses during cooling. The dielectric core should

be compositionally similar to the ferrite to minimize interdiffusional effects and, of course, it must be stable at the reaction temperature.

The first step in the process was a careful series of determinations of thermal expansion for the chosen ferrite composition. The basic idea is that the dielectric properties must accommodate to the ferrite and not the reverse. Samples of three ferrite compositions, one without Ni and two with Ni substitution, were isostatically pressed into rods at 15,000 psi (1060 kg-cm^{-2}) and fired at 1020°C for 10 hours in flowing oxygen, these being identical to forming and firing conditions for the toroids.

Figure 52 shows the data on thermal expansion coefficient versus temperature for the two Ni-substituted ferrites and for a third without Ni. Within the scatter of the data points, the three ferrites have the same expansion characteristics. The fourth set of data points joined with line segments is from measurements made several years ago on a nonmagnetic spinel which shows a good expansion match to the ferrite materials. The coefficient at 1000°C is $\alpha = 14.25 \text{ ppm } ^\circ\text{C}^{-1}$. For convenience we identify the latter as a "dielectric", although all of the oxides are in fact microwave dielectrics. Two other batches of dielectric were prepared, one with $\alpha = 15.2 \text{ ppm-}^\circ\text{C}$ and one having $\alpha = 13.32 \text{ ppm-}^\circ\text{C}^{-1}$. Our objective here was to prepare dielectrics with a deliberate mismatch in expansion coefficient to evaluate the effect of both tensile and compressive stresses on center-loaded toroids fired along with the matched dielectric FIP toroids and hollow (unloaded) ferrite toroids. In this way we could evaluate the degree of compositional adjustment needed to produce a composite phase shifter with optimized magnetic properties.

Large (1 kg) bars of the three dielectric compositions were isostatically pressed and fired for machining of the rectangular rod-shaped pieces. A typical fired bar is shown in Fig. 53. From a bar this size, one can machine about fifty 7 inch rods of the dielectric with the 0.105×0.133 inch cross section suitable for FIP experiments.

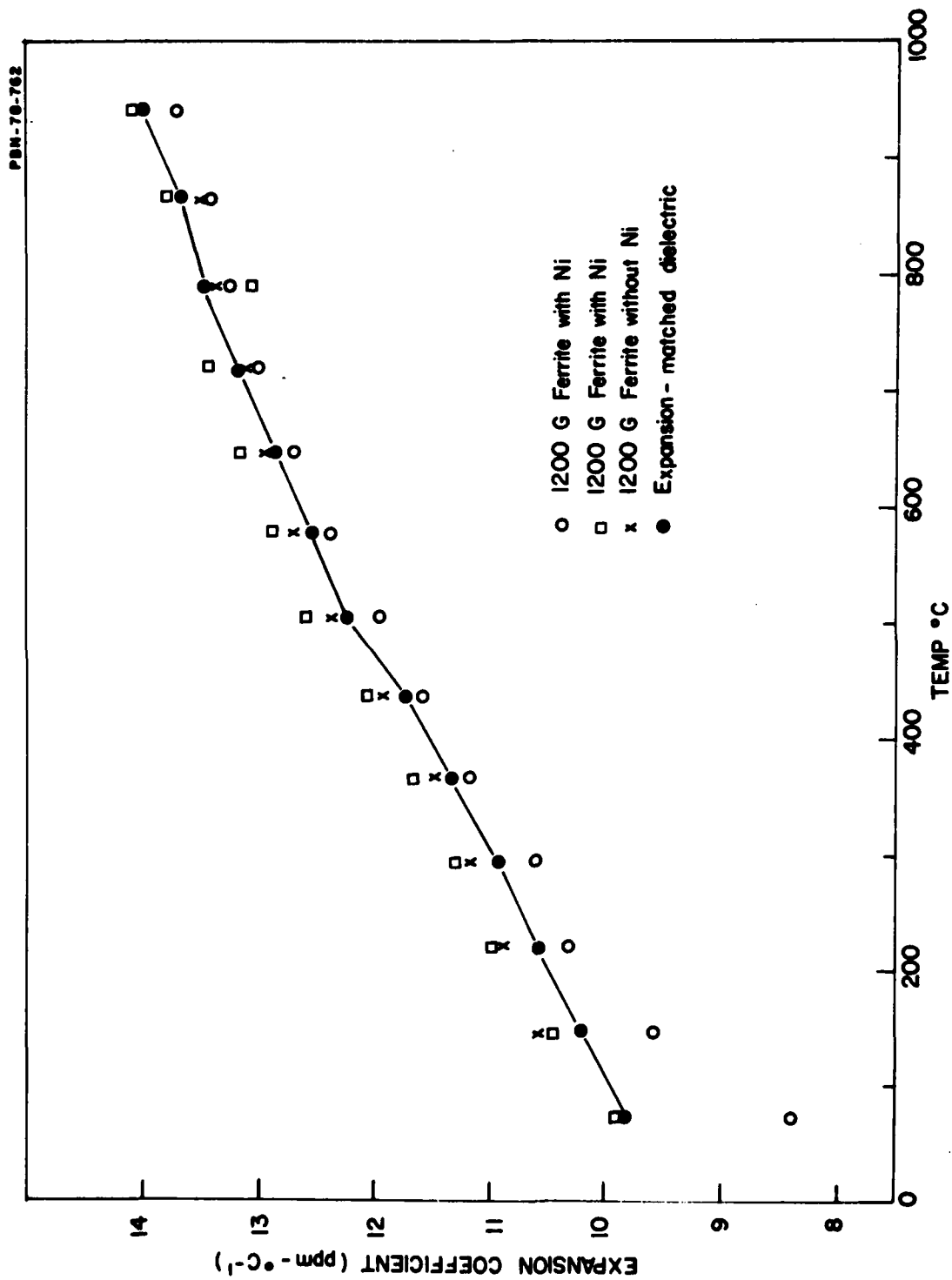


Figure 52. Thermal Expansion Coefficient vs. Temperature for 1200 Gauss Ferrites and a Matched Dielectric.

PBN-76-390

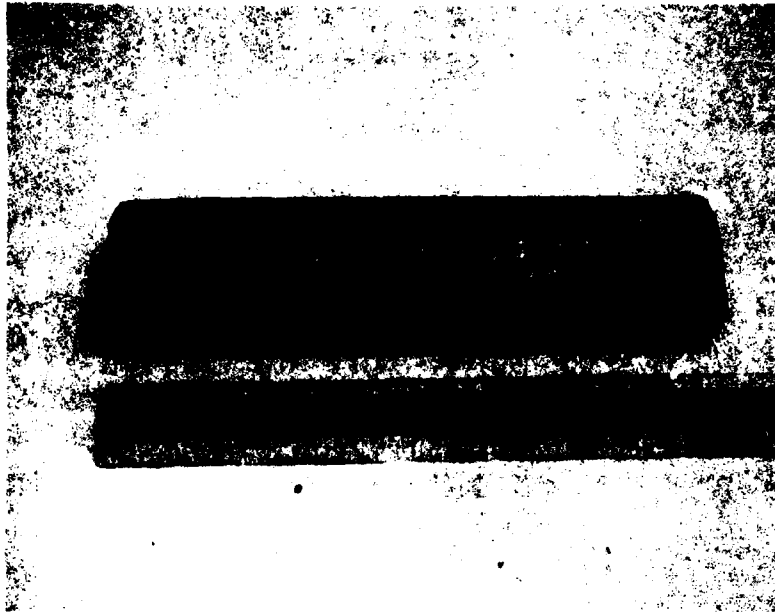


Figure 53. Bar of Li-Ti-Ferrite Dielectric Before Machining.

2.5 Verification of the Dielectric

Thermal expansion and dielectric properties at 10 GHz were measured on the three dielectric compositions chosen for FIP with the LTZNC 61-10-05-005 ferrite. Expansion coefficient was calculated from the formula

$$\alpha = \frac{l_i - l_t}{l_i(T_t - T_i)} \quad (10)$$

where l_i = initial length and l_t = length at temperature t . The coefficient α is an average slope of the $\Delta l/l_o$ curve between T_i and T_t . The data on α are summarized in Fig. 54 which gives results on three of the LMTAF170 compositions, one of LMTF195 material, and one of LMTAF160-30. Note that the value of α and therefore the slope of the curve is constantly changing, so that one must specify temperature to get a unique value. For convenience we have chosen to report α at 1000°C above T_i , nominally 1020°C, which is the normal firing temperature. In the following table we report the composition, expansion coefficient at $T_t - T_i = 1000^\circ\text{C}$, density as percent of the X-ray value, dielectric constant ϵ' , and loss tangent measured at 10 GHz. A comparison with data on the ferrite indicate a good match with the 170 material. The remaining dielectrics were prepared to explore the effect of expansion mismatch on the magnetic properties.

TABLE 6

PROPERTIES OF EXPANSION MATCHING DIELECTRICS

Designation	C o m p o s i t i o n					α 1000° (ppm/°C)	Density (% Theo.)	ϵ' tan δ at 10 GHz	
	Li	Mn	Ti	Al	Fe				
LMTF195	.9875	.10	.9759375	15.5	97.5	20.5	2.7×10^{-4}
LMTAF170	.9250	.10	.85	.20	.9250	14.2	98.5	18.5	3.1×10^{-4}
LMTAF160	.90	.10	.80	.30	.90	13.3	98.6	18.0	3.9×10^{-4}

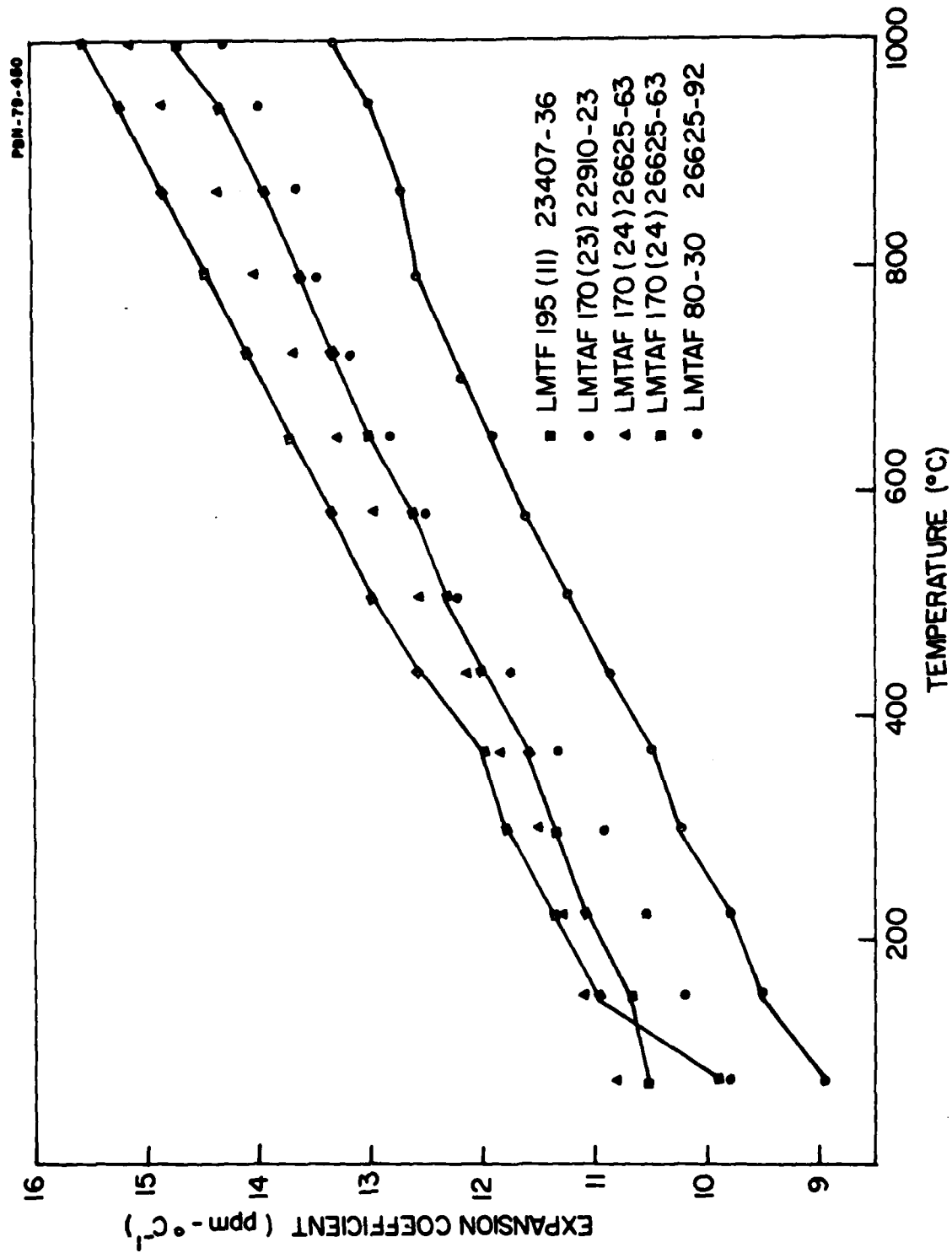


Figure 54. Thermal Expansion Coefficient vs. Temperature for Three Matched Dielectrics.

Density of 97.5 - 98.5 percent is typical of these compositions. The Bi_2O_3 content is less than the ferrite to provide some high temperature strength to the dielectric during the FIP process.

Dielectric constant and loss tangent are typical of what can be expected of these materials. One cannot increase ϵ' in these spinel solid solutions without compromising the expansion match. Note that ϵ' of the LMTAF170 composition is very nearly the same as the 1200 Gauss ferrite ($\epsilon'=18.3$).

2.6 Co-Manufacturing

In earlier sections of this report, we pointed out that there had been a change in emphasis at about midpoint in the contract, when the phase shifter design was altered from a center-loaded to a side-loaded configuration. This change in direction essentially halted co-manufacturing plans after the point of development of matched dielectric but before co-manufacture. A few preliminary firings were made with dielectric sticks about 5 percent oversize relative to the unloaded ferrite cross section. The results were promising in that we obtained well bonded, crack-free co-fired toroid-dielectrics, but disappointing in that the remanent (B_r) was about 25 percent lower than that of hollow toroids fired at the same time.

We speculate that the low B_r may have been caused by residual stresses and/or microscopic cracks generated by shrinkage onto the oversize dielectric core.

2.7 Evaluation of Li-Ti-Zn-Ferrite Toroids

2.7.1 Introduction

In the course of the contract, 264 toroids were fired. In the early phase of toroid manufacture some of the samples were unsuitable for machining because of distortion in shape or cracking. For some of the most recent samples the property data are still too fragmentary for any useful tabulation. Between

these extremes are 166 toroids for which we have sufficient data for tabulation. These have been listed in Table 4. The toroid number generally follows a chronological order of firing. The first column identifies the various batches and gives an indication of composition, as can be deduced from reference to Table 1 in Sec. 2.1. The next five columns describe the firing conditions of temperature, time, the kiln used, the steel pin used to form the part, the number of setter plates if more than one was involved, and the location of the toroid in question within the kiln. In the small kilns Nos. II, III, and V, one or two setters could be used, whereas in the large Lindberg VI kiln two or three setters were always stacked one above the other. In col. 7, a designation 1/3, for example, means that the toroid came from the bottom setter in a three tier arrangement of plates, a designation 2/2 indicates the upper of a two tier stack, and so on. This information is necessary because a tendency to bow during firing is correlated with location in the kiln, particularly vertical position, and with the presence or absence of a thermal mass, i.e., a setter plate above the toroid in question.

The next two columns in Table 4 deal with the pin clearance test applied to the individual toroids. The 0.125×0.097 inch clearance pin is the same percentage undersize (~ 6 percent) relative to the fired hole as the pin used for the same test on garnet toroids. The 0.127×0.099 inch pin (No. 1) is larger and therefore a more stringent test of hole straightness.

The next three columns are derived from ultrasonic measurements which were applied to all samples except Nos. 1 to 17 and 30 to 50. These were not available for measurement primarily because they were mounted in waveguide for early evaluation of phase shifter properties.

Coercive force (H_c) and remanent magnetization (B_r) were measured on all samples. These two properties are related to the important phase shifter requirements of drive current and saturation phase shift. They are also very sensitive to variations in average grain size (primarily H_c) and density (primarily B_r). Since the hysteresis properties are sensitive to both microstructure and magnetic performance, they were measured on all samples and have been used as the primary indicator of reproducibility. Early entries in

the table involve difference 1200 gauss compositions and variations in stoichiometry in the various test batches of the LTZNC 61-10-05-005 composition.

2.7.2 Discussion of tabulated results

2.7.2.1 Furnace conditions

The first fifteen samples were fired on v-groove setter plates which were smaller and with grooves that were not as flat as the plates that became available thereafter. The cap pieces were also nonstandard. The overall effect of these factors is expected to be less uniform firing conditions, although there is no quantitative proof of this.

Samples up through number 39 were fired under conditions in which the thermal gradient from front to rear was 25°C, about double the gradient conditions encountered in the small kiln (II, III, and V in the table) after this date. The improved gradient was due to rearrangements of insulation within the kiln. The large Lindberg kiln (No. 6) was used for most of the toroid firings. In this furnace the toroids were positioned perpendicular to the front to rear gradient which was 12°C over the width of the setter but much less than this across the individual toroids. The gradient from end to end of the toroids, i.e., from the left side of the kiln to the right, was > 5°C. Finally, from the bottom setter plate to the top plate there was a 10°C difference. Although these thermal gradients are quite small at the soak temperature, they may be larger during heating and cooling. The differences in toroid straightness with location inside the kiln indicate that gradient conditions of this magnitude do influence this property and should be carefully controlled in production.

2.7.2.2 Pin clearance and ultrasonic data

A correlation was expected and has generally been confirmed between wall thickness uniformity and the pin clearance test applied to individual toroids. Ultrasonic data were actually obtained on all four toroid walls, but the average thickness and standard deviation of the thin or flux-limiting wall (generally

sidewall B or D) is all that was tabulated. We have retained in our records for future retrieval all of the wall thickness data, measured every half-inch on each wall, for any toroid that has thickness data in Table 4.

The pin clearance tests also cover almost all of the 166 entries in the table. Toroids through which clearance pin No. 1 (the larger pin) dropped are obviously the straightest and should show the smallest standard deviation in ultrasonically measured wall thickness on the machined toroid. If we compare toroid entries No. 51 and 52, we see that the former is a No. 1 drop with a B wall standard deviation side = 0.0006 inch, whereas the latter is a No. 2 pin drop (less straight) and the B wall deviation is larger, i.e. standard deviation = 0.0020 inch. One could argue that the pin clearance could be limited by a bow in the top-bottom wall (A-C) dimension and that the data on toroid sidewall variations indicated by wall thickness measurements in the B-D dimension may not be relevant, i.e., that the two tests were limited by different dimensions and therefore would not necessarily correlate. In most cases, however, the greater deviations are in sidewall straightness. The results of ultrasonic sidewall measurements are reported in the table. Thus a correlation between pin clearance and measured wall thickness can be made from the single wall data in the table. Generally, 1 drop toroids have a wall variation of s.d. ≤ 0.0017 or less and in a "one push" category the wall variation has a s.d. ≤ 0.0043 . For pin No. 2 s.d. ≤ 0.0025 in wall thickness variation is equivalent to "two drop," whereas "two push" yields a toroid with s.d. ≤ 0.0056 . Since the clearance pins themselves have a slight amount of flex, a sample that has a simple bend from one end to the other will more easily pass a "push" test than a sample with less bend but with a compound or "S" bend.

2.7.2.3 Summary of toroid firings

After studying the various combinations of ferrite batch number isostatic bag-pin combination, toroid location in the kiln, oxygen flow, and firing schedule, we have evolved a few generalizations which can serve to guide future work.

1) In no case was the fired toroid as straight as the pin around which the green toroid was formed. This means that firing conditions degrade the straightness of the fired toroid.

2) The straightness of the forming pins is also an important factor. Some of the pins, notably Nos. 14 and 15, although within our ± 0.001 inch specification, consistently broke the toroids on dismounting and were not used. Others such as Nos. 10, 11, 13, and 16 seemed to produce consistently straighter toroids when compared with Nos. 9 and 17.

3) Iron stoichiometry clearly affects final grain size, as shown primarily by H_c data. Compositions 61N(6) and 61N(7) are notable in that H_c is consistently 0.6 to 0.8 Oe, as contrasted with other ferrite batches, where $H_c \approx 1.0$. An increased Fe content also raises $4\pi M_s$ and B_r , as one might expect from considerations regarding cation site occupancy.

The (G-10) and (G-11) production batches were very close in composition and proved quite similar in their magnetic properties. Although lower in B_r than the smaller Research-made batches, G-10 and G-11 fired toroids were also lower in $4\pi M_s$ by the same percentage. The Fe excess 61N(6) toroids have high B_r but also the highest $4\pi M_s$. All this would suggest that the fired density of the various batches is about the same and that we are seeing differences in B_r and $4\pi M_s$ that are primarily caused by the deliberate compositional (Fe) variations in the test batches.

2.7.3 Future work

Clearly, the primary objective in any follow-on work with these materials will be to improve the straightness of the fired toroids. One aspect of this would be to secure straighter forming pins, either ceramic or metal. Another would be study the correlation between position in the furnace and fired straightness. Furnace VI results indicate that toroids fired on the bottom setter of the toroid show a general tendency to bow in one direction, whereas toroids from the upper setter tend to bow in the opposite direction. The

relationship between straightness and location is complex and there are other factors to be investigated; however, this area deserves careful study. Experiments, for example, concerned with toroid straightness as a function of the thermal mass and the separation distance between setter plates may help to resolve these contributing factors and their relative importance.

2.8 Phase Shifter Evaluation

During the course of the 200 toroid fabrication, several toroids from the large powder batches G10 and G11 were selected for temperature measurement similar to those in Sec. 2.0. In addition, a 1350 gauss garnet toroid was put through identical testing. The results are given in Figs. 55-58. The temperature coefficients for the long and short states are given in Table 7. In making this comparison between phase shifters, we have once again normalized the toroid wall thickness to give 360° phase shift at 80°C . The actual measured temperature coefficients have been either increased or decreased by amounts equal to the wall thickness adjustment.

While the LiFe gives a near-zero coefficient for the long state, the short state being the temperature sensitive state, the garnet shows the long and short states to have temperature coefficients of approximately the same magnitude but of opposite signs. Over the temperature range of interest ($17\text{--}20^\circ\text{C}$), the garnet and LiFe are quite similar in the amount of saturation phase they give (Figs. 56 and 58).

2.9 Economic Forecast: Relative Cost of Toroids Made From Lithium Ferrite and Garnet

The relative cost of toroids reduces to comparing raw material costs. The reasons for this are described in this section.

The comparison of the costs of toroids manufactured using lithium titanium ferrite and yttrium gadolinium garnet is based on the following assumptions:

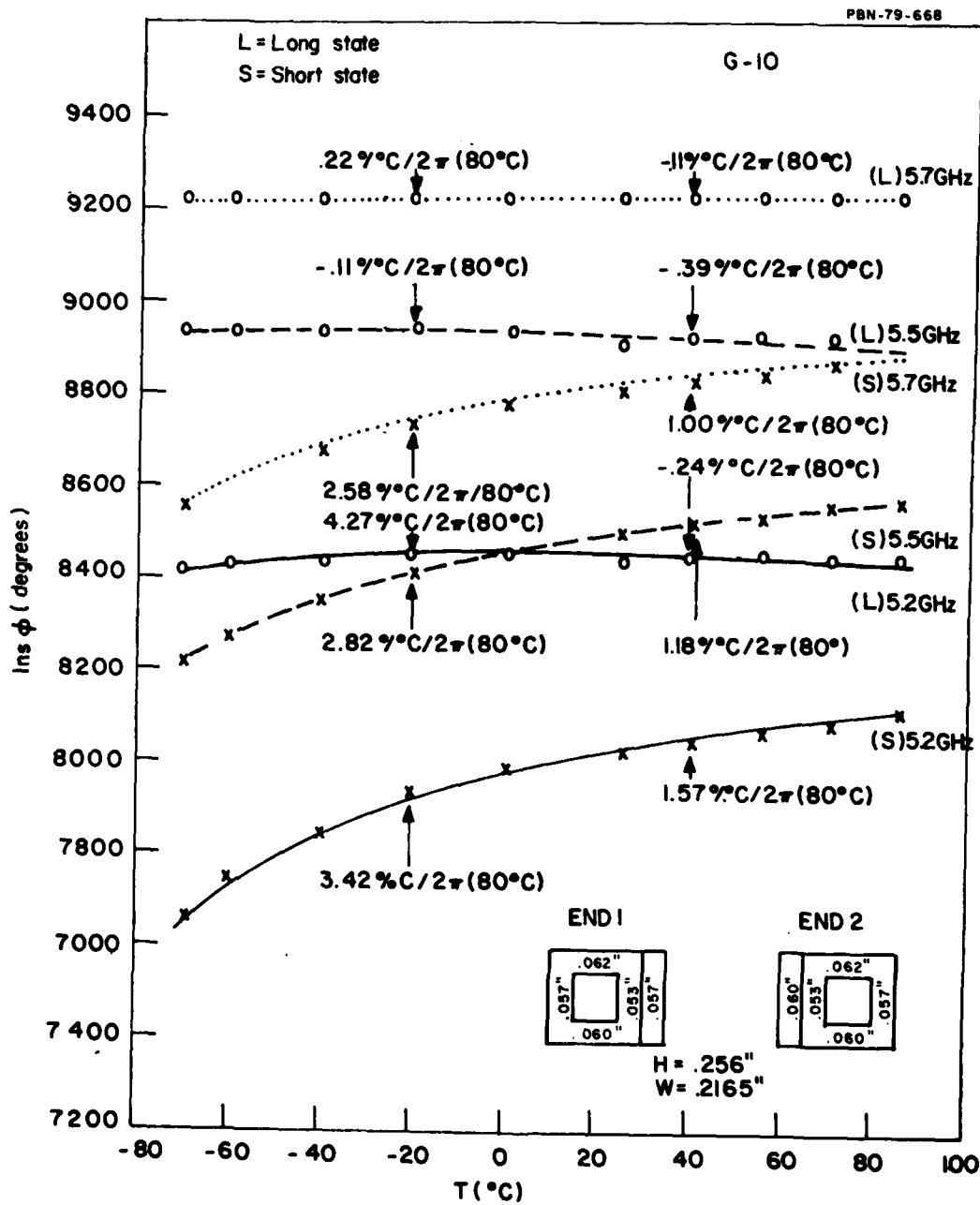


Figure 55. Saturated Insertion Phase as a Function of Temperature.

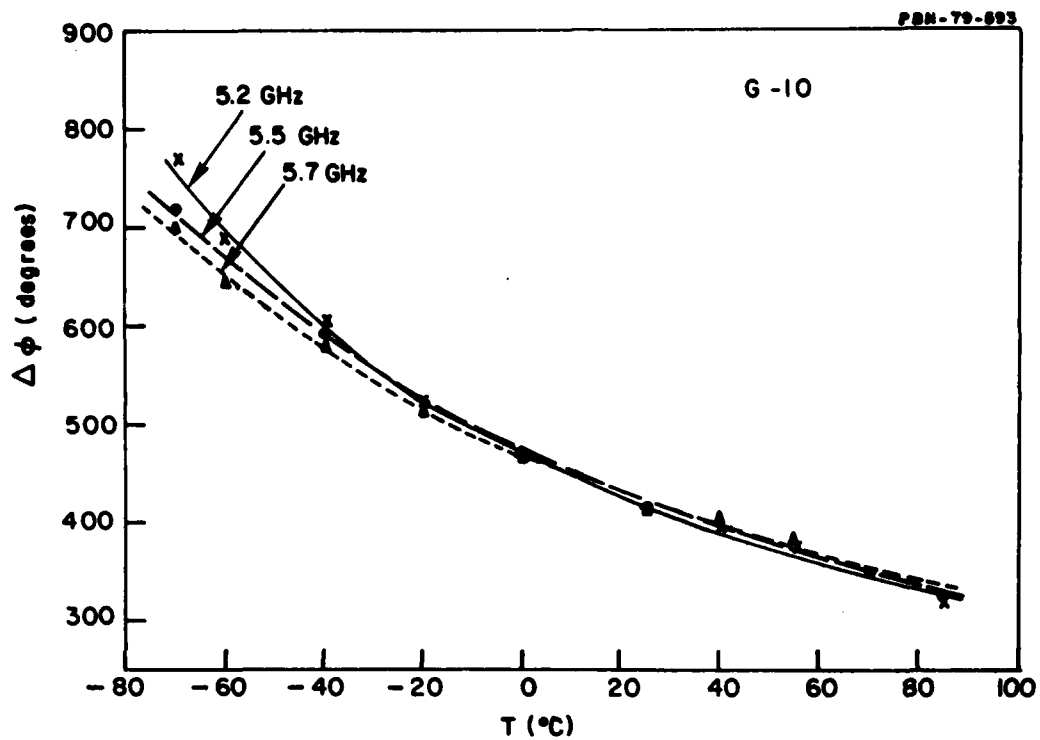


Figure 56. Saturated Differential Phase as a Function of Temperature.

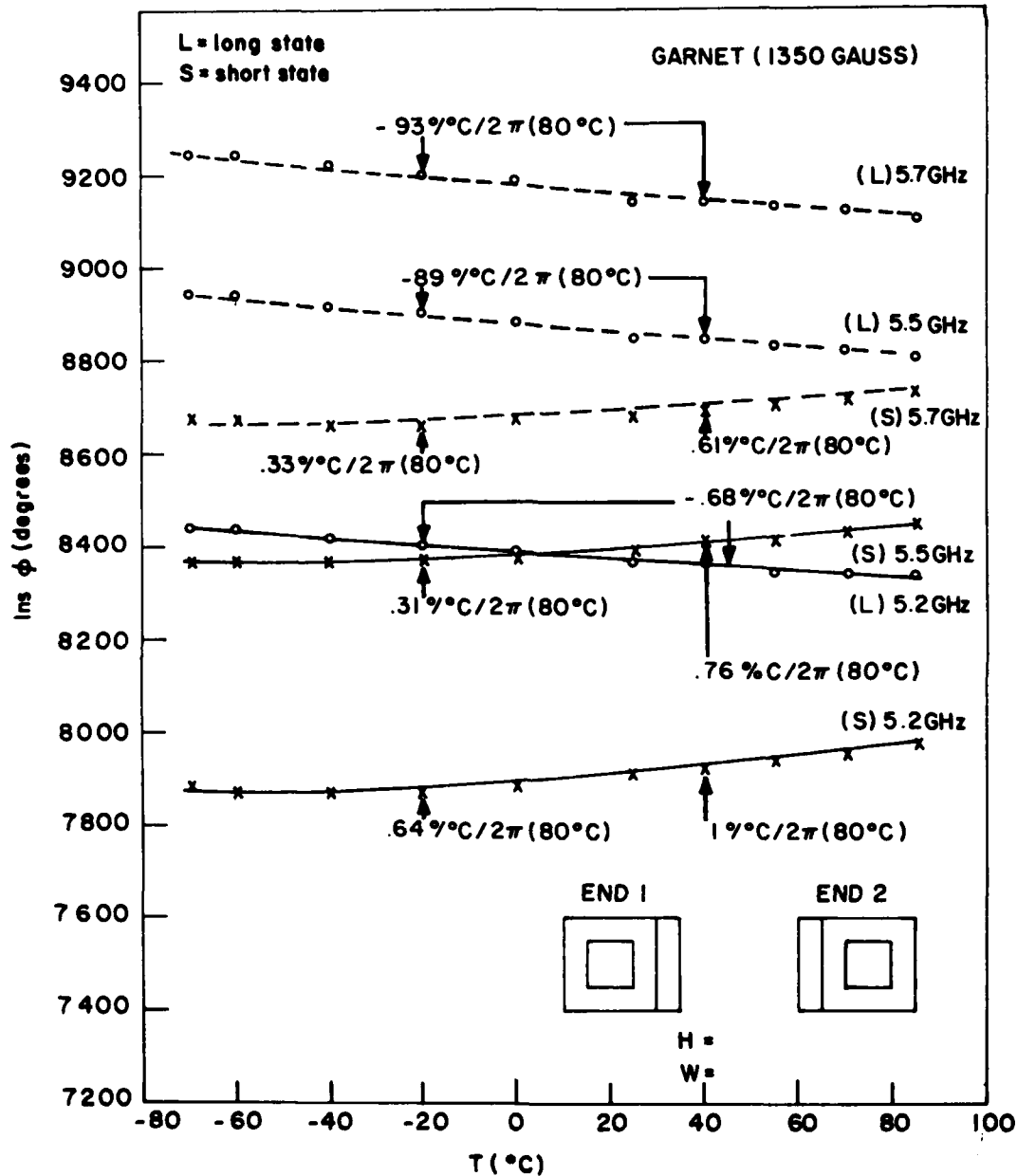


Figure 57. Saturated Insertion Phase as a Function of Temperature.

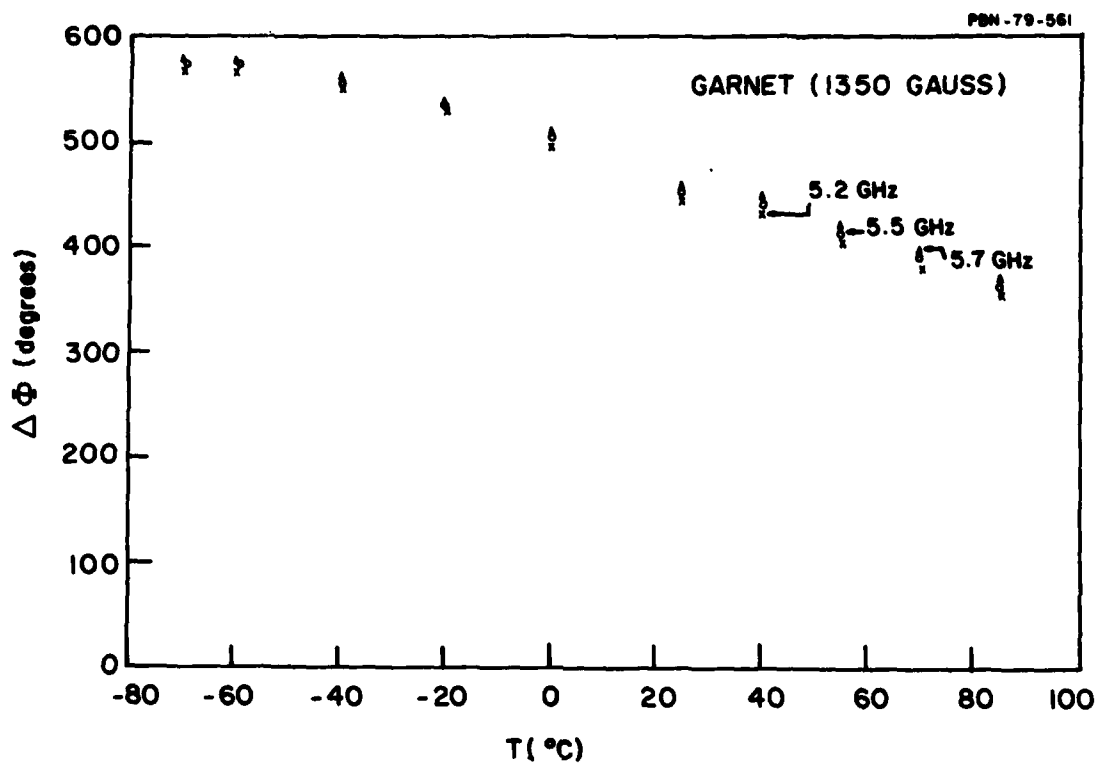


Figure 58. Saturated Differential Phase as a Function of Temperature.

TABLE 7
INSERTION PHASE TEMPERATURE COEFFICIENT
 (degree/degree centigrade/360° $\Delta\phi$ at 80°C)

<u>Mat.</u>	<u>State</u>	<u>T</u>	<u>5.2 GHz</u>	<u>5.5 GHz</u>	<u>5.7 GHz</u>
G10	Long	-20°C	+ .27	- .11	+ .22
		40°C	- .24	- .39	- .11
	Short	-20°C	+ 3.42	+ 2.82	+ 2.58
		40°C	+ 1.57	+ 1.18	+ 1.00
Garnet	Long	-20°C	- .68	- .89	- .93
		40°C	- .68	- .89	- .93
	Short	-20°C	+ .64	+ .31	+ .33
		40°C	+ 1.00	+ .76	+ .61

(a) Both toroids will be of similar size.

(b) Each will be produced at a rate of 100,000 toroids per year.

Hence the volume of material processed in a year will be the same for each composition, and the type and size of the plant and equipment will also be similar.

Given these assumptions, the manufacturing cost can be considered as being composed of three elements, namely raw materials cost, touch labor, and support services. The basic steps in the manufacturing process are listed as follows:

- (1) Weight and mix raw materials.
- (2) Calcine (i.e., chemical reaction to produce ferrite).
- (3) Final grind and mix.
- (4) Batch evaluation.
- (5) Powder preparation.
- (6) Press toroids.
- (7) Sinter.
- (8) Final test.

In the last three steps, the material is handled on an individual toroid basis, whereas in the first five steps the cost per toroid is reduced as the size of the batch is increased. In both cases, it is unlikely that any major difference in the cost of labor to produce toroids, whether there will be garnet or lithium ferrite. Hence, the fundamental basis for an economic projection is the relative cost of the raw materials.

The major constituents of the raw materials used to manufacture toroids are listed as follows:

GARNET		LITHIUM FERRITE	
Material	Weight (%)	Material	Weight (%)
Iron Oxide	49	Iron Oxide	51
Gadolinium Oxide	18	Titanium Dioxide	24
Yttrium Oxide	32	Lithium Carbonate	13
Other Materials	1	Manganese Carbonate	6
		Other Materials	6

Iron oxide comprises 50 percent of the raw material content in each case, but it represents only a small part of the raw material cost. The basis of the cost difference, then, is the relative cost of the rare earth oxides to the titanium, lithium salts, etc.

Rare earth oxides cost between \$30 and \$50 per pound, 10 to 20 times more than the non-iron constituents of lithium ferrite. As a result, a factor of 10 difference in the raw material costs is conservative.

Using 100,000 toroids per year as the basis, the difference in cost of the raw materials is \$205,000. This figure is realistic and is based on the needs of an efficient plant and manufacturing process. This number breaks down to \$2.05 per individual toroid.

3.0 SUMMARY AND CONCLUSIONS

The early stages of this program involved the development of a new lithium ferrite composition which gave a better temperature dependence of the insertion phase than a straight lithium titanium ferrite. Of the compositions tested, a LTZNC-61-10-05-005 composition was selected because it gave the lowest temperature coefficient for the insertion phase of the short state ($1.2^{\circ}/^{\circ}\text{C}$ average at 40°C).

Subsequently, eight 2-Kg powder batches and two 30-Kg batches were fabricated and used to determine the proper forming and firing conditions. These powders varied in iron stoichiometry from an iron-excess powder which produced a high saturation magnetization (1260 g) and a low coercive force (~ 5 Oe) to iron-deficient powders which produced a saturation magnetization of 1130 gauss and a somewhat higher coercive force (~ 1 Oe). The two 30-Kg powder batches were of the iron-deficient type, which is preferable since a low saturation magnetization along with a low anisotropy field leads to the lowest temperature coefficient of insertion phase.

In the course of determining the proper firing conditions, particular attention was paid to toroid location within the kiln and the effect of the surrounding furniture in the kiln. The straightest toroids were produced when the samples were placed on setters and covered with alumina caps (similar to the setter material) and then located in positions (usually in the center of the kiln) where temperature gradients were minimal.

To evaluate these toroids it was necessary to develop a pin drop test which gave some estimate of the straightness of the center hole. An improvement in the analysis of the phase shifting wall was made using an ultrasonic thickness measuring instrument (from Panametrics). This instrument permitted the repeatable measurement of wall thickness to tenths of a mil. Since the external walls were machined, flat variations in wall thickness could be ascribed to a wandering of the center hole. Part of this hole irregularity was traced to curvature of the pin used for the isostatic pressing and part resulted from

distortion during firing. Further work in this area is warranted.

Over two hundred toroids were produced from these ten powder batches in a variety of firings. Loop properties and dimensions were measured on all toroids and are catalogued in this report.

The work performed during the first year of this program has set the stage for the second year program. It has produced optimized composition; established firing, forming, and evaluation techniques; and focussed attention on the problem of maintaining center-hole straightness. During the second year of this program the lessons of the first year will be applied to producing 200 toroids with close material and dimensional tolerances.

DISTRIBUTION LIST

<u>ADDRESS</u>	<u>NO COPIES/ORIGINALS</u>
1. Commander U.S. Army Missile Research & Development Command ATTN: DRDMI-EAM Redstone Arsenal, Alabama 35809	60/1
2. Defense Documentation Center Cameron Station Alexandria, Virginia 22314	2/0
3. Commander U.S. Army Industrial Base, Eng. Activity ATTN: DRXIB-MT Rock Island, Illinois 61201	1/0
4. Director U.S. Army Mechanics and Materials Research Center ATTN: DRXMR-MT Watertown Arsenal Watertown, Massachusetts 02172	1/0
5. Commander U.S. Army Material Development and Readiness Command ATTN: DRCMT Alexandria, Virginia 22333	1/0
6. Commander U.S. Army Missile Research & Development Command ATTN: DRDMI-TI Redstone Arsenal, Alabama 35809	1/0